# Detection and Classification of Buried UXO and Determination of Seafloor Parameters in Littoral Environments using Resonance Scattering Sonar

Roland Gritto[1], Valeri Korneev[2], Lane Johnson[2]

[1]Array Information Technology
[2]Lawrence Berkeley National Laboratory


Principal Investigator:

Roland Gritto
510.428.0400
Roland.Gritto@arrayinfotech.com

| | | | Form Approved OMB No. 0704-0188 |
|---|---|---|---|

## Report Documentation Page

*Form Approved*
*OMB No. 0704-0188*

Public reporting burden for the collection of information is estimated to average 1 hour per response, including the time for reviewing instructions, searching existing data sources, gathering and maintaining the data needed, and completing and reviewing the collection of information. Send comments regarding this burden estimate or any other aspect of this collection of information, including suggestions for reducing this burden, to Washington Headquarters Services, Directorate for Information Operations and Reports, 1215 Jefferson Davis Highway, Suite 1204, Arlington VA 22202-4302. Respondents should be aware that notwithstanding any other provision of law, no person shall be subject to a penalty for failing to comply with a collection of information if it does not display a currently valid OMB control number.

| 1. REPORT DATE **02 APR 2010** | 2. REPORT TYPE | 3. DATES COVERED **00-00-2010 to 00-00-2010** |
|---|---|---|

| 4. TITLE AND SUBTITLE **Detection and Classification of Buried UXO and Determination of Seafloor Parameters in Littoral Environments using Resonance Scattering Sonar** | 5a. CONTRACT NUMBER |
|---|---|
| | 5b. GRANT NUMBER |
| | 5c. PROGRAM ELEMENT NUMBER |
| 6. AUTHOR(S) | 5d. PROJECT NUMBER |
| | 5e. TASK NUMBER |
| | 5f. WORK UNIT NUMBER |
| 7. PERFORMING ORGANIZATION NAME(S) AND ADDRESS(ES) **Array Information Technology,7474 Greenway Center Drive, Suite 600,Greenbelt,MD,20770-3504** | 8. PERFORMING ORGANIZATION REPORT NUMBER |
| 9. SPONSORING/MONITORING AGENCY NAME(S) AND ADDRESS(ES) | 10. SPONSOR/MONITOR'S ACRONYM(S) |
| | 11. SPONSOR/MONITOR'S REPORT NUMBER(S) |

| 12. DISTRIBUTION/AVAILABILITY STATEMENT **Approved for public release; distribution unlimited** |
|---|

| 13. SUPPLEMENTARY NOTES |
|---|

| 14. ABSTRACT |
|---|

| 15. SUBJECT TERMS |
|---|

| 16. SECURITY CLASSIFICATION OF: | | | 17. LIMITATION OF ABSTRACT | 18. NUMBER OF PAGES | 19a. NAME OF RESPONSIBLE PERSON |
|---|---|---|---|---|---|
| a. REPORT **unclassified** | b. ABSTRACT **unclassified** | c. THIS PAGE **unclassified** | **Same as Report (SAR)** | **83** | |

**Standard Form 298 (Rev. 8-98)**
Prescribed by ANSI Std Z39-18

# Table of Contents

# List of Figures

3

## List of Tables

## List of Acronyms

AIT:                  Array Information Technology
APL-UW:         Applied Physics Laboratory, University of Washington
LBNL:             Lawrence Berkeley National Laboratory
NSWC-PC:       Naval Surface Warfare Center, Panama City
UXO:               Unexploded Ordnance

# 1 Summary

The goal of this limited-scope project was to investigate whether narrow-band resonance-scattered waves can be observed in a small dataset collected by a sonar platform in a controlled pond environment and whether these waves can be used to locate UXO in the pond sediments. Furthermore, it was investigated whether UXO can be characterized by their size and filler velocities and whether medium velocities can be derived from the field data.

Analysis of the field data was supported by numerical modeling. It was found that resonance scattered waves were present in all numerical data and in the cases of a proud sphere and a buried cylinder. In all other cases of proud UXO the field data revealed frequency dependent scattered waves that were part of the direct reflected waves. Imaging UXO with monochromatic data produces surprisingly good results considering that in most investigated cases a small fraction of the data with very low amplitudes were used in comparison to data typically used for Kirchhoff migration or SAS imaging. The images derived from resonance scattered waves were generated by data obtained from narrow passbands throughout the whole frequency spectrum such that different parts of the UXO can be illumination separately. This has the advantage of imaging, for example, a cone shaped tip of an UXO separately from its broader tail, which helps to interpret the resulting images. The fact that the resonance images were obtained from much smaller signal amplitudes suggests that monochromatic source signals with longer time duration (i.e., comparable to typically used broadband pulse times) would greatly increase the signal-to-noise ratio. Consequently it would be possible to image smaller objects in sediments that would not be visible when illuminated by a broadband signal. Range resolution is reduced when imaging is done with monochromatic signals. However, the image resolution can be dramatically improved by adding data from different azimuth as was demonstrated for the cases of a proud sphere and bomb. It is noted however, that the images obtained with resonance migration are intended for detection and localization only, while characterization of the object is based on spectral properties.

The resonance waves were manifested by a range of spectral peaks in the amplitude spectrum. The complex spectral pattern depends on the shape, the dimensions, and the internal properties of the UXO and the properties of the embedding medium. Therefore, the spectrum can be used as a spectral fingerprint to characterize the object after it has been detected and localized in space. To achieve this goal, a database with typical UXO-shaped objects located in sediments needs to be compiled, to include the effect of intrinsic attenuation that cannot be modeled very easily with the current knowledge and computational resources. Results from spectral analysis of numerical data from a single UXO under different orientations suggest that the spectral peaks associated with the different spectra were stable and could be matched at low and high frequencies. The outcome suggest that the resonance peaks can be used to characterize the objects when match to a spectrum from a pre-computed database. In contrast, two cylinders with small differences in size produced resonance peaks that were not comparable, such that the two objects could be distinct by their spectral character. In a previous study, the minimum difference in typical filler velocities was determined to be 150 m/s. A

numerical experiment was conducted to determine whether the smallest difference in typical filler velocities of 150 m/s is detectable in the frequency spectrum. The results for identical cylinders with a difference in P- and S-wave velocity of 150 m/s and 87 m/s, respectively, produced relative shifts of 2.5 % in the resonance peaks, suggesting that the peaks could be used to distinguish UXO filler.

Velocity estimates of the background medium have been performed based on the fidelity of the resonance images. A range of velocities including the correct value will produce a suite of images that are progressively defocused the more the migration velocity differed from the correct value. Therefore, the sharpest migration image will yield the correct medium velocity. This approach is independent of the number of objects imaged, because the principle of focusing and defocusing is universal.

## 2    Introduction

Current sonar technology applied to littoral munitions management is concerned with the detection and characterization of UXO in the water column and located proud on the seafloor. Most sonar applications work in the high-frequency regime where specular scattering off the UXO surfaces dominates the reflected signal (Figure 1a). These applications are aimed at locating and characterizing the object by generating a visual image of the UXO and its shadow on the seafloor. Current efforts are underway to extend these sonar applications to buried objects investigating the effectiveness of seafloor penetration by sonar waves (Lim et al., 2009, Kargl et al., 2009). However, high frequencies are generally not well suited to penetrate the seafloor and image buried objects. Biologic activity in the upper parts of the sediments may cause anaerobic conditions producing gas pockets that attenuate the acoustic signal and constrain the maximum penetration of the waves. If free gas is present in the sediments, it may produce anelastic attenuation particularly for the high frequency components of the sonar signal.

In contrast, resonance scattering (also referred to as structural acoustics) sonar applications are currently developed to help detect and characterize proud and partially buried objects (Bucaro et al., 2007a, 2007b; Houston et al., 2002, Houston et al., 2009). The frequency range is lower than in the aforementioned application with wavelengths on the same order or somewhat longer than the dimensions of the object (Figure 1b). The advantage of this frequency range is the emission of resonance scattered energy by the object which carries more information about the internal structure of the UXO than in the case of specular reflections (Brill et al., 1982; Gaunaurd, 1992). In contrast to specular reflected waves which bounce off the outer shell of UXO and consequently depend on its orientation, resonance scattered waves are generated by vibrations of the whole UXO body in form of circumferential waves that propagate continuously around the UXO radiating energy into the surrounding medium (Runkle et al., 1999a; 1999b). As a consequence the frequencies of resonance waves are less dependent on UXO orientation, which simplifies the characterization of the target. Furthermore, the radiation of resonance waves by UXO continues long after the reflected waves have decayed.

The goal of this limited-scope project is to investigate whether resonance-scattered waves can be observed in a small dataset collected by a sonar platform in the controlled pond environment of the Naval Surface Warfare Center, Panama City (NSWC-PC), FL, and whether these waves can be used to locate UXO in the pond sediments. Furthermore, it was investigated whether the UXO can be characterized by their size and filler velocities and whether medium velocities can be derived from the field data.

# 3      Numerical Modeling

## 3.1      Model Parameters

In the following, numerical modeling will be employed to demonstrate the nature of resonance scattering and how resonance waves can dominate the scattered wavefield of proud and buried UXO-like objects.

The numerical modeling is conducted using a 3-dimensional finite difference code with accuracy of $2^{nd}$ order in time and $4^{th}$ order in space based on the staggered grid method. The model consists of a 3 m x 3 m x 3m cube, where the upper half and lower half are representing water and sand, respectively. Node spacing in x-, y-, and z-direction is uniform at 0.005 m resulting in $600^3$ or 216 million nodes. Computing was performed based on parallel architecture with 8 CPUs. Attenuation along the boundaries is obtained by absorbing boundary conditions including exponential functions to suppress reflections of the wavefield from the edges of the model. However, the exponential functions were limited to 20 nodes on either side of the model to maximize the modeling volume. This resulted in some modest reflections off the model boundaries, while it did not interfere with the modeling results. A schematic view of the model is presented in Figure 2. The physical parameters of the model were taken from pond measurements performed during data acquisition by the Applied Physics Laboratory, University of Washington, at the NSWC-PC pond facility. The physical model parameters are listed in Table 1.

|                  | Water | Sand  |
|------------------|-------|-------|
| Vp [m/s]         | 1,482 | 1,719 |
| Vs [m/s]*        | 0     | 0     |
| Density [g/ccm]  | 1.0   | 2.0   |

**Table 1:** Physical properties of water and sand at the pond facility of NSWC-PC during data acquisition in 2007 (Kargl, personal communication, 2009). * The shear wave velocity in the pond sediments is sufficiently low that it is assumed to be zero for the modeling study.

## 3.2      Numerical Modeling of Proud Shell and Mortar

In order to model attributes of resonance scattering for the case of two proud UXO, a 4-inch artillery shell and an 81-mm mortar were used to demonstrate the kinetic and spectral properties of resonance scattering. The dimensions and elastic properties of the UXO are presented in Table2.

| Object | Shell | Mortar |
|---|---|---|
| Length [m] | 0.417 m | 0.520 m |
| Diameter [m] | 0.102 m | 0.081 m |
| **Casing** | **Steel** | **Steel** |
| Vp [m/s] | 5,950 | 5,950 |
| Vs [m/s] | 3,240 | 3,240 |
| $\rho$[g/ccm] | 7. 85 | 7. 85 |
| **Filling** | **Iron** | **Concrete** |
| Vp [m/s] | 5,920 | 3,560 |
| Vs [m/s] | 3,230 | 2,160 |
| $\rho$[g/ccm] | 7.87 | 2.4 |

**Table 2:** Physical properties of two UXO used for numerical finite difference modeling.

The numerical model and source receiver geometry were chosen as presented in Figures 3 and 4. The model was based on a single source position located 1 m above the UXO and two crossing receiver profiles. The 2 m long profile along the x-axis was comprised of 401 receivers spaced at 0.005 m, while the 3.4 m long profile along the y-axis was comprised of 681 receivers at the same spacing. Because of limitations in resolution of the finite difference technique the shape of the artillery shell and mortar were modeled by spherical cylinders. Using the physical parameters from Table 2, the 4-inch shell was modeled by a 0.415 m long cylinder with a diameter of 0.1 m. The interior velocities for P- and S-waves and density were chosen to match those of the iron filled artillery shell. However, for reason of limitation in resolution, the thin steel casing of the shell was not modeled. Similarly, the 81-mm mortar was modeled by a 0.52 m long spherical cylinder with 0.08 m diameter and P- and S-wave velocities and density matching those of the concrete filled mortar. Even though this geometry is a simplification of the actual field case, it provides sufficient resolution and accuracy to demonstrate the physical properties of resonance scattering for these two UXO classes.

### 3.2.1 Wavefield Snapshots

Finite difference modeling offers the opportunity to study the amplitude distribution of the wavefield throughout the model at every time step. To demonstrate the kinematics of resonance scattering, time snapshots for the model with the proud shell are presented in Figures 5-7. In the following all wavefield snapshots and time section display the divergence of the numerically calculated wavefields. The wavefield shown in Figure 5 represents early times (t = 1 ms) shortly after the incident wave has reached the

seafloor. The dominant waves include the incident P-wave, reflections off the water surface and seafloor interface as well as scattered waves by the shell into the water column and into the seafloor. At intermediate times (Figure 6), the wavefield has already changed dramatically and is comprised of reflected waves, insufficiently attenuated along the model boundaries, and visible by the crossing pattern throughout the figure. The resonance waves, although slightly smaller in amplitude than the reflected waves, are already present throughout the model and can be easily recognized by their concentric shape centered on the shell. The difference in P-wave velocity between the water and seafloor is manifested by the longer wavelength of the waves propagating in the lower half of the model. Figure 7 displays the wavefield after a time of t = 5 ms. It can be easily seen that the wavefield is completely dominated by resonance waves radiating from the shell on the seafloor. It is noted that the resonance waves propagating within the shell are mainly composed of S-waves propagating with the shear wave velocity of steel. In contrast, the resonance waves in the outer medium (i.e. sand and water in the current case) are propagating as P-waves with the compressional wave velocity of sand and water, as the shear wave velocity is set to zero (refer to Table 1). This is a non-trival finding that demonstrates that resonance waves can propagate as compressional waves in the background medium, because in the case of a solid medium with finite shear strength, resonance wave propagate as shear waves in the background medium (Korneev, 2009). Therefore, the observation of resonance waves in the current case is an indication that these waves can be used for UXO detection and location.

### 3.2.2 Time Sections

The reverberating nature of resonance wave can easily be assessed in time sections, where the recorded trace at each receiver position is displayed as a function of time. The time section recorded by the receivers along the x-profile, oriented perpendicular to the long axis of the shell (see Figure 4), is presented in Figure 8. In this figure, the waves have been muted prior to t = 0.0009 s to suppress the direct waves, which presented the largest amplitude in the wavefield snapshots at early times as shown in the last section. The strongest amplitudes in the time section arriving at about 0.001 s represent the waves reflected directly off the shell. The observed moveout is a function of the water velocity, the receiver spacing and the location of receiver profile relative to the location of the shell. It is evident that the largest amplitudes of the reflected signal attenuate quickly, while some phases with low amplitudes and hyperbolic moveout are visible at later times throughout the time section. The later phases are resonance scattered waves, which are more pronounced in Figure 9, where the first 0.005 s of the time section have been muted. It can now be seen that these waves are recorded at each receiver position and continue to resonate for the duration of the recording time.

The spectral content of the resonance waves is presented in Figure 10a, which shows the normalized amplitude spectrum from 0-50 kHz. Numerous maxima related to the resonances of the proud shell are visible throughout the spectral range. The number of spectral peaks indicates the complex interaction between the elastic waves and the shell. The different spectral peaks are related to phases that interact with the shell to form a

large number of waves propagating in various directions internally and along the outside of the shell. These waves include, face crossing and meridional Rayleigh and Stoneley waves, helical or circumferential waves, bending waves and internal multiple scattered body waves. The complex spectral patter depends on the shape of the object, its dimensions, its internal properties and the properties of the embedding medium. Therefore, the spectrum can be used as a spectral fingerprint to characterize the object after it has been detected and localized in space.

Localization of the object can be done based on resonance waves associated with narrow spectral bands as will be shown in Chapter 4 for the case of the pond data. In the current example, the resonance waves associated with the spectral peak at 5,750 Hz will be investigated. It is noted that the energy at 5,750 Hz is less than 0.2 % of the total energy in the spectrum (see arrow in Figure 10a). However, after applying a narrow (200 Hz) bandpass filter centered at this frequency to the wavefield in Figure 9 the resulting waves are presented in Figure 10b. The monochromatic nature as well as the hyperbolic moveout of the resonance waves is apparent in the time section. It is noted that although the energy at 5,750 Hz represent only a fraction of the total spectral energy, they form coherent wavefronts in the time section. The advantage of using low frequencies is the gain in seafloor penetration as mentioned in the introduction. However, the resonance method is not limited to low frequencies and even high frequencies can penetrate the seafloor as will be discussed in Chapter 4. As mentioned above, the apex and the moveout of the hyperbola are related to the location of the object relative to the receiver profile, which can be utilized to locate the object in space. Furthermore, the narrow bandpass filtering removed all unwanted phase arrivals from the wavefield. The continuous oscillation of the resonance waves in the time domain is a result of the narrow passband which creates a near monochromatic pulse. The advantage of using these waves for location is that they are independent of source origin time, while the necessary phase information is obtained by the delay of the phase from trace to trace across the time section. As a consequence, the amplitudes can be chosen anywhere on the time sections, i.e., where the signal to noise ratio is optimal (Korneev, 2009). In order to form an image of the object and to locate it in space, more than one source record is needed. However, generating a sufficient number of source records to demonstrate a reliable location is not practical because of the time constraints associated with the 3-D finite difference model. For comparison, the pond data were acquired with 750 source locations. Nevertheless, the current example is educational in that it exhibits another attribute associated with resonance scattering. The wavefield in Figure 10b exhibits variations in amplitudes and phase shifts across the recorded traces (see arrow in Figure 10b). These variations exhibit the complexity of the scattered wave pattern, which indicates constructive and destructive interference of the scattered waves throughout the object. The variations have been found in resonance data for all numerically modeled and field objects, as will be shown below. The migration of these amplitude patterns to locate objects will form images that are different from those obtained with SAS imaging. Nevertheless, the objects are correctly located while their characterization can be done by spectral pattern recognition.

The time section recorded by the receivers along the y-profile, oriented parallel to the long axis of the shell (see Figure 4), is presented in Figure 11. In this case the

geometry of the receiver profile and distance to the shell prevented the direct waves from being completely muted ahead of the reflected waves. Therefore, remnant amplitudes of the direct waves can be seen at large offsets on either side of the profile. Nevertheless, the results are similar to the case of the x-profile. Coherent direct reflected waves are visible between 0.001 and 0.0013 s throughout the whole record section, followed by faint amplitudes. Muting the first 0.005 s generated the wavefield presented in Figure 12, where the reverberating nature of the resonance wave is apparent again. Upon close inspection it can be seen that two hyperbolas with separate apexes are crossing in the time section. This is due to the geometry of the profile running parallel to the long axis of the shell, which generates scattered waves off the front and back edges of the shell, which are recorded by separate receivers at different time. In contrast the case of the x-profile is symmetric with respect to scattering off the edges. The spectrum of the wavefield in Figure 12 is presented in Figure 13a. Similar to the data recorded along the x-profile, it is dominated by spectral peaks associated with different types of resonance waves throughout the frequency range. In the current case, the phases associated with the frequency peak at 7,000 Hz (see arrow in Figure 13a), representing less than 0.2 % of the total spectral energy, are selected for narrow (200 Hz) bandpass filtering. The processed resonance data are displayed in Figure 13b, where the reverberating nature and the hyperbolic moveout are visible. As previously seen, variations in amplitude and phase shifts are apparent and indicated by the arrow in Figure 13b.

The results for the proud mortar support the findings for the proud shell and are summarized in the following. The time sections recorded along the x-profile, oriented perpendicular to the long axis of the mortar are presented in Figures 14 and 15. In both figures the resonance waves appear stronger than in the case of the shell. This observation is manifested by the spectrum in Figure 16a, which displays pronounced spectral maxima throughout the frequency range. Narrow (200 Hz) bandpass filtering for the spectral peak at 4,300 Hz, which constitutes less than 0.1 % of the maximum spectral energy, yields the time section displayed in Figure 16b. As seen before, coherent low frequency waveforms are visible throughout the section in addition to amplitude variations and phase shifts (see arrow in Figure 16b).

The data recorded along the y-profile, parallel to the long axis of the mortar, are presented in Figures 17 and 18. Again, some of the resonance waves are already visible concurrent with the direct reflected waves in the time section in Figure 17. The resonance waves in Figure 18 exhibit the same crossing pattern of the hyperbolas, generated by the scattering of the resonance waves off the opposing edges of the mortar, which was seen in the shell data before. The frequency spectrum of the time gated data, presented in Figure 19a, reveals distinct resonance peaks throughout the whole frequency range. In the current case the frequency peak at 5,850 Hz, representing approximately 0.4 % of the maximum spectral energy is select for narrow (200 Hz) bandpass filtering. The result is displayed in Figure 19b). As before, the moveout of the resonance waves is clearly visible throughout the time section superimposed by amplitude variations and phase shifts (see arrow in Figure 19b).

### 3.2.3    *Spectral Signatures*

While the resonance waves in the time domain can be used to detect and locate an object, the spectral properties of these waves can be used to characterize and identify it. To evaluate the dependence of the resonance peaks on the orientation of the object, the spectra computed for x- and y-profiles, perpendicular and parallel to the long axis of the UXO, respectively, are superimposed to assess the degree to which they correlate. Figure 20, reveals the first spectral pair for the data from the proud shell. The black and red lines represent the stacked spectra computed from the resonance waves along the x- and y- profile respectively. Both spectra were normalized before plotting. While the low frequency trend of the spectrum is governed by the spectrum of the source signal, most spectral peaks are related to the resonance waves interacting with the UXO. It is noted that there are 401 receivers located along the x-profile and 681 receivers along the y- profile, which translates to the red spectrum being supported by 70 % more data. Nevertheless, the comparison between the two spectra shows a good match for many resonance peaks particularly in the low and high frequency range, while at intermediate frequency the match is deceased. This suggests that the location of spectral peaks at low and high frequencies is independent of the orientation of the object when the source is located above.

The spectra derived from the mortar data recorded along the x- and y-profiles are presented in Figure 21. Again, a good correlation is visible between spectral peaks at low and high frequencies but even at intermediate frequencies a good match is apparent for several large spectral peaks.

These results are contrasted by the superposition of the spectra for the shell and mortar, each derived from data recorded along the x-profile as presented in Figure 22. It can be seen that the match of the spectral peaks is decreased in this case. While there is some degree of correlation at a few peaks, the match is far less pronounced than in the previous two examples. It appears that the two objects have different spectral signatures in data collected perpendicular to their long axes.

The final comparison is between the spectra for the shell and mortar derived from data recorded along the y-profiles. The result, presented in Figure 22, suggests a similar degree of poor correlation between the major resonance peaks throughout the spectral range. In this case even fewer peaks correlate between the two spectra.

Combining the results of Figures 22 and 23 it appears that the shell and mortar have distinct enough spectral features that a positive match can be ruled out. This suggests, however, that the observed size difference between the 0.417 m long 4-inch shell and the 0.52 m long 81-mm mortar, in combination with the different internal velocities, produces distinct resonance features to distinguish the objects from each other.

In contrast, the good correlation in the position of the spectral peaks for the data recorded along the x- and y-profile for the shell and mortar suggests some degree of independence on the orientation of the object with respect to the source and receiver

geometry. It is therefore likely that a method based on spectral matching could prove successful in characterizing the object. This idea should be pursued in future research.


# 4 Field Data

## 4.1 Geometry of the Field Experiment

Sonar data of proud UXO were acquired by the Applied Physics Laboratory (APL-UW), University of Washington, at the pond facility of the Naval Surface Warfare Center, Panama City (NSWC-PC), FL in 2007. The UXO-like objects included one 4-inch shell, one 81-mm mortar, one 500 lbs bomb and one sphere with a diameter of 0.6 m. The UXO targets had different filler material with varying density and P- and S-wave propagation velocities as summarized in Table 3; while the background properties of the water and pond sediments were summarized in Table 1 above.

| Object | Bomb | Shell | Mortar | Sphere |
|---|---|---|---|---|
| Length [m] | 1.680 m | 0.417 m | 0.520 m | 0.60 |
| Diameter [m] | 0.273 m | 0.102 m | 0.081 m | 0.60 |
| **Casing** | **Steel** | **Steel** | **Steel** | **Steel** |
| Vp [m/s] | 5,950 | 5,950 | 5,950 | 5,950 |
| Vs [m/s] | 3,240 | 3,240 | 3,240 | 3,240 |
| $\rho$[g/ccm] | 7. 85 | 7. 85 | 7. 85 | 7.85 |
| **Filling** | **Concrete** | **Iron** | **Concrete** | **Air** |
| Vp [m/s] | 3,560 | 5,920 | 3,560 | 330 |
| Vs [m/s] | 2,160 | 3,230 | 2,160 | 0 |
| $\rho$[g/ccm] | 2.4 | 7.87 | 2.4 | 1.2 |

**Table 3:** Physical properties of the UXO-like targets used during the pond experiment.

The geometry of the experiment is presented in Figure 24. A sonar tower, comprised of one source and 12 receivers, is mounted on a 20 m long rail positioned approximately 10 m across the proud target resting on the pond bottom (Figure 24a). During data acquisition the tower was moved in increments of 0.025 m for each shot position along the rail, which resulted in 750 recorded traces for each object. The data processing in the current report is based on six recording channels and one source location, as shown in Figure 24b. The source signal was comprised of a 4 ms long sweep with a bandwidth of 12 – 28 kHz, presented in Figure 25. Total data recording time was T = 30 ms at a sample rate of $\Delta t = 10^{-6}$ s, which translates to 30,000 samples per trace, a frequency interval of $\Delta f = 33.3$ Hz and a Nyquist frequency of $f_{ny} = 500,000$ Hz.


## 4.2 Data Processing

The first step in data processing consisted of pulse compression to transform the time delayed sweep into a compressed source signal. This was done by convolving each trace with the complex conjugate of the sweep signal in the frequency domain. Data processing in the previous chapter was done at very narrow passbands, which could have easily been applied to the field data without prior compression of the source sweep. However, in the current chapter we will also employ Kirchhoff migration, a technique equivalent to synthetic aperture sonar (SAS) imaging, which requires compressed data to improve image resolution in the time domain. Additionally, we intended to remove direct arrivals and unwanted reflections from other objects in the pond that were stored in the vicinity of the target field. The suppression of these data is based on gating in the time domain, which requires compressed pulses.

Imaging of the object is based on two different techniques. The first method, Kirchhoff migration, is equivalent to SAS imaging and has been employed extensively to image subterranean structure in oil and gas exploration for many years (Yilmaz, 1991). The imaging is performed in the time domain by integration over the amplitudes of the recorded wavefield. The equation for Kirchhoff migration is given by:

$$U(x, y, z) = \sum_i \frac{S_i\left(l_{s_i} + l_{r_i}/v\right)}{l_{r_i}}, \tag{1}$$

where $U(x,y,z)$ is the amplitude of the image at location $x$, $y$ in the image plane located at depth $z$; $S_i$ is the amplitude on the time trace; $v$ is the velocity of the medium; $l_{s_i}$ and $l_{r_i}$ are the distances from the source and receiver locations to the location $x$, $y$, $z$ in the image plane, respectively and $i$ is the trace index. The distances $l_{s_i}$ and $l_{r_i}$ are defined by:

$$l_{s_i} = \sqrt{\left(x - x_{s_i}\right)^2 + \left(y - y_{s_i}\right)^2 + \left(z - z_{s_i}\right)^2}, \tag{2}$$

and

$$l_{r_i} = \sqrt{\left(x - x_{r_i}\right)^2 + \left(y - y_{r_i}\right)^2 + \left(z - z_{r_i}\right)^2}, \tag{3}$$

where $x_{s_i}$, $y_{s_i}$ and $z_{s_i}$ are the coordinates of the source location while $x_{r_i}$, $y_{r_i}$, and $z_{r_i}$ are the coordinates of the receiver location.

In contrast, resonance migration is performed in the frequency domain, where the complex spectral values of the resonance frequency are summed of over all traces. The equation for resonance migration is given by:

$$F(M_k) = \sum_j \left| \sum_{n=1}^{N} s_{nj}^{*}(f_{res}) W_{nk}(f_{res}) \right|, \tag{4}$$

where $F(M_k)$ is the amplitude of the image at location $x$, $y$, $z$ in the image plane; $s_{nj}^*(f_{res})$ is the spectral component of data from source location $j$ and receiver location $n$; the star "*" denotes complex conjugation, $M_k$ represents the imaging location at $(x_k$, $y_k$, $z_k)$ and $W_{nk}(f_{res})$ is defined by:

$$W_{nk}(f_{res}) = \exp(i2\pi f_{res}\tau_{nk})/r_{nk}, \tag{5}$$

where $f_{res}$ denotes the resonance frequency; $r_{nk}$ is the distance from the receiver locations to the location $x$, $y$, $z$ in the image plane; $n$ is the receiver index and $\tau_{nk}$ the travel time defined for a homogeneous background velocity $v$ by:

$$\tau_{nk} = \frac{r_{nk}}{v}. \tag{6}$$

In the following equations (1) and (4) will be used to compute the Kirchhoff and resonance migration images, respectively.


## 4.3    Imaging the Proud Sphere

The first object to be imaged is an air-filled sphere with a diameter of 0.6 m. The wavefield for the proud sphere is displayed in Figure 25a, where the first 0.012 s have been muted to delete direct waves which dominate the wavefield in amplitude. The displayed traces combine the direct scattered waves, visible by the two pronounced hyperbolas (the first arriving at 0.0132 s and the second arriving at 0.0142 s) and resonance waves, which are visible as faint hyperbolas at 0.0152 s and 0.0162 s (see arrows in Figure 25a). The two hyperbolas for each wave group are related to reflections from the front and back of the sphere. The spectral composition of the data displayed in the time window of Figure 25a is presented in Figure 25b. Several resonance peaks are visible throughout the frequency range. The arrows indicate four resonance frequencies that will be further investigated in the following.

The resonance waves, filtered with a narrow (200 Hz) bandpass around 12,600 Hz, are displayed in Figure 26a. From the spectrum in Figure 25b it is evident that the energy at 12,600 Hz only represents 0.09 % of the maximum energy in the data. Nevertheless, the wavefield in Figure 26a reveals strong resonance waves with constant hyperbolic moveout across most of the profile. Considering the low amplitude value in the spectrum this is a remarkable result. A closer inspection of the traces along the tails of the hyperbola reveals phase shifts that were previously observed in the numerical data. Because the phase shift appears more concentrated around the edges of the object, it is possible that this phenomenon reflects interaction of the scattered waves between the object and the seafloor. Figure 26b shows the wavefield for a narrow bandpass around 16,000 Hz. Again, monotonic hyperbolas with constant moveout are visible across the profile. The increase in frequency is apparent by the shortening of time between adjacent wavefront maxima relative to the wavefield in Figure 26a. The results for the resonances

at 19,330 and 25,000 Hz are displayed in Figure 26c and 26d. Both wavefields reinforce the previous interpretations.

In the following, the wavefield displayed in Figures 25-26 will be migrated to from images of the sphere at different frequencies. The first image shown in Figure 27a is based on Kirchhoff migration using the complete wavefield as presented in Figure 25a. It is evident that the image is very sharp and that the sphere is presented by two maxima including energy in between. The two maxima are the result of migrating the two major hyperbolas visible in Figure 25a at arrival times of 0.0132 s and 0.0142 s. The maxima represent the focal points of reflections from the front and back of the sphere. The spatial resolution is good because of the bandwidth in the input data (see Figure 25a). In comparison, the result of the resonance migration for the 12,600 Hz resonance waves is presented in Figure 27b. It can be seen that the image is elongated in range (x-direction) but very narrow in cross range (y-direction). The maxima of the images in Figure 27a and 27b are co-located in cross range, while in range, the maxima of the resonance image is spread, covering the two maxima of the Kirchhoff migration. However, the two absolute maxima of the Kirchhoff and resonance migration are co-located in the target field. The resolution for resonance migration is reduced due to the monochromatic character of the input data (see Figure 26a). The resolution can be improved using multi-aspect data as shown in Chapters 4.6.3 and 4.7.

The imaging results of the resonance migration using the waveforms shown in Figures 26b (16,000 Hz), 26c (19,330 Hz) and 26d (25,000 Hz) are presented in Figures 27c, 27d and 27e, respectively. In can be seen that with increasing frequency the width of the maxima decrease until, for the case of 25,000 Hz in Figure 27e, the maxima splits into two parts, imaging the focal points of reflections from the front and back of the sphere, similar to the observation for the Kirchhoff migration in Figure 27a.

The results are remarkable for two reasons. The first is that the energy that the resonance migration is base on represents only 0.09 % of the maximum energy in the spectrum. The second is that the Kirchhoff migration utilizes the whole wavefield displayed in Figure 25a. The spectrum of the wavefield in Figure 25b shows non-zero amplitude values from 12 – 28 kHz. Considering the frequency interval of $\Delta f = 33.3$ Hz this translates to 480 frequencies that are stacked during Kirchhoff migration. Therefore, the resonance migration uses only 0.2 % of the data of the Kirchhoff migration. In other words; the duration of the source sweep was 4 ms as discussed at the beginning of Chapter 4. If a constant phase is assumed, this translates to a source time of only 83 $\mu$s per frequency. Thus, the image of the proud sphere is based on 1/480th of the data with an energy level of only 0.09 % of the maximum energy available for Kirchhoff migration. The implications of this finding will be discussed at the end of Chapter 4.

## 4.4  Imaging the Proud Mortar

The mortar data processed during the current project were taken from an 81-mm mortar located proud off the seafloor with its fins attached. A representative picture from

file (not the actual mortar used during the experiment) is shown in Figure 28, to demonstrate its shape and the location of its fins along the tail.

The data displayed in Figure 29a were acquired while the tip of the mortar was pointing towards the rail. The wavefield includes the waves directly scattered off the object and the following resonance waves. The amplitude spectrum, shown in Figure 29b, follows the general trend of the source spectrum superimposed by resonance peaks. In the following, resonance waves and migration images of three frequencies will be presented. The resonance waves obtained with a narrow (200 Hz) bandpass filter around 13,000 Hz are presented in Figure 30a. The hyperbolic moveout of the resonance waves is evident across the profile, while phase shifts become more apparent. This observation will be revisited during the discussion of the migration images below. The wavefield generated by the narrow (200 Hz) bandpass filter around 16,000 Hz is presented in Figure 30b. The wavefronts of the resonance wave still display a hyperbolic moveout but the amplitudes are not symmetric across the profile any longer. This trend is reinforced by the results of the bandpass filter centered on 20,800 Hz in Figure 30c. The wavefronts are continuous only between trace numbers 365 and 425. At the same time, phase shifts are visible throughout the wavefield at most receiver locations.

The results for Kirchhoff migration are presented in Figure 31a. It can be seen that the maximum amplitude of the image is reduced to a single point in the target field. The maximum is likely associated with the locations of the fins on the tail of the mortar. The planar structure of the fins represents a good reflector for scattered waves. Similar results were reported by Kargl et al. (2009). In comparison, the image of the resonance migration for 13,000 Hz is given in Figure 31b. Similar to the case of the sphere, an elongated image is visible with the maximum co-located in space with that of the Kirchhoff migration. Furthermore, the image appears to be composed of two branches slightly offset from each other. The picture becomes clearer at 16,000 Hz, when two equally larger maxima develop toward the tip and the tail of the mortar. This trend is supported by the image at 20,800 Hz, when the two maxima separate more clearly. It is likely that the two maxima are related to scattering off the tip and the tail fins of the mortar. Furthermore, the slight angle visible for the migrated resonance images suggest that the mortar was not aligned perfectly perpendicular to the rail. Reasons for this include poor visibility in the pond caused by bad weather conditions (Lim, personal communication, 2009). The angle in mortar orientation is the likely cause for the non-symmetric amplitude distribution in the wavefronts of the resonance waves in Figures 30b and 30c. The orientation of the mortar amplifies reflections in the direction of the rail that recorded the larger amplitudes in the resonance waves (i.e., the traces with higher numbers are recorded by the receivers positioned at negative y-coordinates).

Phase shifts in the resonance waveforms were observed in numerical data for symmetric cylinders on a flat interface as well as in the pond data for the proud sphere and the mortar resting on a flat pond bottom. In contrast, phase shifts were less apparent in numerical and field data for a buried cylinder under a sinusoidal interface, as will be shown in the appendix. It is plausible that the interaction of the waves between the objects and the flat seafloor, or in the case of the mortar, between the flat fins causes the

observed phase shift in the resonance waveforms. This phenomenon might be amplified in the monochromatic resonance data as interference pattern might be more apparent.

## 4.5    Imaging the Proud Shell

The processed shell data were taken from a 4-inch artillery shell located proud off the pond bottom. A sample picture of a typical 4-inch shell (not the actual shell used during the experiment) is shown in Figure 32. Note the pointed nose at the top and the flat round end at the tail of the shell.

For reasons of brevity, only the migrated images are shown for the shell as the intention of this section is to show how resonance waves of different frequencies interact with distinct parts of the object.

During data acquisition for the results presented below, the proud shell was oriented with the nose in negative y-direction. The Kirchhoff migrated image of the shell is shown in Figure 33 a. The image is comprised of two maxima oriented parallel to the rail with the larger maximum pointing in negative y-direction. The result is expected, because the nose of the shell represents a near perfect point scatterer that will generate coherent amplitudes along hyperbolas in the recorded waveforms. Consequently the weaker maximum pointing in positive y-direction is related to the flat tail of the shell. In contrast, the result of the resonance migration bandpassed around 19,100 Hz reveals an amplitude maximum near the tail of the shell as presented in Figure 33b. The reason is that resonance waves at this frequency interfere constructively with the tail of the shell. When the frequency is increased to 20,200 Hz, however, the amplitude maximum appears on the nose side of the shell in the same location as for the Kirchhoff migration. This trend is reinforced in the last example using a resonance frequency of 26,900 Hz. The migration generates a maximum with even higher resolution in the same location, reinforcing the interpretation that this is the nose of the shell. In addition to the two maxima, the resonance migrated image displays the typical elongated amplitude structures delimiting the tip and tail of the shell and thus its length of 0.417 m in between.

This example reveals the flexibility of resonance imaging in that it may illuminate different parts of the object with different frequencies and help to interrogate the object by forming multiple resonance images.

## 4.6    Imaging the Proud Bomb

The field data for the 500 pound bomb was acquired in two orientations relative to the recording rail. For the first dataset analyzed below, the bomb was oriented parallel to the rail, with the tip pointing in negative y-direction. For the second dataset, the orientation of the bomb was rotated by 90 degrees with the tip pointing toward the rail. A file picture of two representative 500 pound bombs is presented in Figure 34. It is noted that these objects were not used in the field experiment, but are representative in that they

demonstrate the geometry of this UXO with a cone-shaped tip and a narrowing but flat tail.

For reasons of brevity, only the migrated images are shown in the following as the intention of this section is to show how resonance waves interact with objects of different orientation and how different acquisition geometries can be used to sharpen the image.

### 4.6.1 Orientation Parallel to Rail

The first image of the bomb oriented parallel to the rail is based on Kirchhoff migration and is presented in Figure 35a. The image is correctly oriented and comprised of several amplitude maxima. These are likely resulting from variations in amplitudes of the reflected waves due to the shape or reflective strength of the target, although interference of the waves between the seafloor and the target can also be a reason. The first resonance migrated image, shown in Figure 35b, was generated with a frequency of 20,120 Hz. The image reveals a different character with a broad amplitude structure and a maximum along the right edge. While the lower amplitudes of the image result from interaction of the resonance waves with the central part of the bomb, the maximum on the right edge (at y = 1m) is related to resonance scattering off the tail end of the bomb (compare to image in Figure 35a). Increasing the resonance migration frequency to 25,960 Hz results in the image presented in Figure 35c. The image reveals two amplitude ridges with the weaker one on the right at the location of the maximum discussed in Figure 35b. The maximum in Figure 35c has moved towards the tip of the bomb but it is likely not co-located with the tip yet. The reasons include the length of the bomb, which is longer that the separation of the amplitude ridges in Figure 35c and because the two imaging frequencies are not that different while the tip of the bomb is noticeably smaller than the tail section.

### 4.6.2 Orientation Perpendicular to Rail

The second set of images from the proud bomb is derived by rotating its orientation such that the tip is pointing toward the rail (i.e., its longer axis is perpendicular to the rail system). The image derived from Kirchhoff migration is presented in Figure 36a. It is composed of several amplitude maxima, with the strongest one in the center. The range extent of the maxima reaches from 9 m to approximately 10.5 m which is close to the length of the bomb. Additionally, the long axis of the bomb is slightly rotated clockwise. The resonance migrated image for 18,070 Hz is shown in Figure 36b. A very narrow amplitude ridge with two maxima is visible. The first maximum is located between 9 m and 10 m range, while the second one is located between 10 m and 11 m range. These two maxima coincide with the front and back part of the Kirchhoff migrated image. However, the orientation of the image in this picture appears rotated counter clockwise. The resonance migrated image for 19,340 Hz is given in Figure 36c. The image appears changed in that the front maximum is still visible,

while the amplitude of the second maximum has decreased. However, the orientation of the image is now rotated clockwise.

The imaging of the bomb has provided another example how resonance imaging illuminates different parts of the object under interrogation. This part needs further study to determine, for example, which resonance frequencies in the observed spectra are stable under varying incidence angles.

### 4.6.3   Combination of Two Recording Geometries

The availability of two datasets for the elongated bomb under two orientations has provided the opportunity to demonstrate the improvement of resonance imaging for data with different azimuth (multi-aspect data). The idea behind this concept is to improve the limited resolution of the resonance images in range direction by adding data acquired in cross range direction, for example. The idea is illustrated in Figure 37, which shows two rail configurations. The first configuration depicts the current situation, where the proud bomb is oriented parallel to the recording rail (Figure 37a). If a second rail, perpendicular to the first, was available for data acquisition, the target could be insonified at an azimuth of $90^{o}$ compared to the first geometry (Figure 37b). This concept can be demonstrated with the dataset of the bomb oriented with the tip to the original rail. In this case, the x- and y-coordinates of the source and receiver positions along the rail need to be exchanged followed by migration of the resonance waves. This process is equivalent to rotating the image obtained with the original geometry by $90^{o}$. Once the two single images are superimposed the resulting image reveals much higher resolution. This concept will be demonstrated in the following

The first image is taken from the resonance migration at 25,960 Hz (originally presented in Figure 35c) and redisplayed in Figure 38a. This image was obtained for the bomb oriented parallel to its axis. The second image is taken from the resonance migration at 19,340 Hz (originally presented in Figure 36c), which was obtained with the bomb oriented perpendicular to the rail. This image is subsequently rotated by $90^{o}$ and redisplayed in Figure 38b. The rotated image would be obtained with a source-receiver geometry as presented in Figure 37b. The superposition of the two images results in the resonance image presented in Figure 38c. It is apparent that the superposition greatly improves the resolution in range direction. This example is a simplified concept to demonstrate how the resolution of resonance imaging can be improved by combining data from different azimuth. This concept is also applied in section 4.7.

### 4.6.3   Spectral Signatures of Perpendicular Bomb Orientations

The availability of datasets with two perpendicular bomb orientations provides the opportunity to study the robustness of the spectral features observed in the resonance waves as a function of target orientation. The recorded wavefields for the bomb oriented parallel and perpendicular the rail are presented in Figure 39a and 39b, respectively. Of the total wavefield only the direct reflected waves and a section trailing these waves are presented in the figure. The waves reflected off the bomb oriented parallel to the rail reveal strong amplitudes with smooth hyperbolic moveout visible just before 0.014 s in the wavefield for duration of about 0.0005 s (Figure 39a). In contrast, the wavefield for the bomb oriented perpendicular to the rail reveals a stronger hyperbolic moveout, because the tip of the bomb represents a point scatterer. At the same time, the two end points of the bomb located at different distances from the rail produce separated hyperbolas over a time interval of approximately 0.002 s in the wavefield (Figure 39b). To improve the visibility of the resonance waves, amplitude gain control with a 0.005 s window length was applied to both wavefield sections. The white rectangles indicate the data that were selected for the following spectral analysis. The arrows point to the amplitudes of the resonance waves visible by their hyperbolic moveout. The variations in amplitude across the traces are likely due to interactions of the waves between the UXO and seafloor as well as variation is scattering strength caused by variation in the incidence angle due to the curvature of the bomb. However, the coherency of the resonance waves is similar to the coherency of the respective direct reflected waves in Figure 39a and 39b.

The amplitude spectra of the source sweep and the resonance scattered waves for the two bomb orientations are presented in Figure 40. The spectra of the resonance waves for the two bomb orientations show a remarkable match throughout the spectral band. The overall trend of the resonance spectra is dominated by the source spectrum (see Figure 40a for comparison), while the spectral peaks are likely cause by the interaction of the incidence wave with the UXO. Attenuation in the medium helps to compare the two spectra by damping and broadening some of the peaks as compared to the numerical data presented earlier, which lacked intrinsic attenuation and showed a multitude of narrow peaks.

To exclude the possibility that the spectral features in Figure40b are generated by scattering off the pond bottom, the analysis is repeated for representative noise in the data. Figure 41 shows the wavefields presented in Figure 39 including earlier times prior to the arrival of the direct reflected waves. Representative noise data are selected prior to the arrival of the direct scattered waves to avoid interference with the latter. The data selected for spectral analysis are indicated by the white rectangles. The superposition of the two noise spectra is presented in Figure 42, which also displays the spectrum of the source sweep for easier comparison. It can be seen that the noise spectra closely match the trend of the source spectrum without exhibiting the spectral features observed for the two bomb orientations in Figure 40b.

The results of the spectral analyses indicate that characterization of UXO may be independent of the orientation of the object. It is noted that the presented results were derived with the bomb rotated in place, relative to the source-receiver geometry along the rail. Therefore, this finding needs to be further investigated with multi-aspect data that

allow studying the spectral features of a stationary object insonified from different azimuth.


## 4.7    Estimating Velocities of the Background Medium

Physical properties of the background medium are necessary parameters required to correctly detect, locate and characterize UXO in littoral environments. The propagation velocity of sonar waves in water and the seafloor are essential to from accurate images of the object at the correct location. In the past sections, migration (imaging) techniques have been employed to create images of the UXO under interrogation. Because these techniques rely on background velocities, they can be used to estimate the correct medium velocity. This approach is typically applied in oil and gas exploration and in acoustic imaging. In the following, the applicability of this approach for resonance migration will be described by revisiting the case of the proud sphere.

As a starting point for this exercise, the resonance migrated image for the proud sphere at 16,000 Hz is shown in Figure 43 again. As previously stated, the two-dimensional image shows a maximum at the location of the sphere, with decaying amplitudes in the range (x) direction (Figure 43a). A three-dimensional surface plot of the two-dimensional image is presented in Figure 43b. The topography clearly shows the peaked maximum at the location of the sphere. If, in addition to the present data acquired along the rail (range direction), measurements were also available in cross range direction (in field situations this could be achieved by an AUV that insonifies the object from different azimuth) the migration images would be more focused as the elongated decaying amplitudes visible in Figure 43a would interfere destructively. This concept has been applied to the images in Figure 44 where the x- and y-coordinates of the source and receiver positions along the rail in range (y) direction were exchanged to mimic the situation of data acquisition in cross range (x) direction. This process is equivalent to rotating the image in Figure 43a by 90$^{o}$. The result of the resonance migration with a frequency of 16,000 Hz is a much sharper image resulting from the superposition of the two dataset, which dramatically reduces the decaying amplitudes surrounding the maximum that were caused by limited geometrical aperture in Figure 44a. The surface plot of the new image reveals the dramatic improvement in resolution in Figure 44b. This image will be the basis for estimating background velocities.

If the background velocity of the water was not exactly known, the results of the resonance migration would be quite different. Figure 45 shows the outcome of a migration attempt assuming a propagation velocity of 1,432 ms/, a 50 m/s reduction of the true background velocity. The resulting images exhibit two properties. The first is a slight shift of the maximum farther away from the source and receiver positions, due to the lower migration velocity. The second, more apparent change is a defocusing effect of the migrated object, because the stacking of the resonance waves during migration produces lower amplitudes of the resulting image that are spread out farther in space. This effect is best visible in Figure 45b. The results become more pronounced, when the water velocity is underestimated by 100 m/s resulting in a background velocity of 1,382

m/s as for the case presented in Figure 46. In this case, the shift in maximum amplitude and defocusing of the image become quite apparent even in the two-dimensional images. It can be seen that two maxima formed, which have shifted out farther from the original focal point. Furthermore, the decaying amplitudes surrounding the maxima are also spread farther from the original focal point, which can easily be seen in Figure 46b.

The examples above show how resonance migration can be used to estimate the correct propagation velocity of the background medium. A range of velocities that include the correct value will produce a suite of images that are progressively defocused the more the migration velocity differs from the correct value. Therefore, the sharpest migration image will yield the correct medium velocity. This approach is independent of the number of objects imaged, because the principle of focusing and defocusing is universal.

## 4.8    Implications for Resonance Migration

The results so far have shown that resonance imaging with monochromatic data is viable at very low amplitude values. In the examples above it was shown that with a fraction of the amplitudes typically used for Kirchhoff migration, or SAS imaging, an image can be formed that identifies the location of UXO. There are several advantages of using resonance imaging. The ability to image at low frequencies allows deeper penetration in seafloor sediments. The fact that the presented results were obtained with 0.2 % of the data available to Kirchhoff migration in addition to much smaller signal amplitudes suggests that monochromatic source signals with longer duration time (i.e. comparable to the 4 ms sweep time) would dramatically increase the signal-to-noise ratio. Studies in active monitoring in earth sciences have been performed where stacking of very small monochromatic signals can be detected at observational distances of several hundred kilometers (Kasahara et al., 2010). Consequently it would be possible to image a range of objects in sediments, including smaller and deeper targets and objects with less acoustic contrast, that would not be visible when illuminated by a broadband signals.

Data acquisition in the field can be conducted by interrogating the medium with a series of pulses with narrow spectral width to excite various resonances from the UXO under interrogation. The duration of the pulses can be similar to typical source times, because the narrow frequency band ensures that more energy is radiated into the medium at the specified frequencies.

Range resolution, as seen in the examples presented in Chapter 4, is reduced when imaging is done with monochromatic signals. However, the image resolution can be dramatically improved by adding data from different azimuth. In field application this can be achieved by an AUV that navigates partially around the object. It is noted however, that the images obtained with resonance migration are intended for detection and localization only, because characterization of the object should by done by matching the distinct peaks in the amplitude spectrum of the data. To achieve this goal, a database with typical UXO-shaped objects located in sediments needs to be compiled, to include

the effect of intrinsic attenuation that cannot be modeled very easily with the current knowledge and computational resources.

# 5    Conclusions

The main implications of this limited-scope project can be summarized as follows:

- Resonance migration was successful for all investigated proud and buried UXO as long as the approach is based on resonance peaks observed in the amplitude spectrum.
- A very small fraction ($< 0.5$ %) of energy in the wide frequency band emitted by the UXO is sufficient to form an image.
- UXO generate object specific spectral signatures with unique sets of resonance peaks.
- Resonance migration can be used to estimate the correct propagation velocity of the background medium using the fidelity of the image to appraise the estimate.
- Single-frequency sonar signals of typical source duration should enable deeper penetration into the seafloor expanding the current list of targets to include deeper and much smaller objects as well as objects with reduced acoustic contrast to the background medium.
- Results of resonance imaging can be improved with data recorded from varying azimuthal orientations and by taking source radiation and receiver sensitivity pattern into account.
- Resonance migrated images are intended for detection and location only, while discrimination is intended through matching of spectral signatures.

# 6    Acknowledgement

# 7      Literature

Brill, D., Gaunaurd, G., Uberall, H., 1982, Sonar Target-Identification by Means of an Acoustic Spectroscopy Scheme, *Oceans*, Vol. 14, pp. 123-128.

Bucaro, J.A., Houston, B.A., Saniga, M., Nelson, H., Yoder, T, Kraus, L. and Carin L., 2007a, Wide Area Detection and Identification of Underwater UXO Using Structural Acoustic Sensors, *Annual Report, SERDP Project Number MM-1513*.

Bucaro, J.A., Houston, B.A., Saniga, M., Nelson, H., Yoder, T, Kraus, L. and Carin L., 2007b, Broadband, Multi-Aspect Scattering Measurements from Shells, Rockets and False Targets in the Structural Acoustic Domain, *Partners in Environmental Technology Technical Symposium and Workshop, Washington, D.C.*

Cobb, W. (2006), Acoustic identification of filler materials in unexploded ordnance, *Final Report*, SERDP Project MM-1382.

Gaunaurd, G.C., 1992, Active Acoustic Classification via Transient Resonance Scattering, *Optical Engineering*, Vol. 31, Thompson, B.J., ed. pp. 2553-2561.

Gritto, R., V.A. Korneev V.A., and L.R. Johnson, 2009, Detection of Underwater UXO Using Resonance Scattered Sonar, *The Forum, 2009, Orlando, FL,* Aug. 24-27.

Gritto, R., V.A. Korneev V.A., and L.R. Johnson, 2009, Detection and Classification of Underwater UXO Using Resonance Scattered Sonar, *Partners in Environmental Technology Technical Symposium and Workshop, Washington, D.C.,* Dec. 1-3, 2009.

Gritto, R., Korneev, V. A. and Johnson, L. R., 1995, Low frequency elastic wave scattering by an inclusion - Limits of applications, *Geophys. J. Int.*, 120, 677-692.

Houston, B.H.; Bucaro, J.A.; Yoder, T.; Kraus, L.; Tressler, J.; Fernandez, J.; Montgomery, T.; Howarth, T., 2002, Broadband Low Frequency Sonar for Non-Imaging Based Identification, *Oceans*, Vol. 1, pp. 383-387.

Houston, B.H., Bucaro, J.A., Saniga, M., Simpson, H., Nelson, H., Yoder, T, Kraus, L. and Carin L., 2009, Broadband, Multi-Aspect Scattering from UXO, *Partners in Environmental Technology Technical Symposium and Workshop, Washington, D.C.,* Dec. 1-3, 2009.

Kasahara, J., V, Korneev and M. Zhdanov, editors, 2010, Active Geophysical Monitoring, Vol 40, *Handbook of Geophysical Exploration: Seismic Exploration,* Klaus Helbig and Sven Treitel. The Netherlands, Elsevier, 2010, pp. 5-28.

Kargl, S., Espana, A.L., Williams, K.L., 2009, Underwater UXO Detection and Classification via Synthetic Aperture Sonar and Acoustic Templates, *Partners in Environmental Technology Technical Symposium and Workshop, Washington, D.C.,* Dec. 1-3, 2009.

Korneev, V., 2009, Resonant seismic emission of subsurface objects, *Geophys.*, Vol. 74, No 2, pp. 47-53, 10.1190/1.3068448.

Korneev, V.A. and E. Landa, 2007, Imaging of Subsurface Objects Using Resonant Emission, *Society of Exploration Geophysicist Annual Meeting,* San Antonio, TX.

Korneev, V. A., and Johnson, L. R., 1996 , Scattering of P and S waves by spherically symmetric inclusion, *Pure and Appl. Geophys.*, 147, No.4, pp. 675-718.

Lim, R., Lopes, J., Paustian, I., Arrieta, R., Dobeck, G., Burnett, D., 2009, Pond Measurements to Investigate Sonar Detection and Classification of Underwater

UXO, *Partners in Environmental Technology Technical Symposium and Workshop, Washington, D.C.,* Dec. 1-3, 2009.

Runkle, P., Carin, L., Couchman, L., Yoder, T.J., and Bucaro, J.A., 1999a, Multi–Aspect Identification of Submerged Elastic Targets via Wave–Based Matching Pursuits and Hidden Markov Models, *J. Acous. Soc. Am.*, Vol. 106, pp. 605–616.

Runkle, P., Carin, L., Couchman, L., Yoder, T.J., and Bucaro, J.A., 1999b, Multi–Aspect Target Identification with Wave–Based Matching Pursuits and Continuous Hidden Markov Models, *IEEE Trans. Pattern Analysis and Machine Intelligence*, Vol. 21, pp. 1371–1378.

Yilmaz, Ö, 1991, Seismic Data Processing, *Investigations in Geophysics*, Vol. 2, SEG, Tulsa, OK, pp. 526.

## 6    Figures
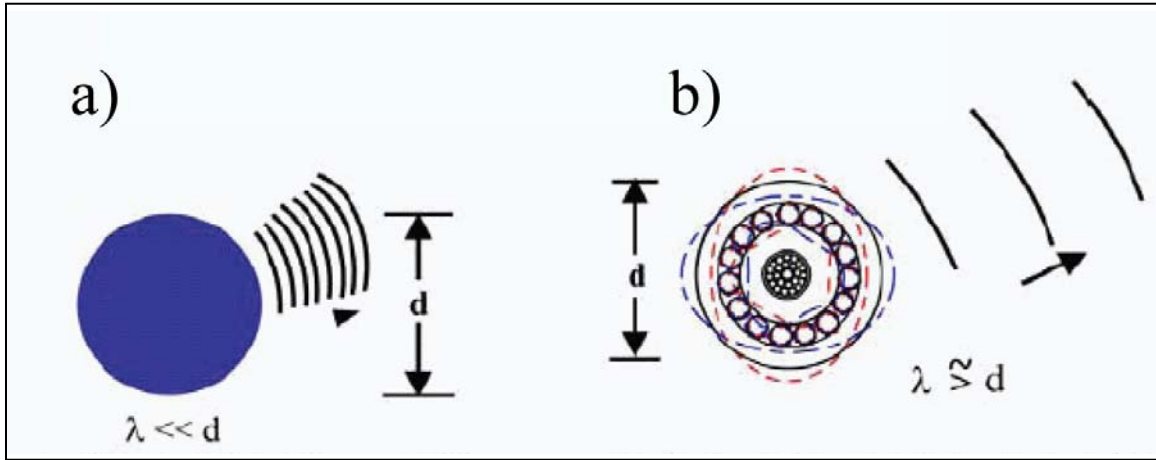


**Figure 1: a)** High frequency scattering of waves by a spherical object. The wavelengths of the incidence and reflected waves are much smaller than the dimensions of the object. **b)** Low frequency resonance scattering of waves by a spherical object. The wavelengths of the incidence and scattered waves are comparable to the dimensions of the spherical object (after Bucaro, 2007a).
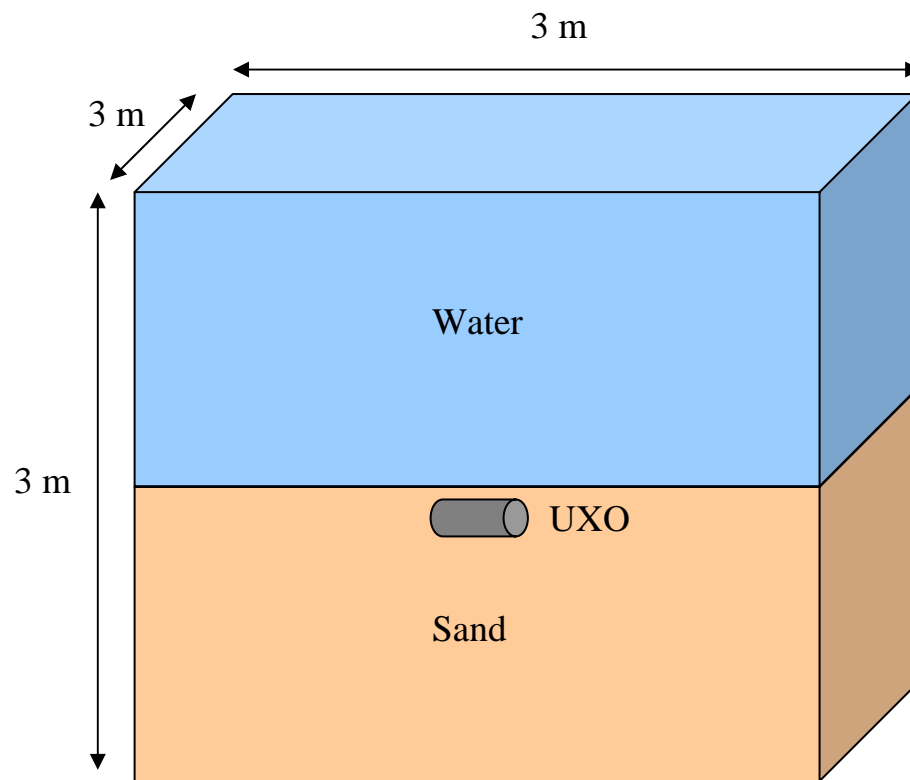
**Figure 2:** Geometrical sketch of the 3-D finite difference model.
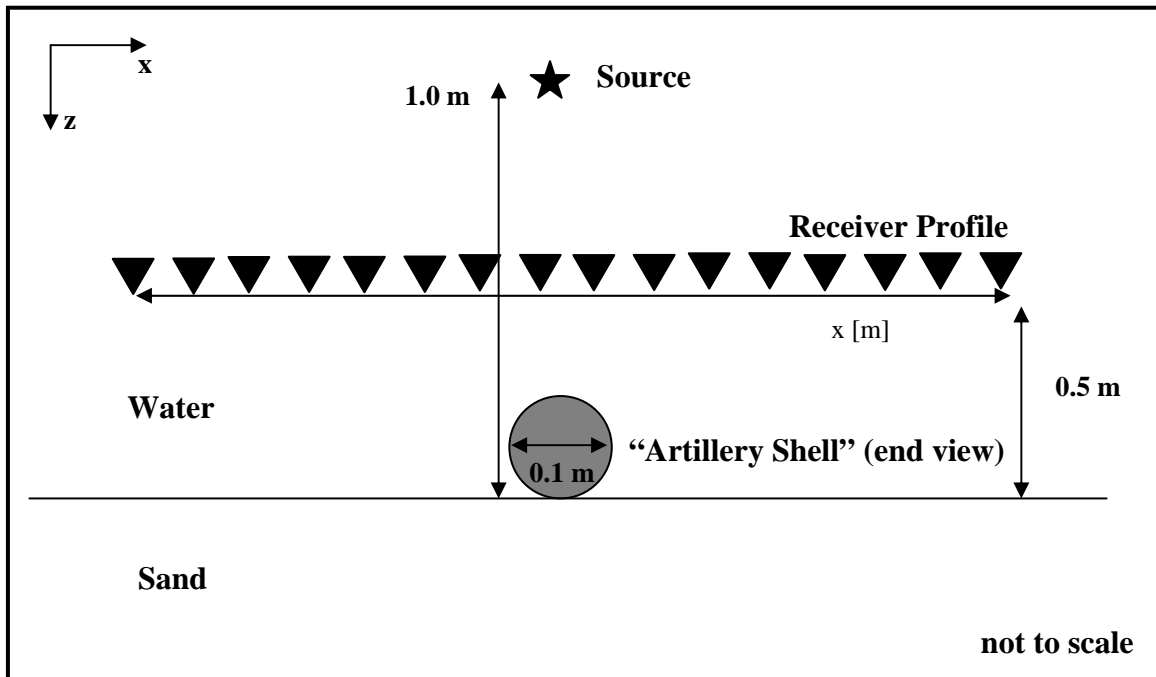
**Figure 3:** Two dimensional vertical view of the finite difference model for proud UXO geometry. Viewing plane is perpendicular to the long axis of the artillery shell. The 4-inch caliber shell was modeled by a cylinder with 0.1m diameter and length of 0.415 m. The 2 m long receiver profile consists of 401 receivers at 0.005 m spacing.
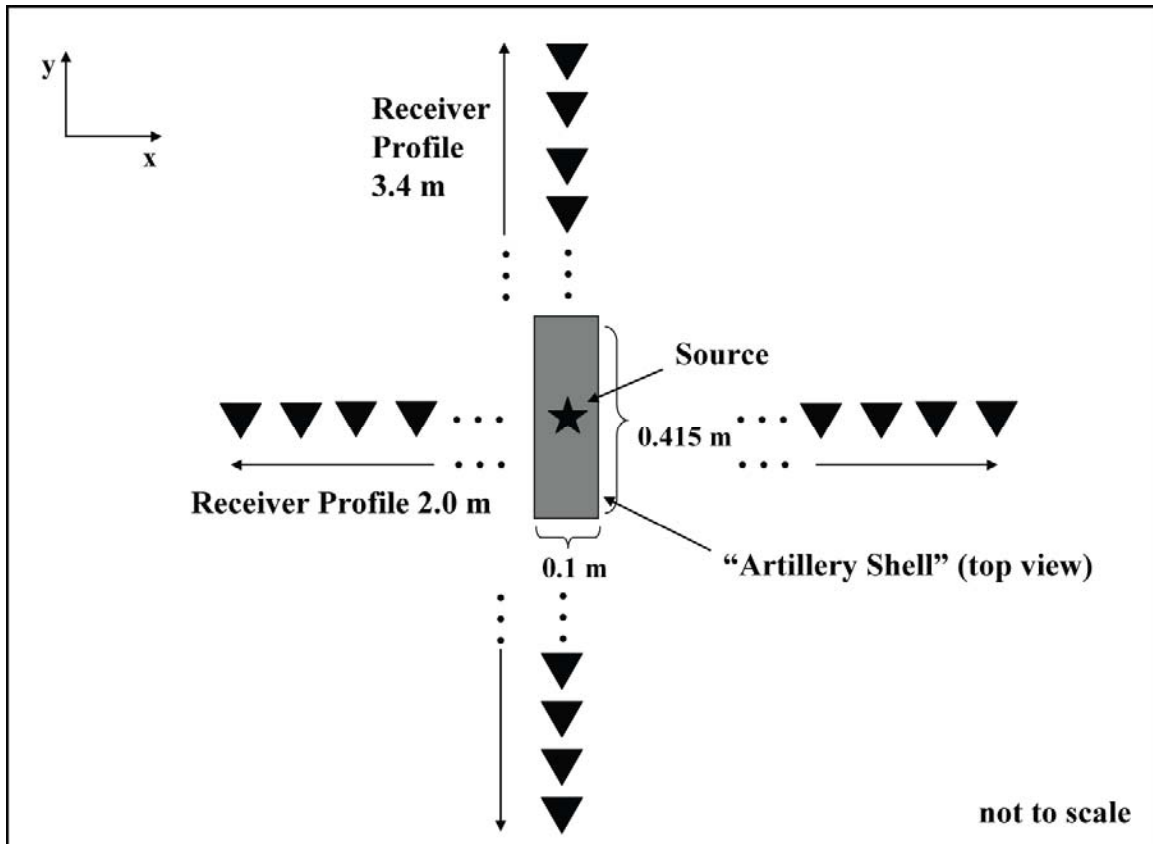
**Figure 4:** Two dimensional horizontal view of the finite difference model for proud UXO geometry. Viewing plane is parallel to the long axis of the artillery shell. The 4-inch caliber shell was modeled by a cylinder with 0.1m diameter and length of 0.415 m. The two receiver profiles in x- and y-direction consist of 401 and 681 receivers, respectively, each spaced at 0.0005 m.
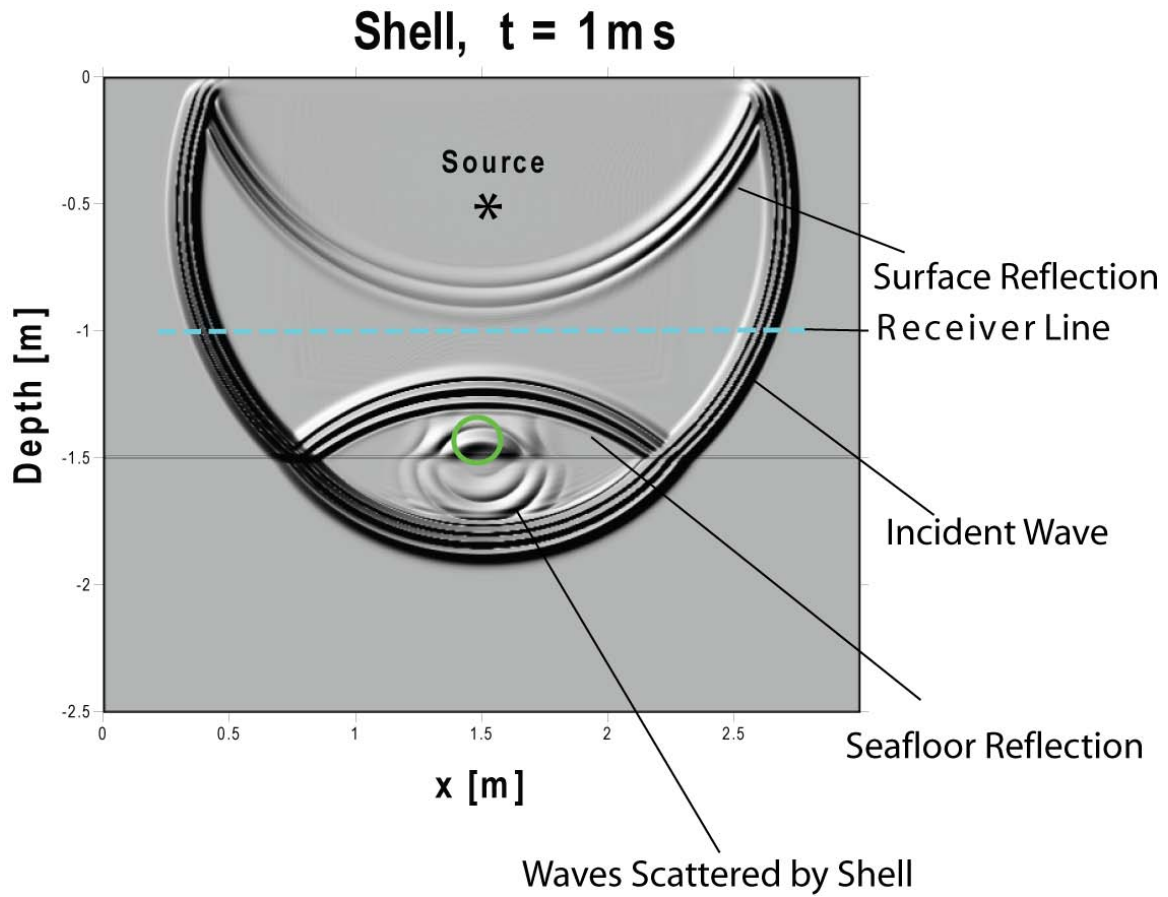
**Figure 5:** Early time snapshot (t = 1 ms) of the wavefield perpendicular to the long axis of the 4-inch shell located proud of the seafloor. The dominant phases include the incident wave, reflected waves off the water surface and seafloor interface and waves scattered by the shell (green circle) into the seafloor and back into the water column.
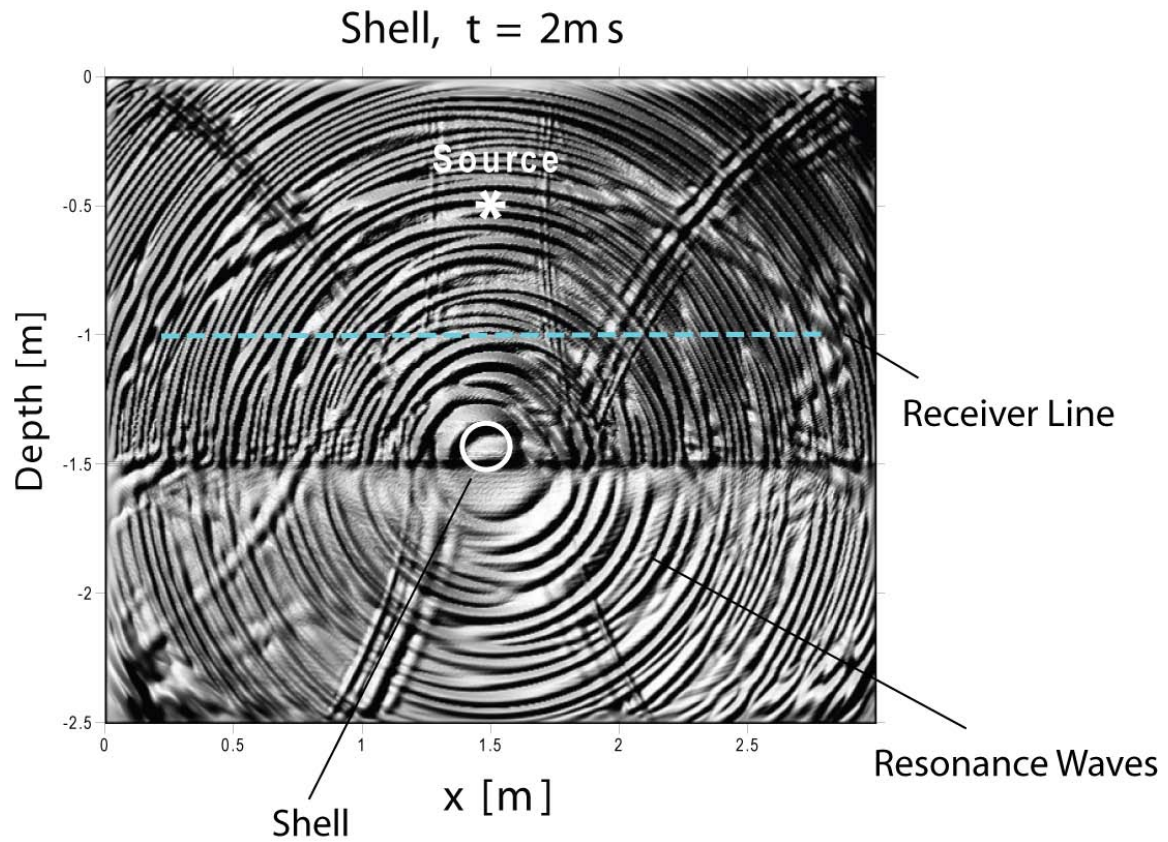
**Figure 6:** Intermediate time snapshot (t = 2 ms) of the wavefield perpendicular to the long axis of the 4-inch shell located proud of the seafloor. The dominant phases include insufficiently attenuated waves reflected off the model boundaries (x-shaped moveout) and resonance scattered waves, recognizable by their concentric wavefronts around the shell.
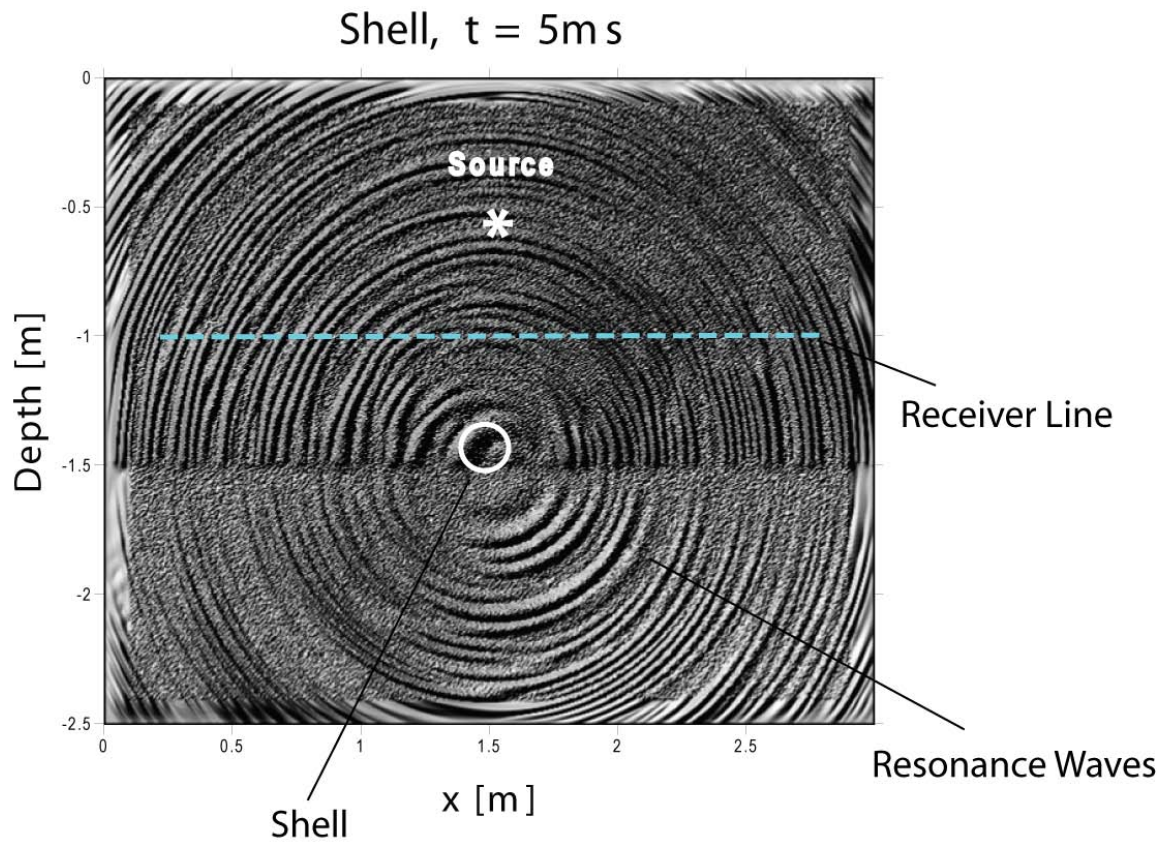
**Figure 7:** Late time snapshot (t = 5 ms) of the wavefield perpendicular to the long axis of the 4-inch shell located proud of the seafloor. The wavefield is dominated by resonance scattered waves radiating concentrically from the shell on the seafloor.
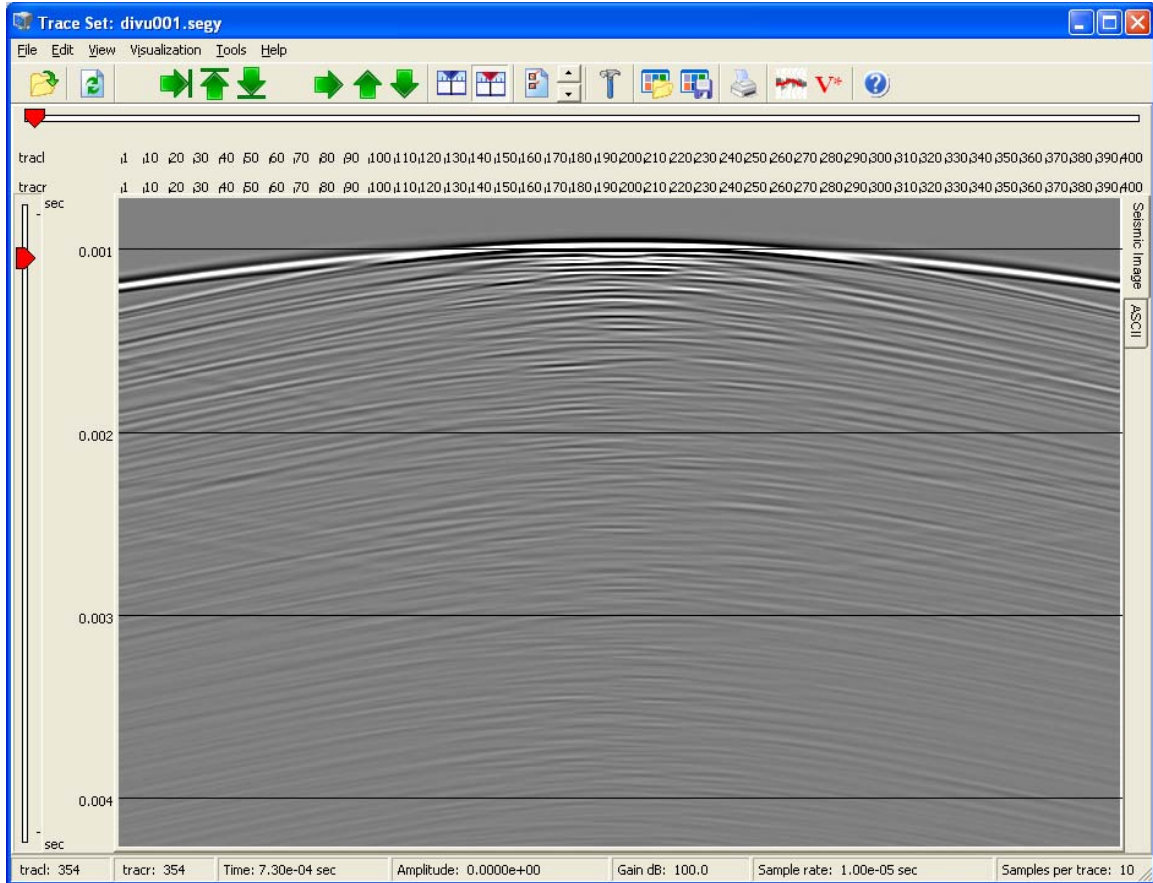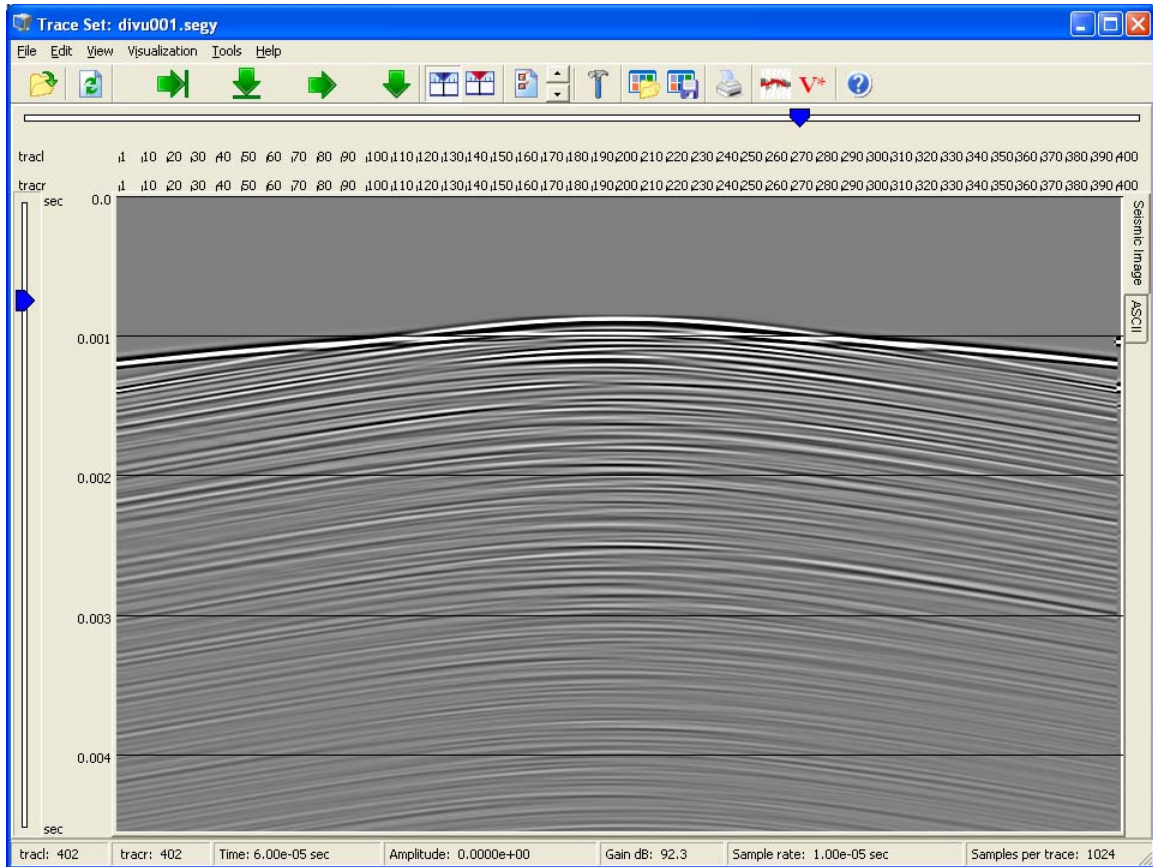
**Figure 8:** Time section of waveforms recorded for the proud shell recorded with the receiver profile in x-direction (refer to Figure 4). The wavefield is muted before 0.0009 s to suppress the large amplitudes of the direct waves. The large hyperbolic wave arriving at 0.001 s are the waves directly reflected off the shell, while the faint later arrivals represent resonance waves.
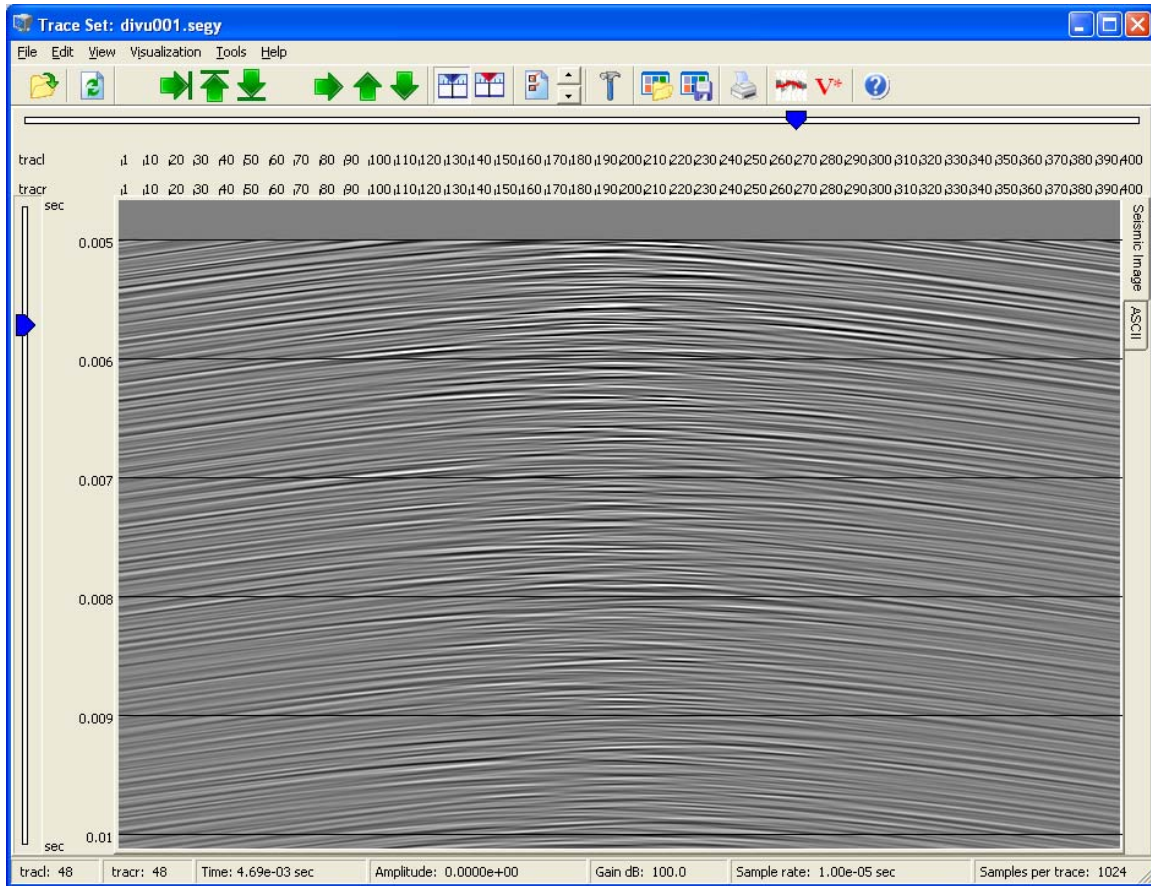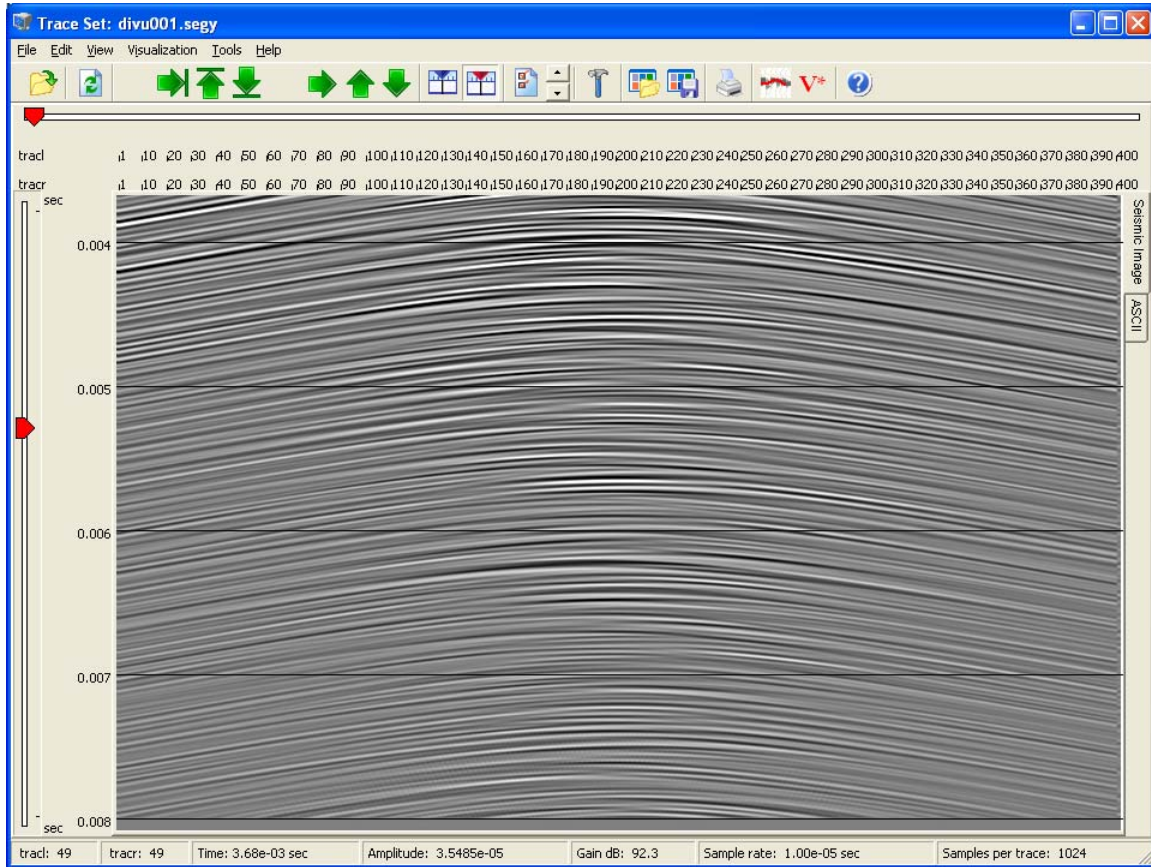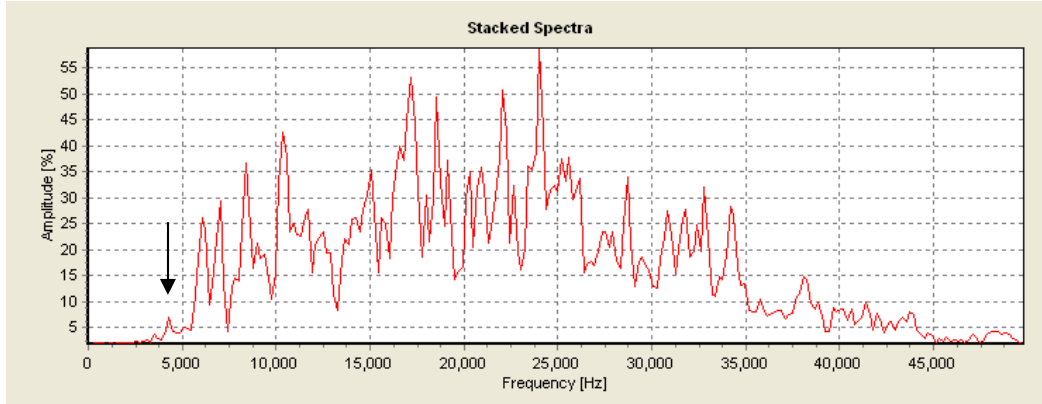
**Figure 9:** Time section of waveforms recorded for the proud shell with the receiver profile in x-direction (refer to Figure 4). The wavefield is muted before 0.005 s to suppress the amplitudes of the waves directly scattered off the shell. The hyperbolic wavefronts visible throughout the time section are resonance waves scattered off the shell.
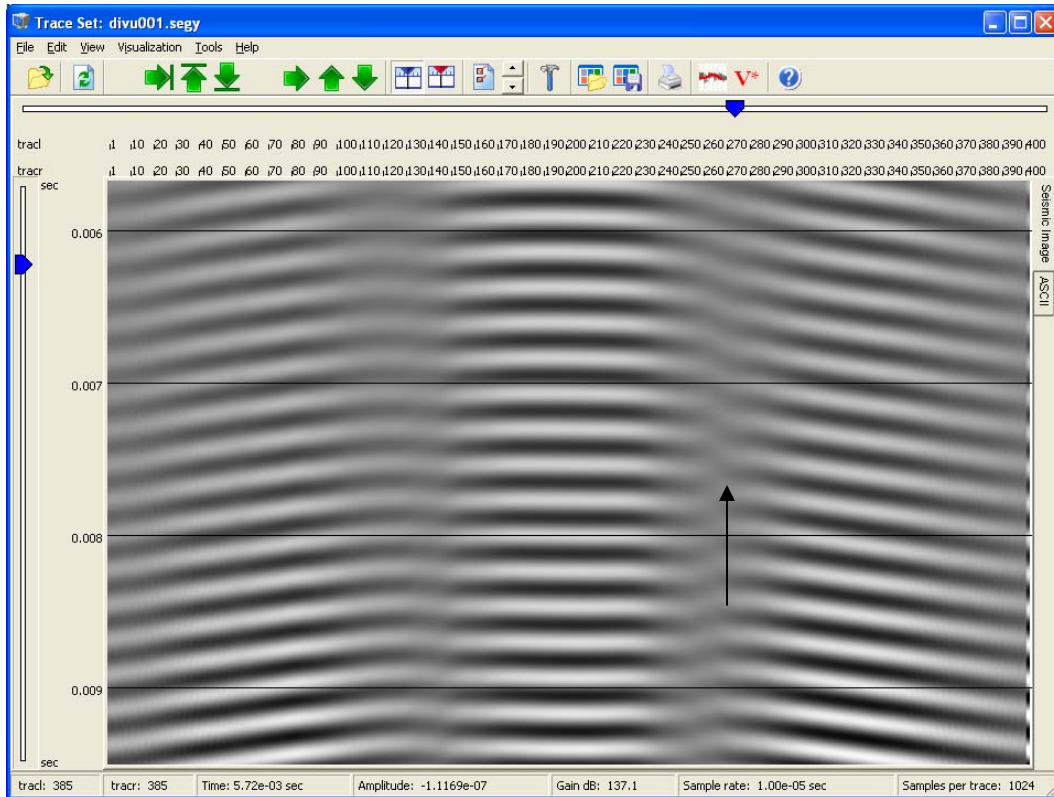
**a)**
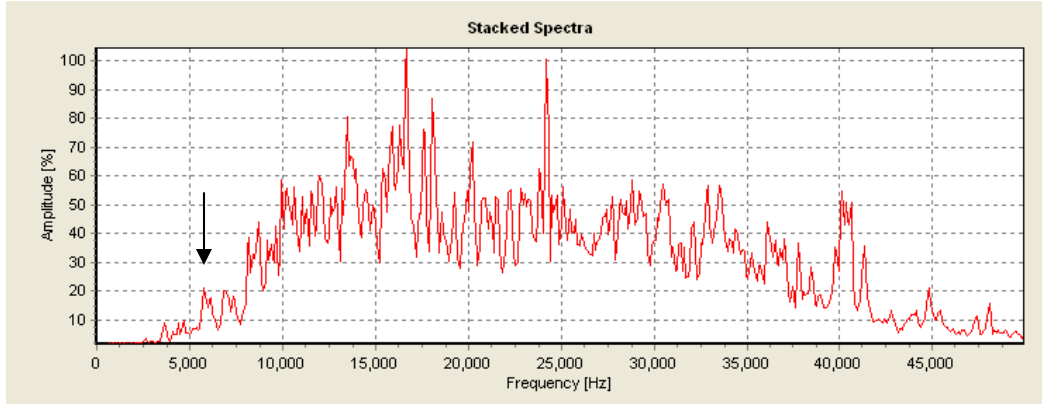


**b)**
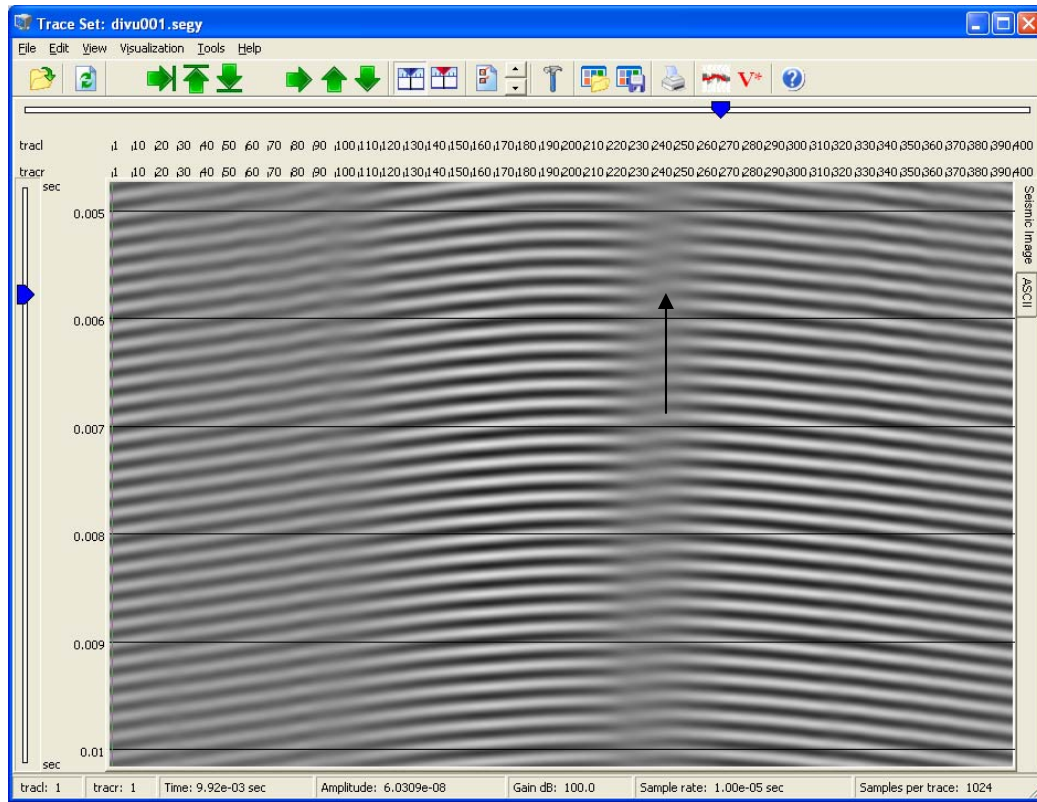


**Figure 10: a)** Amplitude spectrum of resonance waves for the proud shell presented in Figure 9. **b)** Narrow bandpass filtered resonance waves with central frequency of 5,750 Hz. The energy at this frequency represents less than 0.2 % of the total energy of the resonance wave (see arrow in Figure 10a). Amplitude variations due to interference of the resonance waves are manifested by shading and cycle skipping (see arrow in Figure 10b).
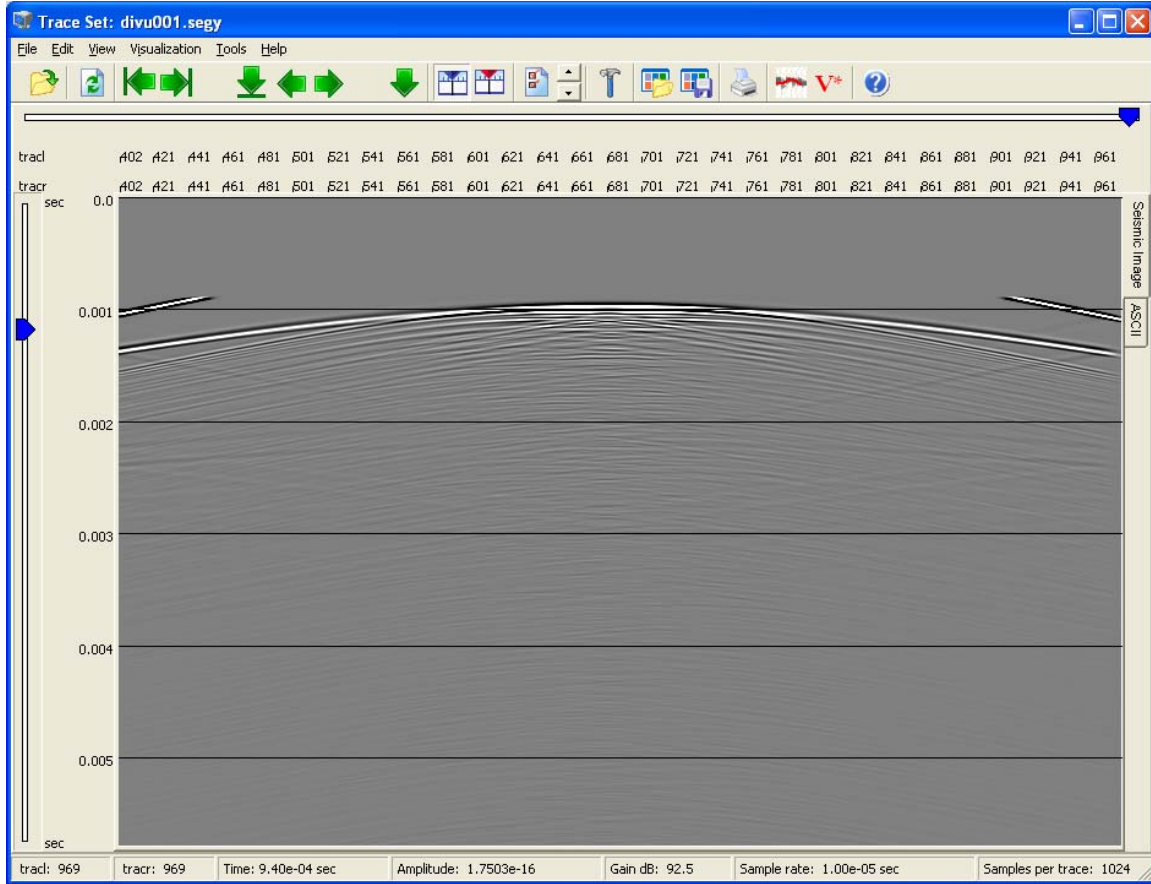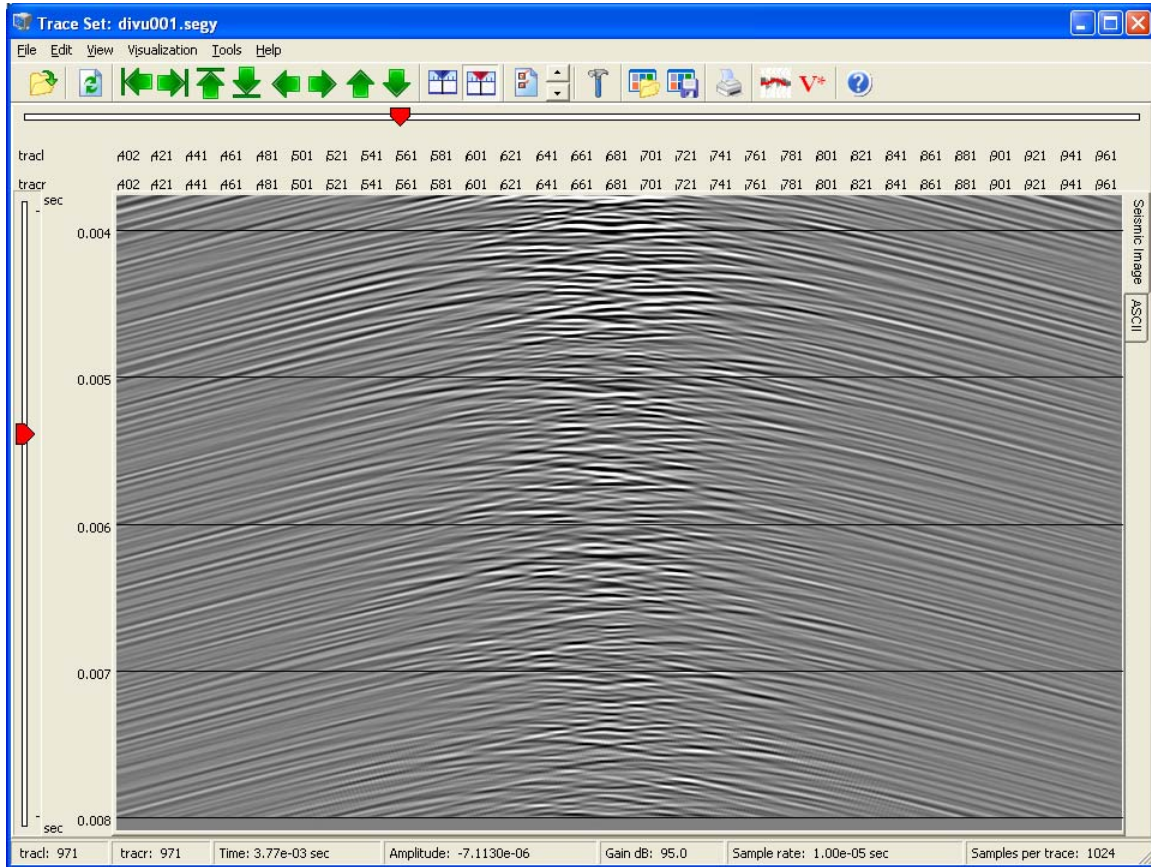
**Figure 11:** Time section of waveforms recorded for the proud shell with the receiver profile in y-direction (refer to Figure 4). Because of the longer extent of this receiver line it was not possible to completely suppress the direct waves without simultaneously suppressing the direct reflected waves. Therefore, remnant amplitudes of the direct waves can be seen on either end of the receiver line. Again, the continuous hyperbolic waves arriving after 0.001 s are the waves directly reflected off the shell, while the faint later arrivals represent resonance waves.
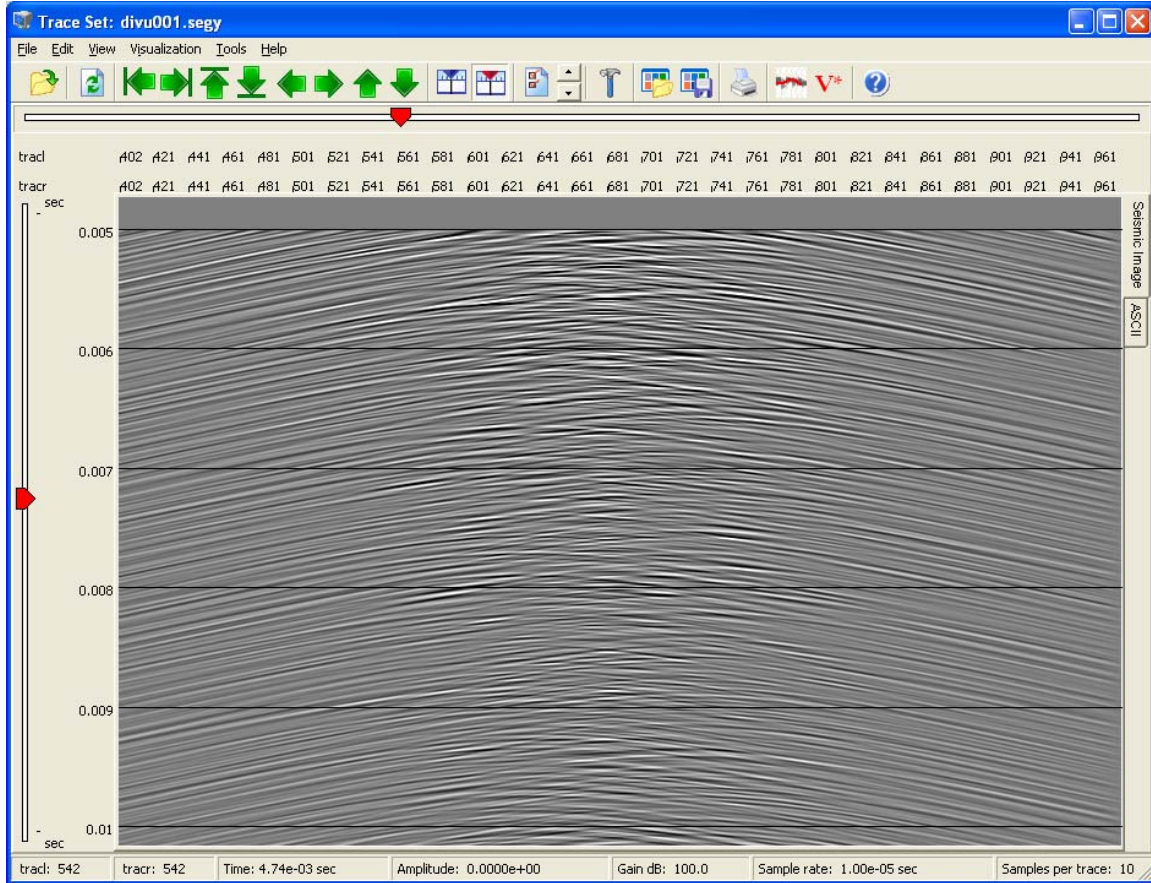
**Figure 12:** Time section of waveforms recorded for the proud shell with the receiver profile in y-direction (refer to Figure 4). The wavefield is muted before 0.005 s to suppress the amplitudes of the waves directly scattered off the shell. The hyperbolic wavefronts visible throughout the time section are resonance waves scattered off the shell.
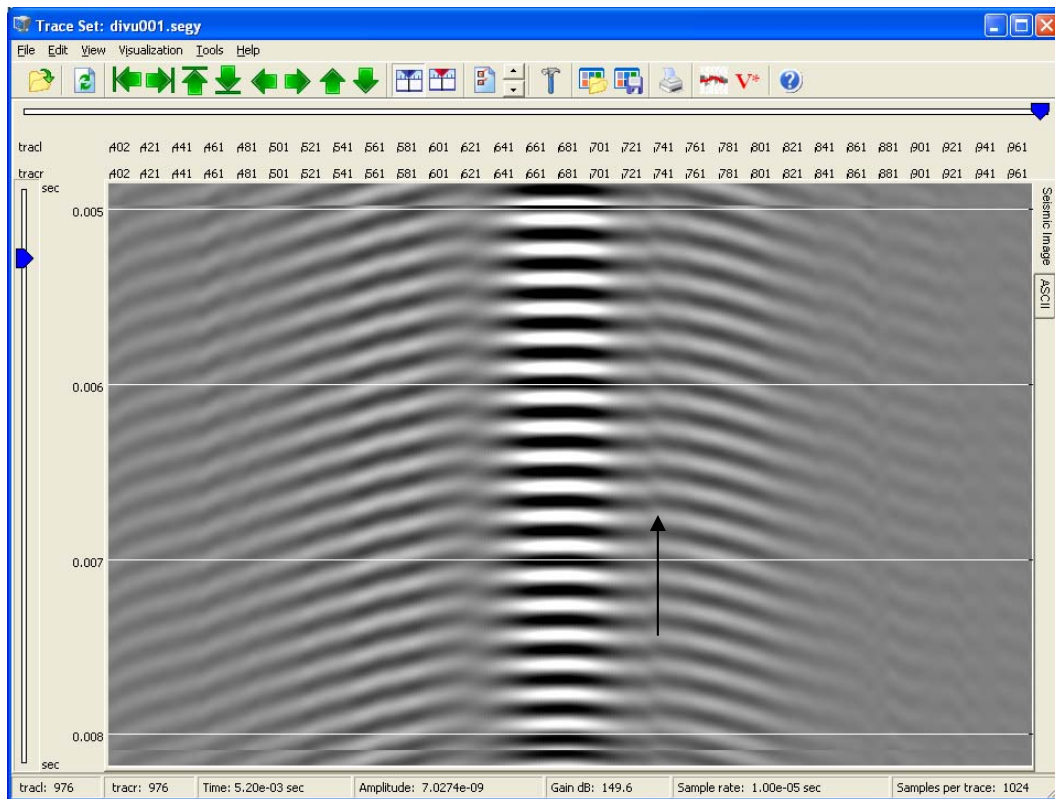
**a)**
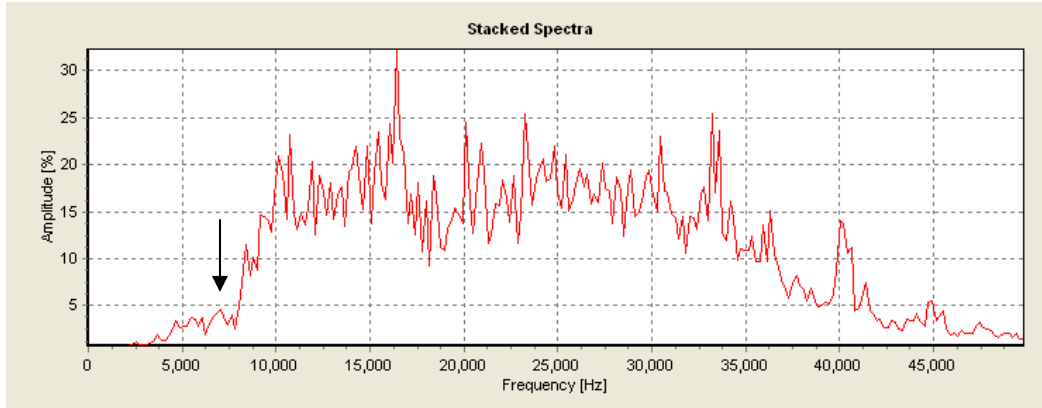


**b)**
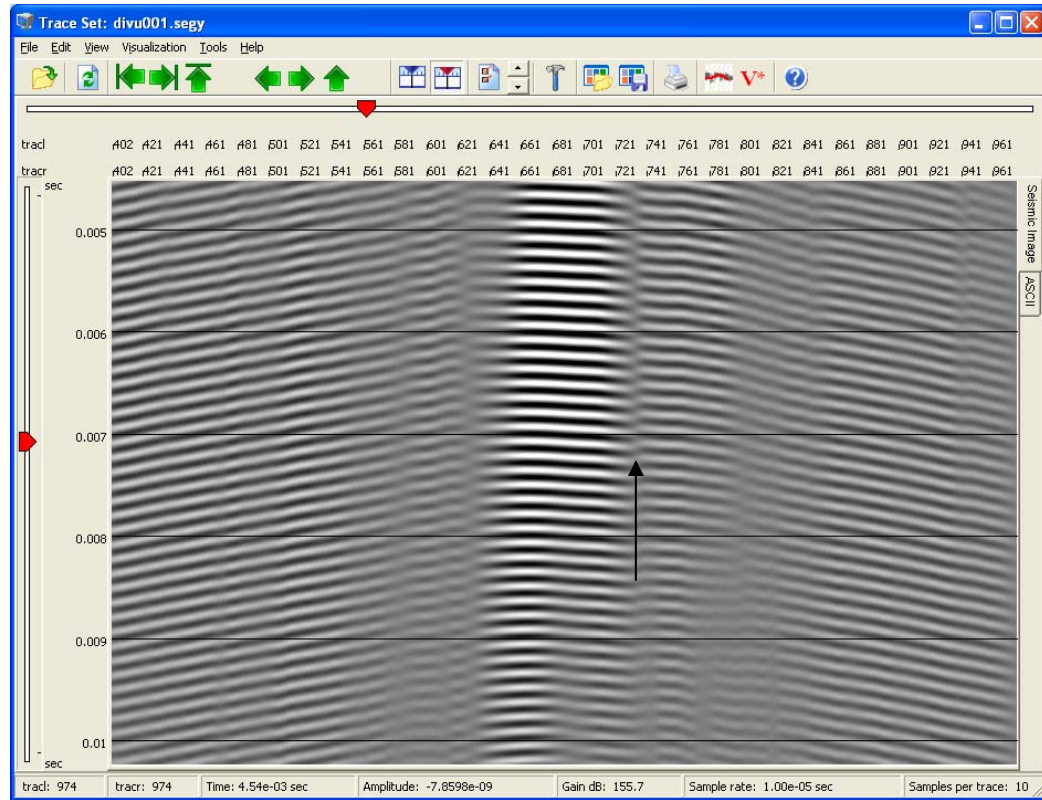


**Figure 13: a)** Amplitude spectrum of resonance waves for the proud shell presented in Figure 12. **b)** Narrow bandpass filtered resonance waves with central frequency of 7,000 Hz. The energy at this frequency represents less than 0.2 % of the total spectral energy of the resonance wave (see arrow in Figure 13a). Amplitude variations due to interference of the resonance waves are manifested by shading and cycle skipping (see arrow in Figure 13b).

**Figure 14:** Time section of waveforms recorded for the proud mortar with the receiver profile in x-direction (refer to Figure 4). The wavefield is muted before 0.0009 s to suppress the large amplitudes of the direct waves. The large hyperbolic wave arriving at 0.001 s are the waves directly reflected off the shell, while the faint later arrivals represent resonance waves.

**Figure 15:** Time section of waveforms recorded for the proud mortar with the receiver profile in x-direction (refer to Figure 4). The wavefield is muted before 0.0035 s to suppress the amplitudes of the waves directly scattered off the shell. The hyperbolic wavefronts visible throughout the time section are resonance waves scattered off the shell.

**a)**



**b)**



**Figure 16: a)** Amplitude spectrum of resonance waves for the proud mortar presented in Figure 15. **b)** Narrow bandpass filtered resonance waves with central frequency of 4,300 Hz. The energy at this frequency represents less than 0.1 % of the maximum spectral energy of the resonance wave (see arrow in Figure 16a). Amplitude variations due to interference of the resonance waves are manifested by shading and cycle skipping (see arrow in Figure 16b).

**Figure 17:** Time section of waveforms recorded for the proud mortar with the receiver profile in y-direction (refer to Figure 4). Because of the longer extent of this receiver line it was not possible to completely suppress the direct waves without simultaneously suppressing the direct reflected waves. Therefore, remnant amplitudes of the direct waves can be seen on either end of the receiver line. Again, the continuous hyperbolic waves arriving at about 0.001 s are the waves directly reflected off the shell, while the faint later arrivals represent resonance waves.

**Figure 18:** Time section of waveforms recorded for the proud mortar with the receiver profile in y-direction (refer to Figure 4). The wavefield is muted before 0.0035 s to suppress the amplitudes of the waves directly scattered off the shell. The hyperbolic wavefronts visible throughout the time section are resonance waves scattered off the shell.

**a)**
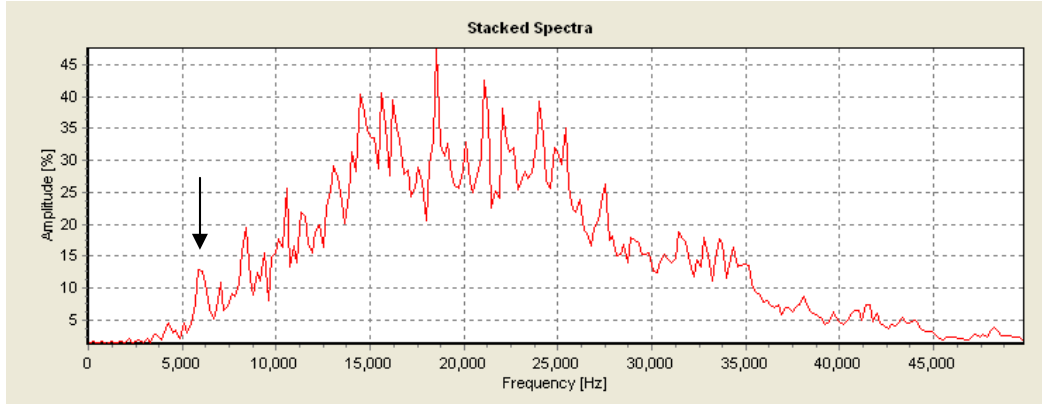


**b)**



**Figure 19: a)** Amplitude spectrum of resonance waves for the proud mortar presented in Figure 18. **b)** Narrow bandpass filtered resonance waves with central frequency of 5,850 Hz. The energy at this frequency represents about 0.4 % of the maximum spectral energy of the resonance wave (see arrow in Figure 19a). Amplitude variations due to interference of the resonance waves are manifested by shading and cycle skipping (see arrow in Figure 19b).
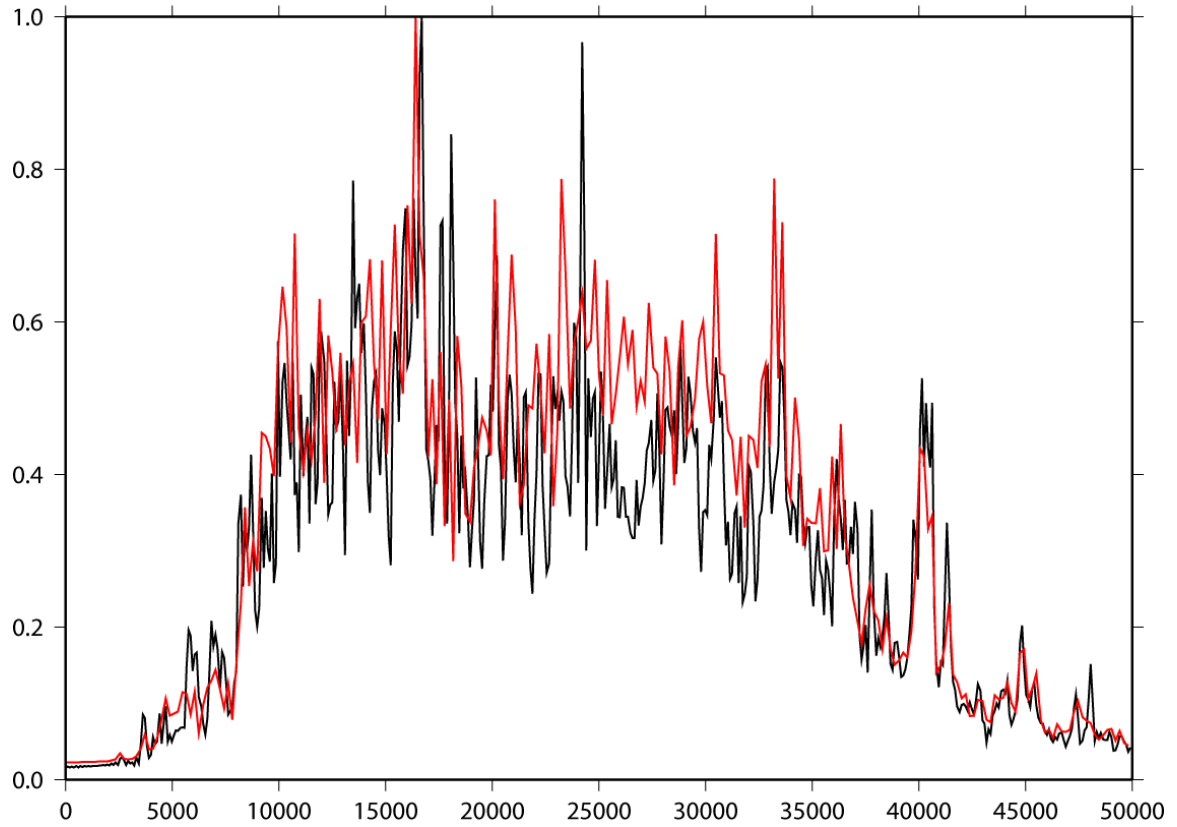
**Figure 20:** Superposition of normalized resonance wave amplitude spectra for the proud shell for the x-profile (black, refer to Figure 10a) and y-profile (red, refer to Figure 13a).
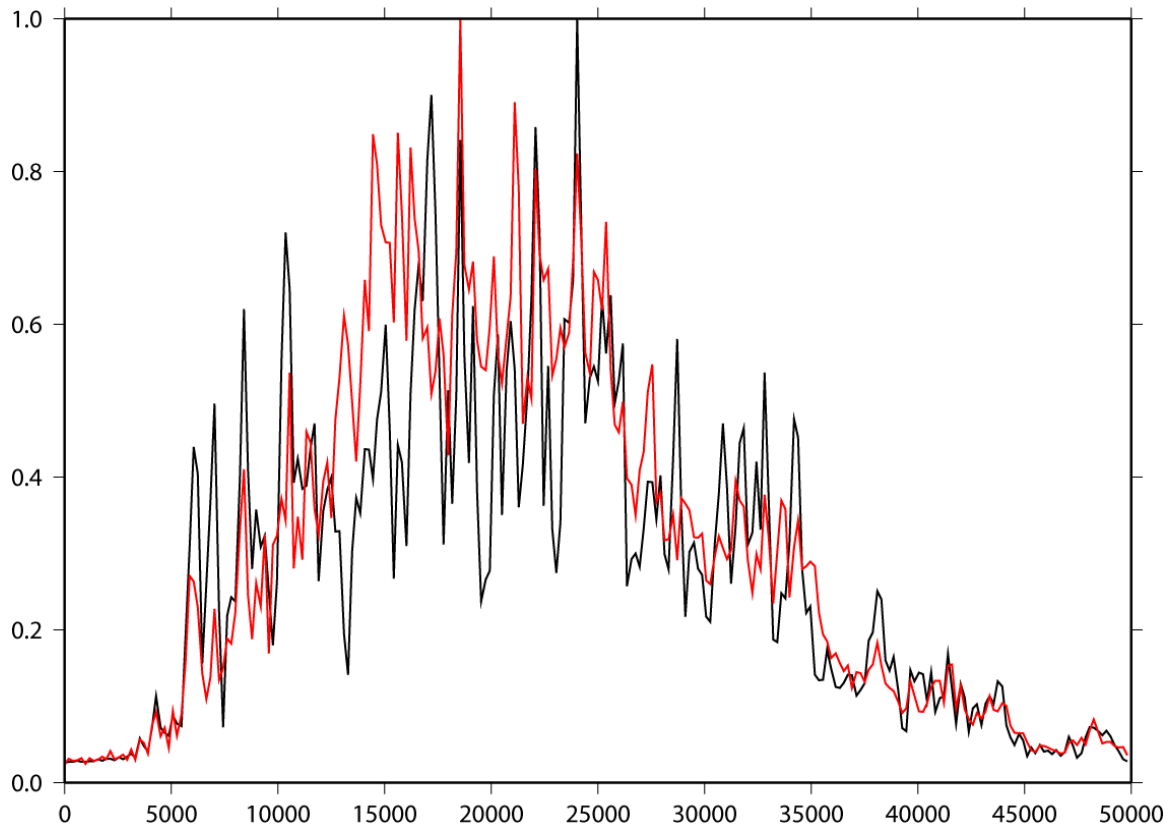
**Figure 21:** Superposition of the normalized resonance wave amplitude spectra for the proud mortar for the x-profile (black, refer to Figure 16a) and y-profile (red, refer to Figure 19a).
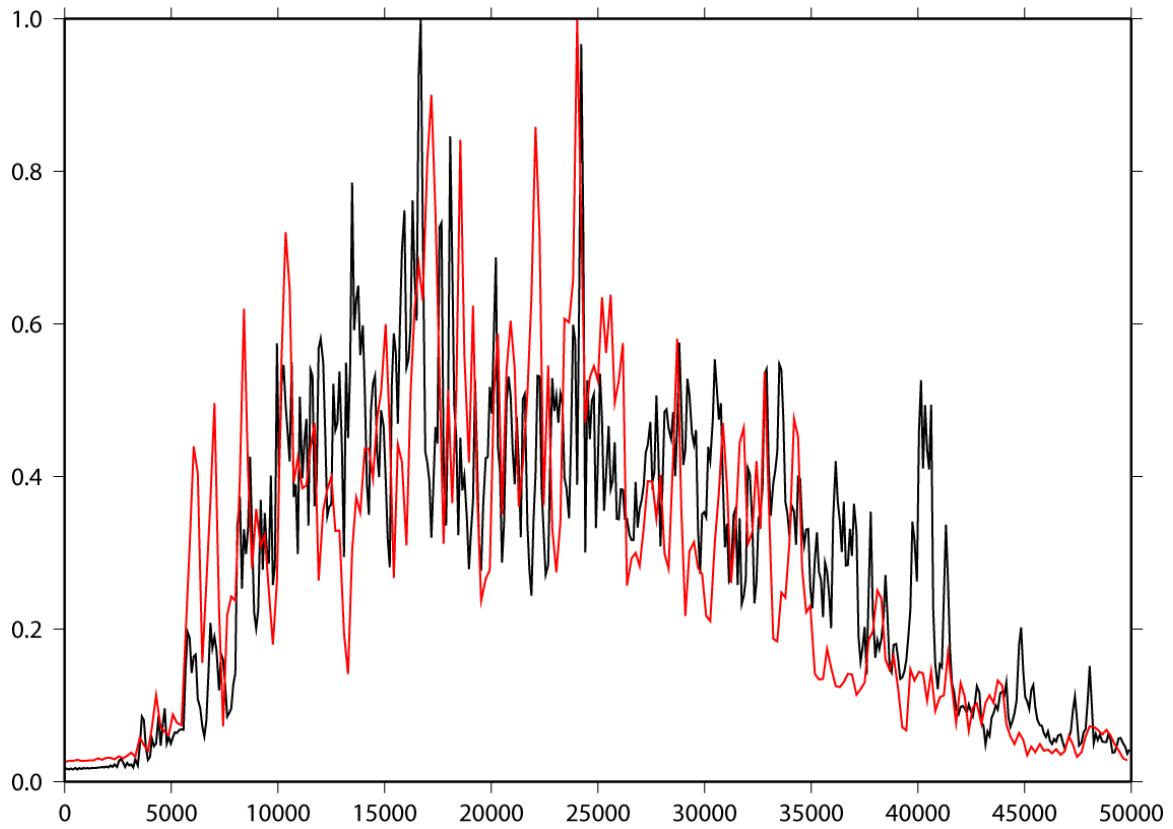
**Figure 22:** Superposition of the normalized resonance wave amplitude spectra for the x-profiles of the proud shell (black) and of the proud mortar (red).
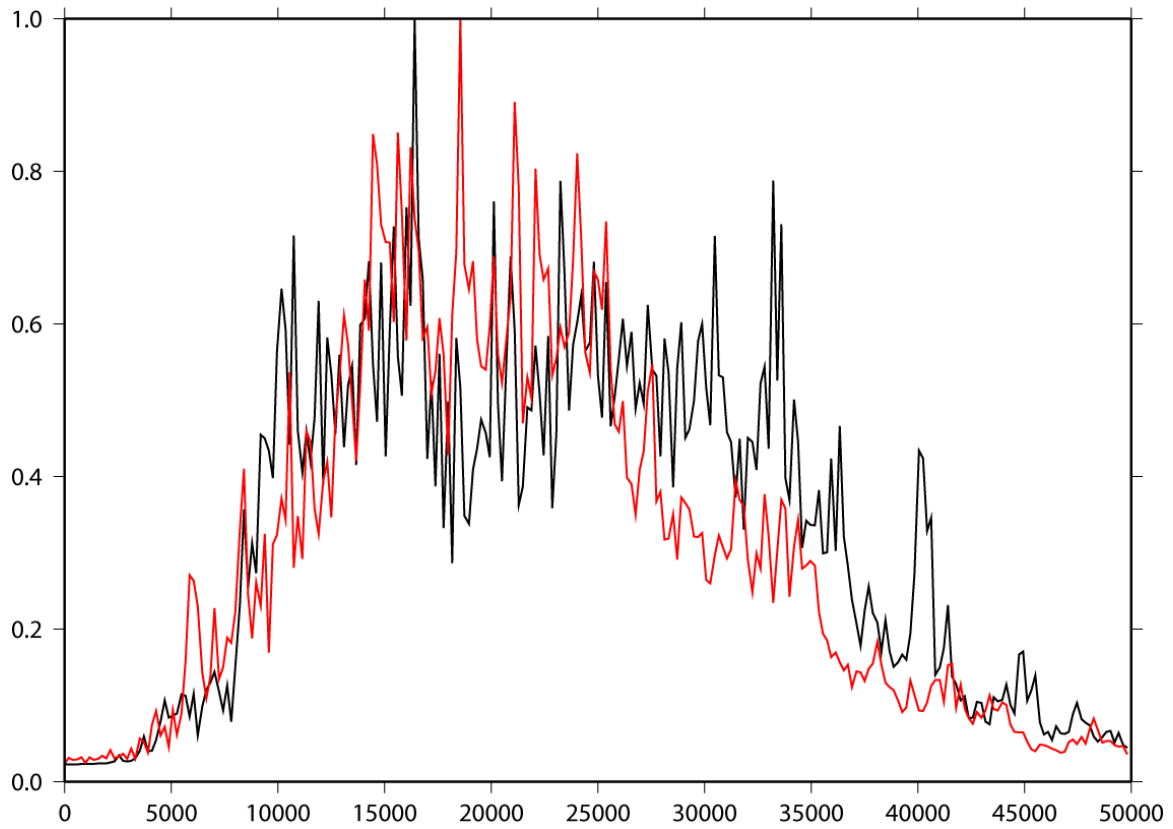
**Figure 23:** Superposition of the normalized resonance wave amplitude spectra for the y-profiles of the proud shell (black) and of the proud mortar (red).

**a)**

Target Field

Target

10 m

Range (x) Distance [m]

Cross Range (y) Distance along Rail [m]

**b)**

Viewing Direction from Rail to Target Field

Elevation (z) above Bottom [m]

Chan-07

Chan-08

Sources
Chan-09

Chan-10

Chan-11

Chan-12

Distance (y) along Rail [m]
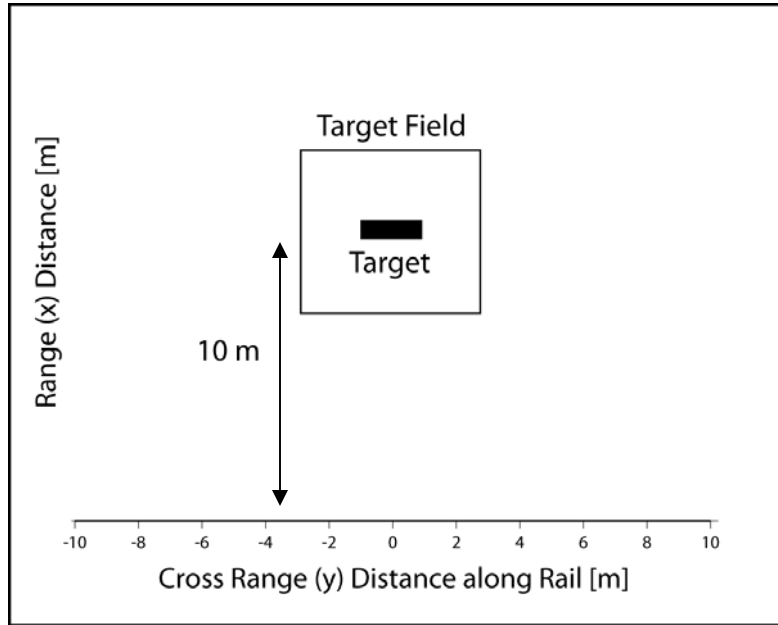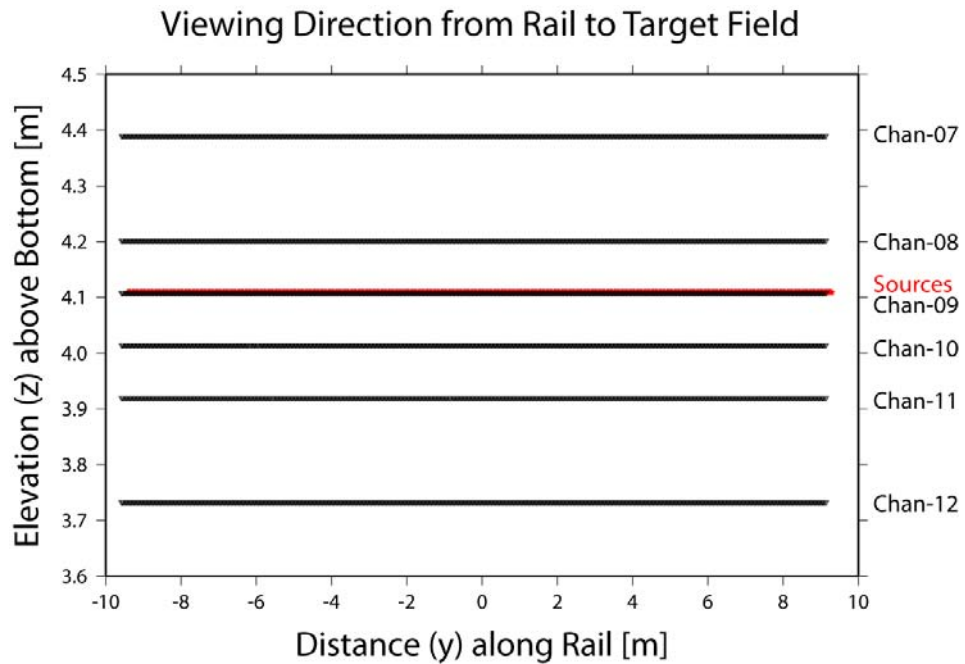
**Figure 24:** Geometry of the data acquisition experiment at the pond facility of NSWC-PC in 2007. **a)** Plan view of the rail and target field. **b)** Vertical view of the recording geometry with 750 horizontal source and receiver positions spaced by 0.0025 m. The separate symbols for source (red) and receiver (black) locations are not resolved due to the short spacing along the rail.
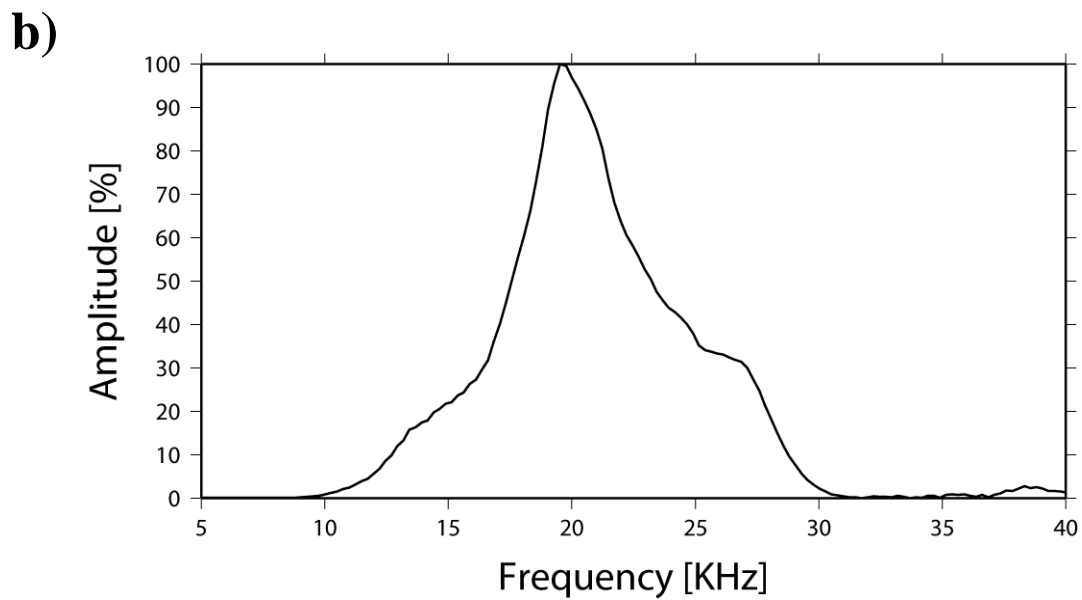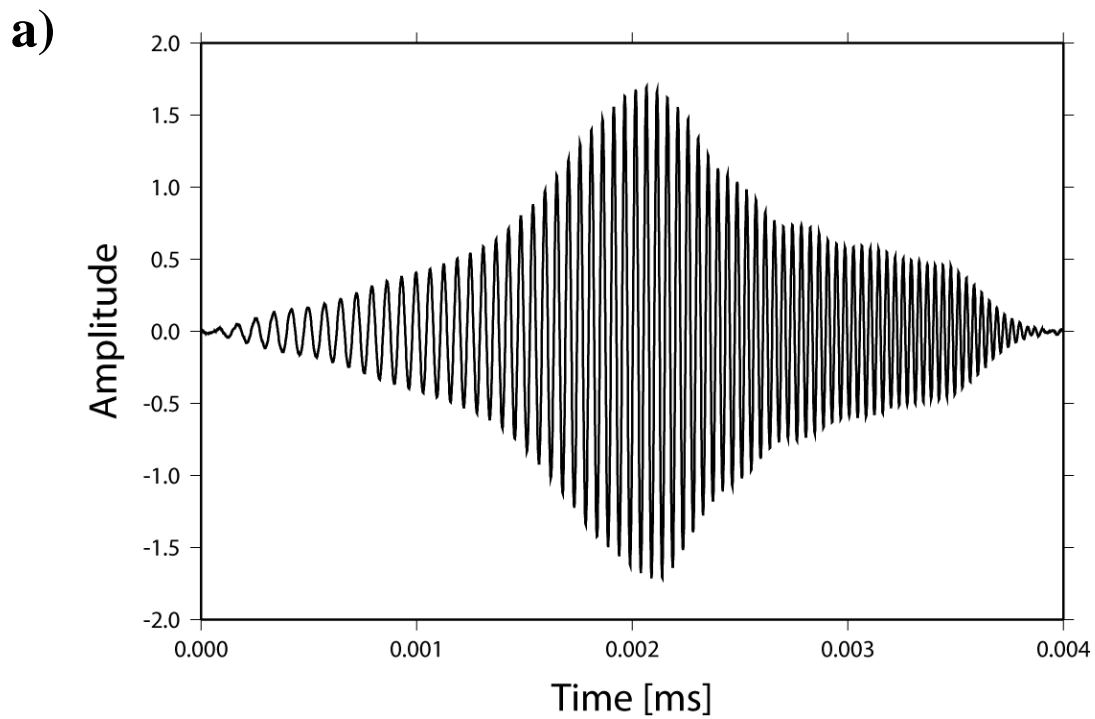
**Figure 24: a)** Analytical representation of the source sweep with 0.004 s duration used as source input. **b)** Amplitude spectrum of source sweep in a).
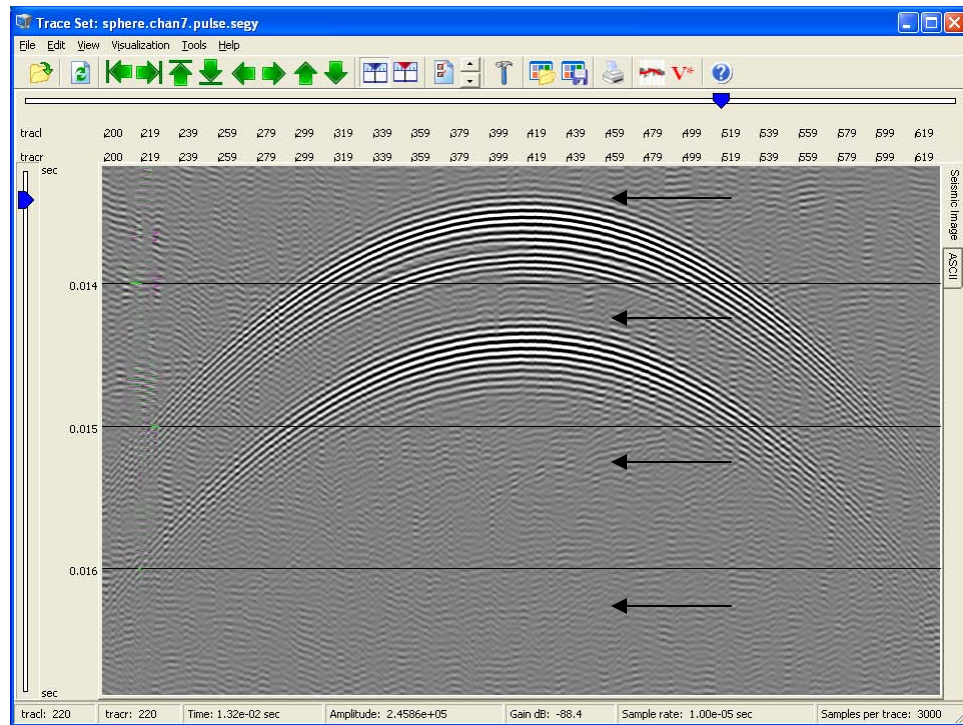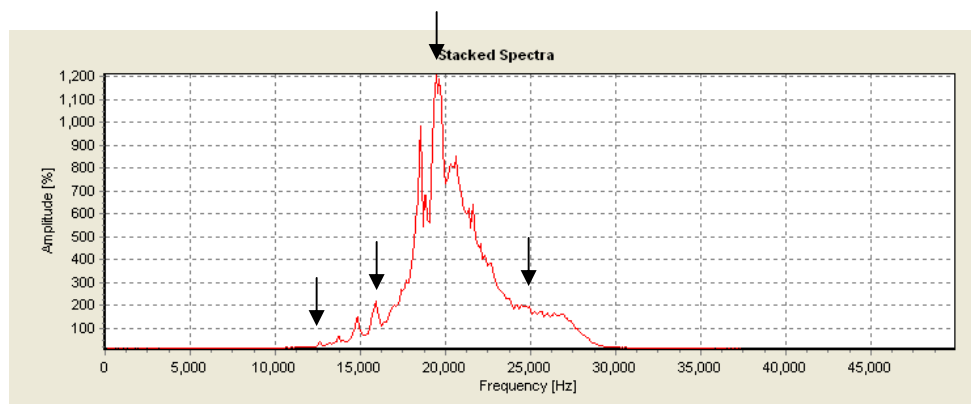
**Figure 25: a)** Time section of the waveforms recorded for the proud sphere. The arrows identify direct and resonance scattered waves. **b)** Amplitude spectrum of the data displayed in a). The arrows identify spectral resonance frequencies used for narrow bandpass filtering and imaging of the sphere.

**a)**
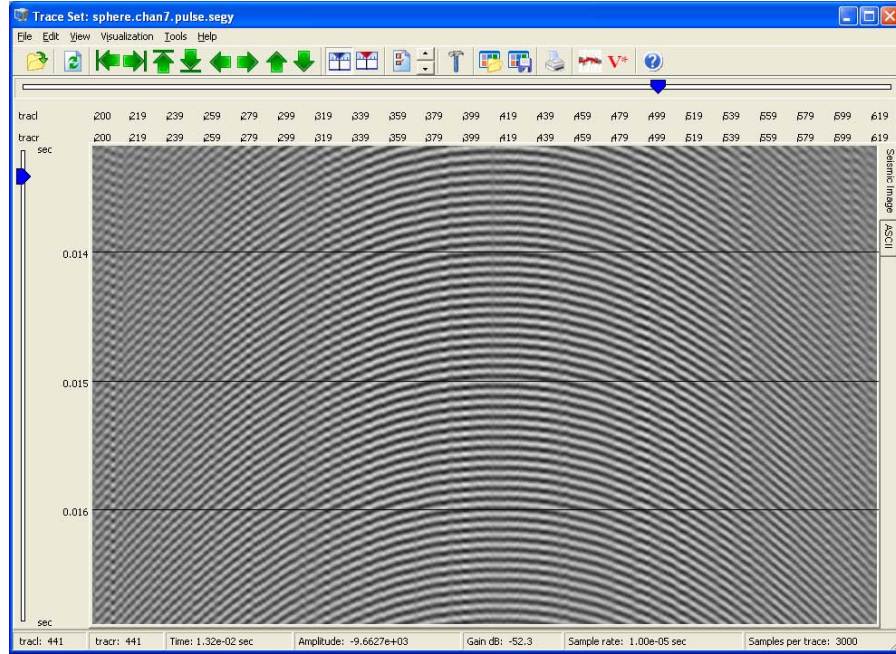


**b)**
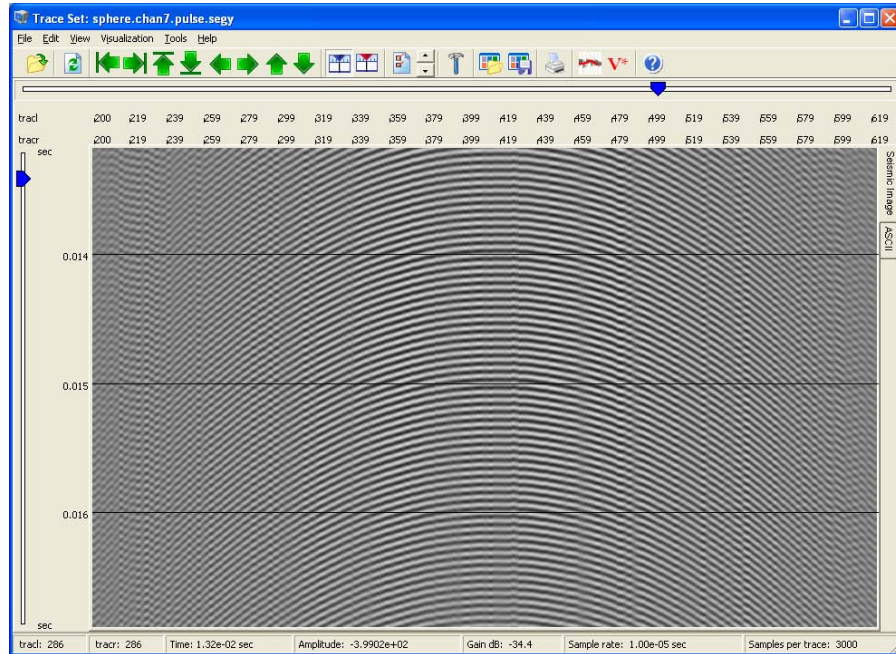


**Figure 26: a)** Narrow bandpass filtered resonance waves for the proud sphere with central frequency of 12,600 Hz. The energy at this frequency represents only 0.09 % of the maximum spectral energy of the resonance wave (see arrow in Figure 25b). **b)** Narrow bandpass filtered resonance waves for the proud sphere with central frequency of 16,000 Hz. The energy at this frequency represents about 0.9 % of the maximum spectral energy of the resonance wave (see arrow in Figure 25b).

**c)**
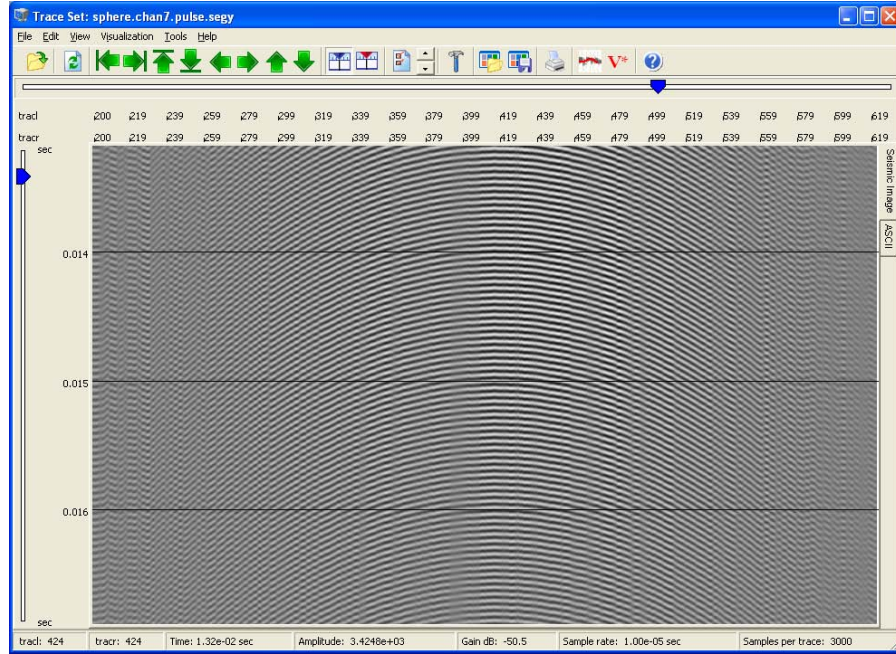


**d)**
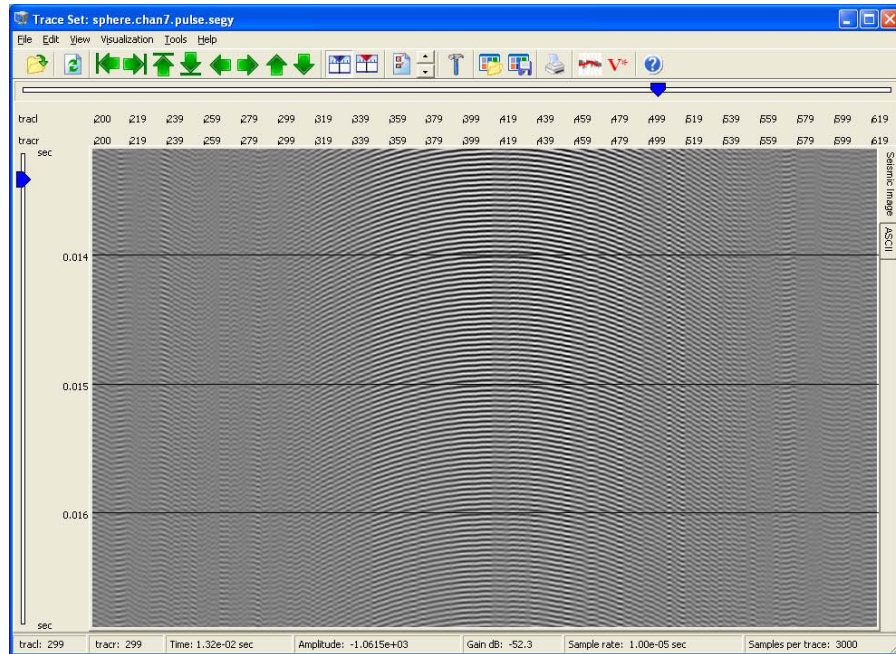


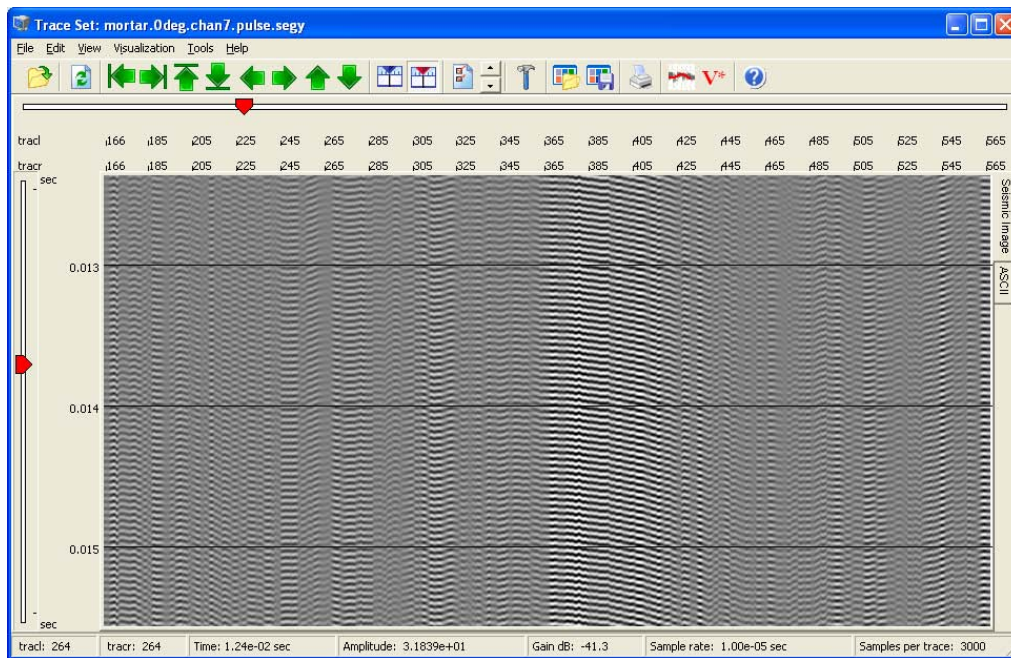**Figure 26 (cont.): c)** Narrow bandpass filtered resonance waves for the proud sphere with central frequency of 19,330 Hz. The energy at this frequency represents 5.3 % of maximum spectral energy of the resonance wave (see arrow in Figure 25b). **d)** Narrow bandpass filtered resonance waves for the proud sphere with central frequency of 25,000 Hz. The energy at this frequency represents about 0.9 % of the maximum spectral energy of the resonance wave (see arrow in Figure 25b).
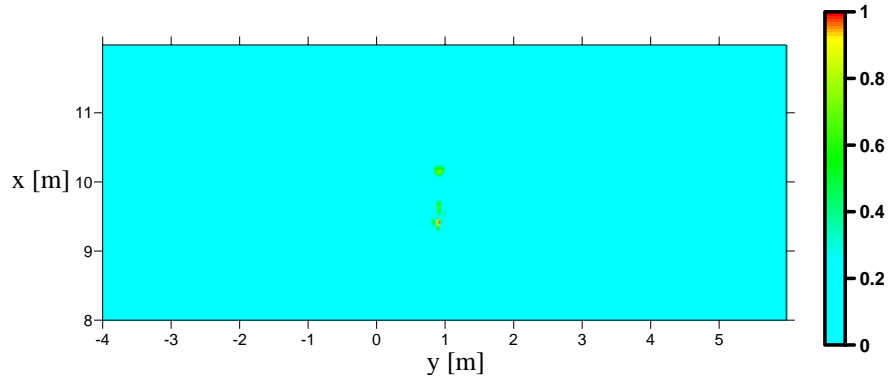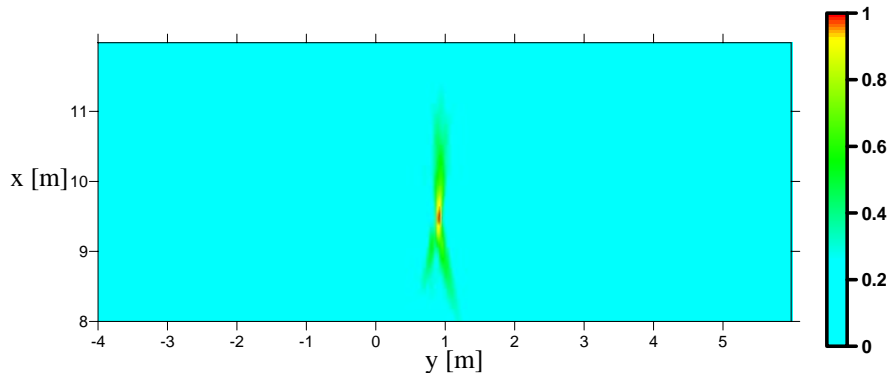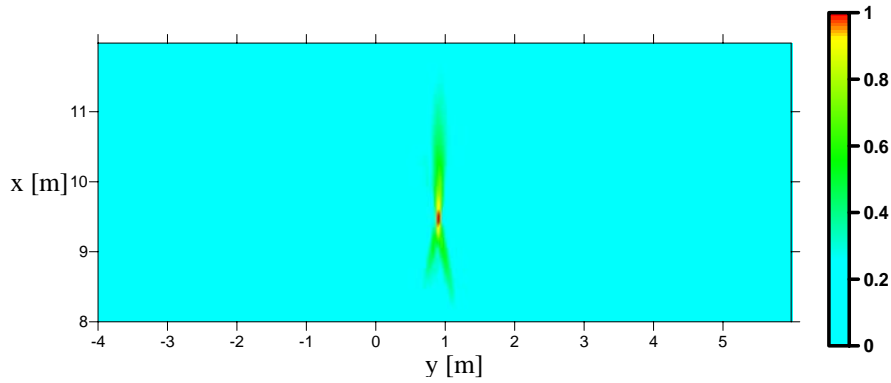
**Figure 27: a)** Two-dimensional plane view of the Kirchhoff migrated proud sphere using data shown in Figure 25a. **b)** Two-dimensional plane view of the resonance migrated proud sphere using 12,600 Hz data shown in Figure 26a. **c)** Two-dimensional plane view of the resonance migrated proud sphere using 16,000 Hz data shown in Figure 26b.
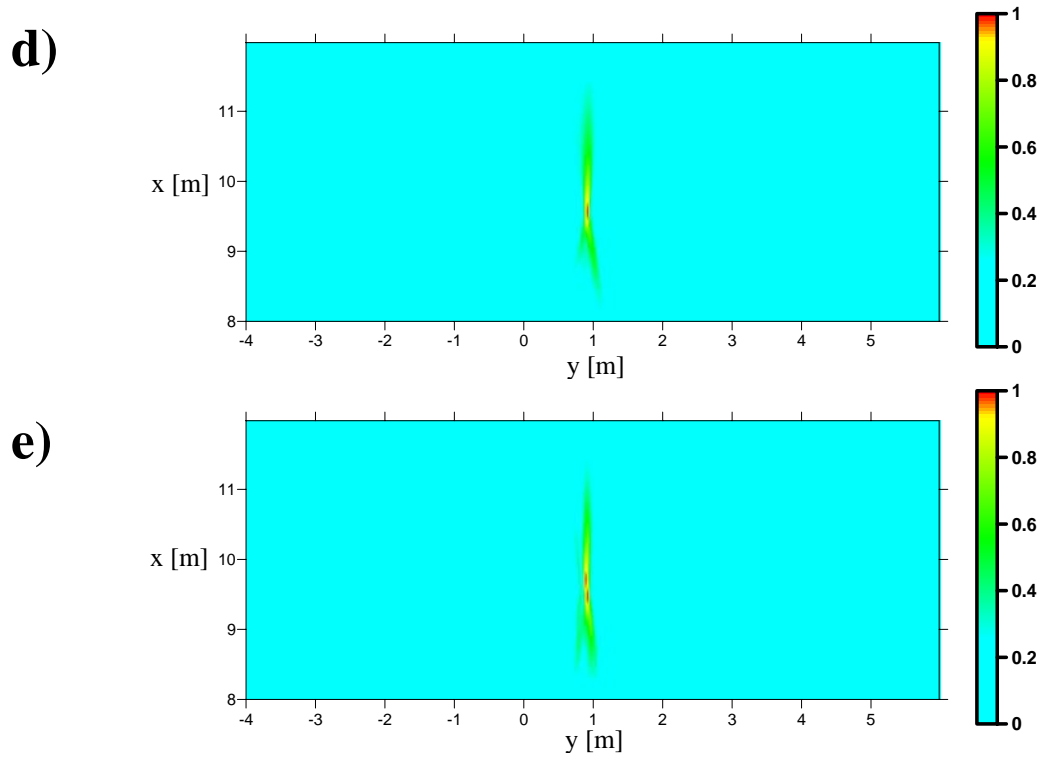
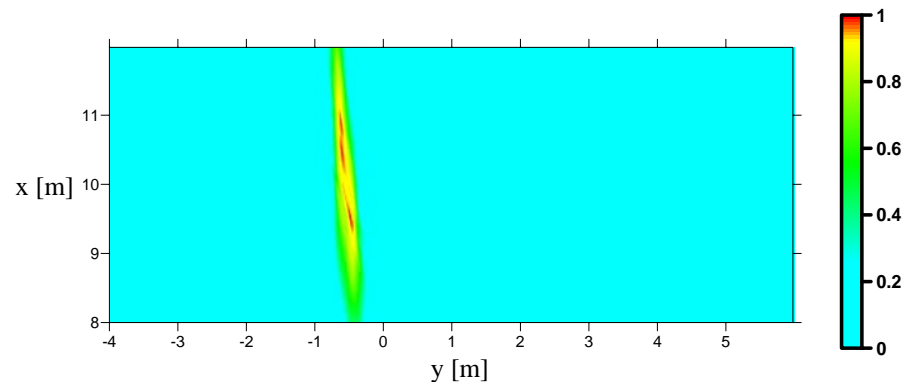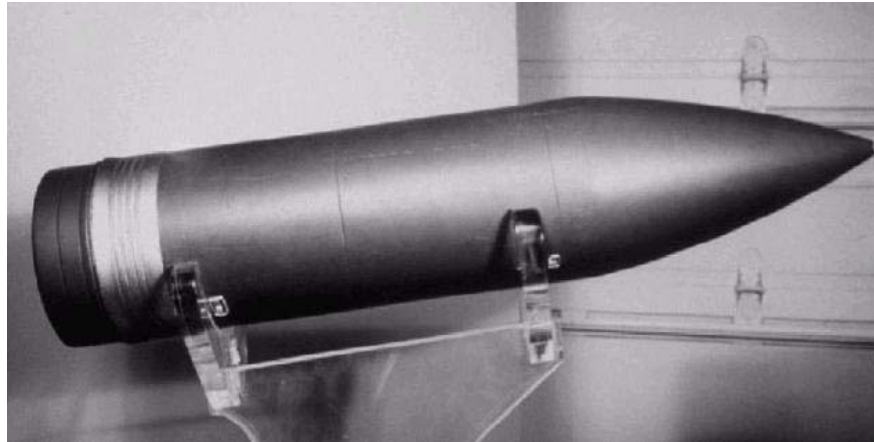**Figure 27 (cont.): d)** Two-dimensional plane view of the resonance migrated proud sphere using 19,330 Hz data shown in Figure 26c. **e)** Two-dimensional plane view of the resonance migrated proud sphere using 25,000 Hz data shown in Figure 26d.

**Figure 28:** Representative image of an 81-mm mortar from file (not the mortar used during the field experiment). Note the fins along the tail section. The processed mortar data was acquired from a mortar with its fins attached.

**a)**
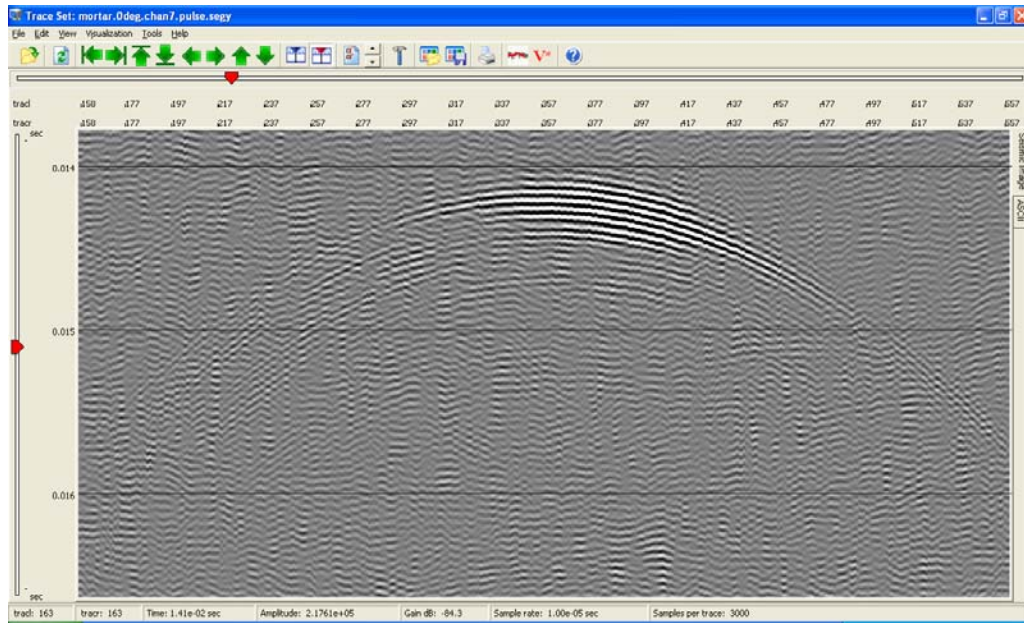


**b)**
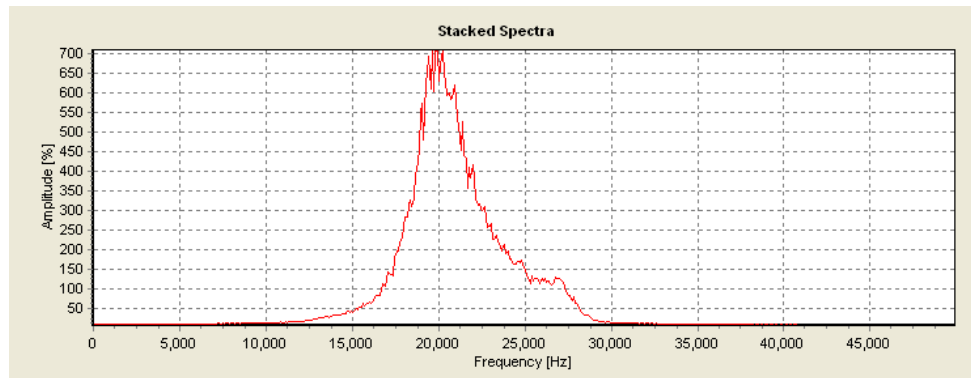


**Figure 29: a)** Time section of the waveforms recorded for the proud mortar. During data acquisition the tip of the mortar was oriented towards the rail. **b)** Amplitude spectrum of the data displayed in a).

**a)**
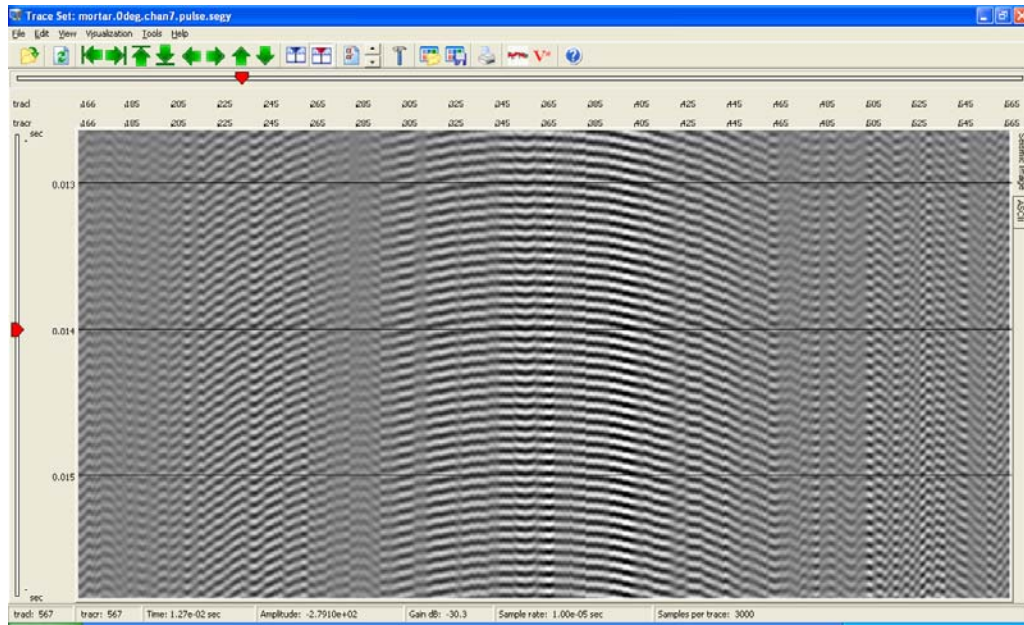


**b)**
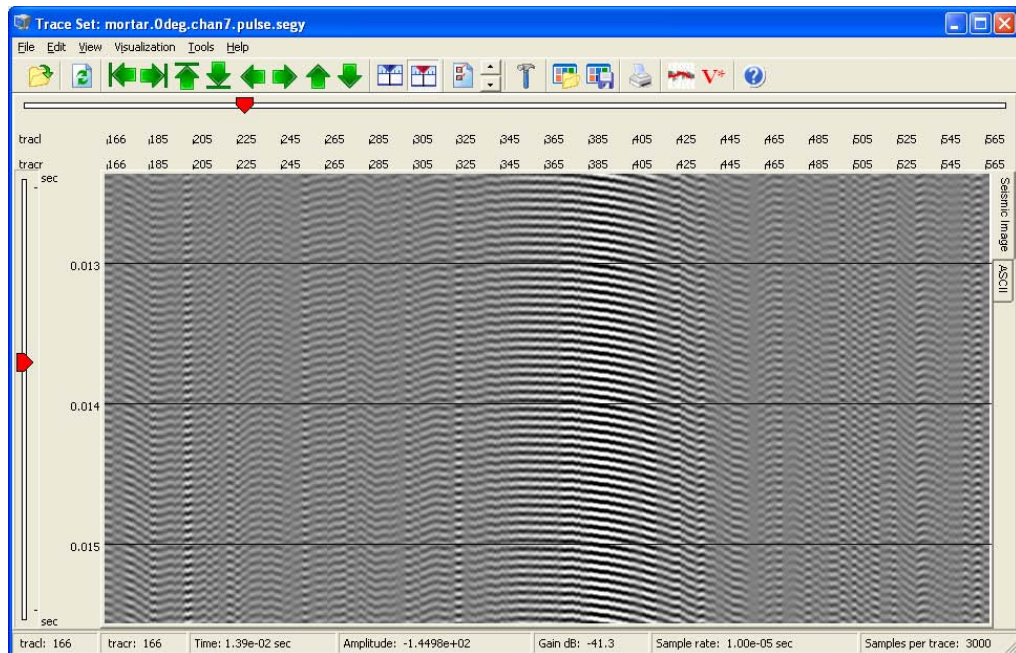


**Figure 30: a)** Narrow bandpass filtered resonance waves for the proud mortar with central frequency of 13,000 Hz. **b)** Narrow bandpass filtered resonance waves for the proud mortar with central frequency of 16,000 Hz.

**c)**



**Figure 30 (cont.): c)** Narrow bandpass filtered resonance waves for the proud mortar with central frequency of 20,800 Hz.
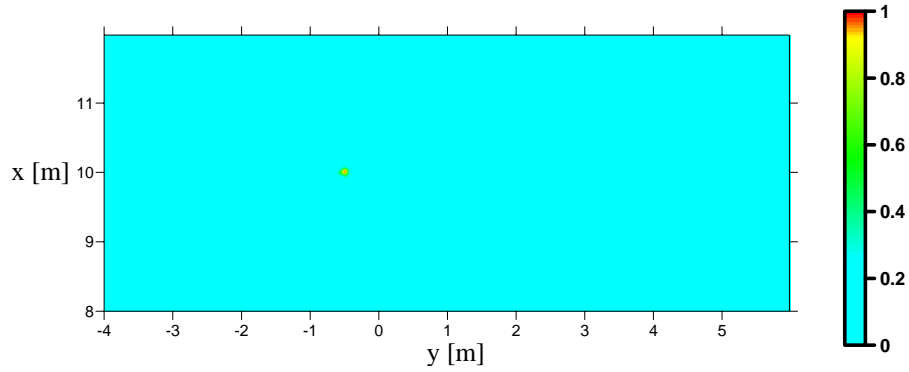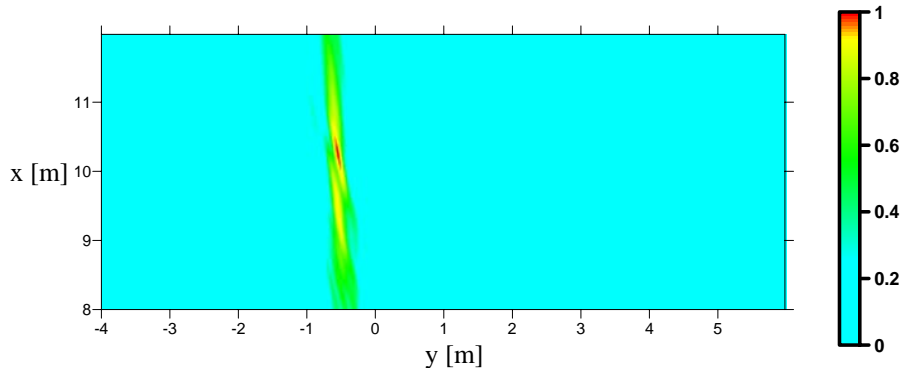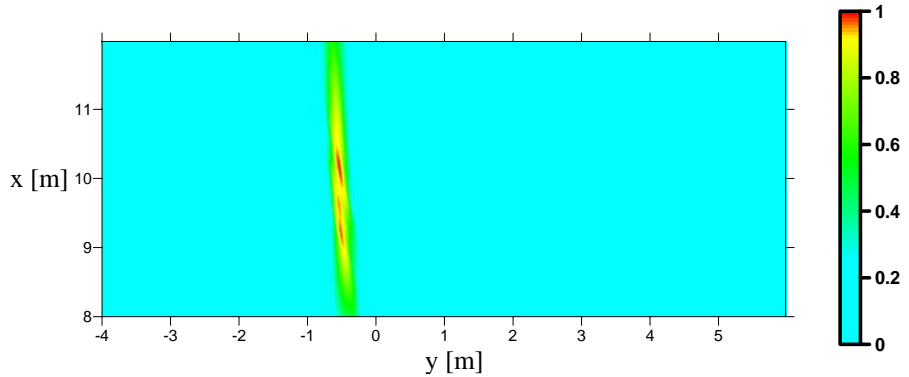
**Figure 31: a)** Two-dimensional plane view of the Kirchhoff migrated proud mortar using data shown in Figure 29a. During data acquisition the tip of the mortar was oriented towards the rail. **b)** Two-dimensional plane view of the resonance migrated proud mortar using 13,000 Hz data shown in Figure 30a. **c)** Two-dimensional plane view of the resonance migrated proud mortar using 16,000 Hz data shown in Figure 30b.

**d)**



**Figure 31 (cont.): d)** Two-dimensional plane view of the resonance migrated proud mortar using 20,800 Hz data shown in Figure 30c.

**Figure 32:** Representative image of a 4-inch artillery shell (not the shell used during the field experiment). Note the pointed tip and the round flat bottom.
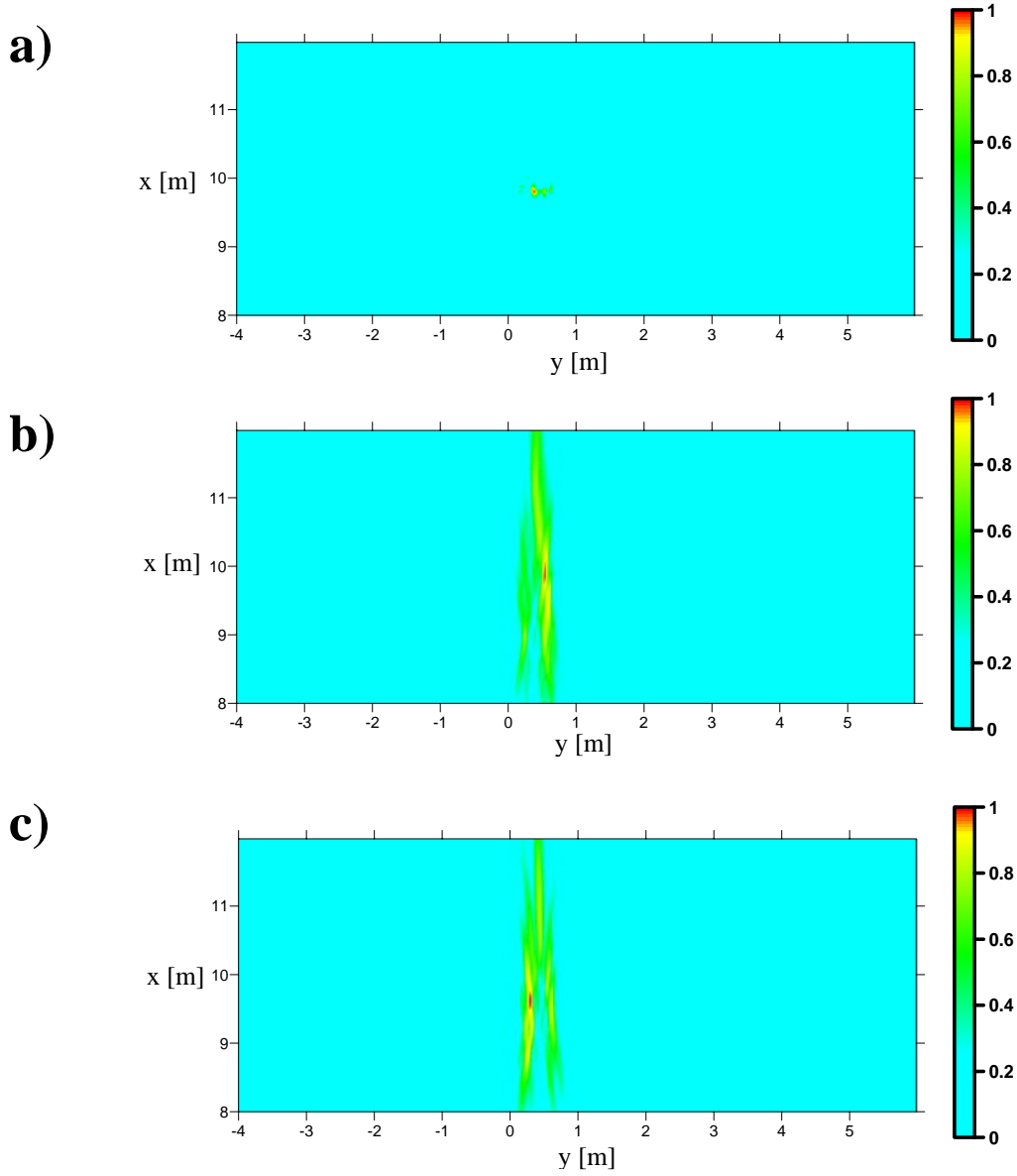
**Figure 33: a)** Two-dimensional plane view of the Kirchhoff migrated proud shell. During data acquisition the tip of the shell was oriented in negative y-direction. **b)** Two-dimensional plane view of the resonance migrated proud shell using 19,100 Hz data. **c)** Two-dimensional plane view of the resonance migrated proud shell using 20,200 Hz data.

**d)**
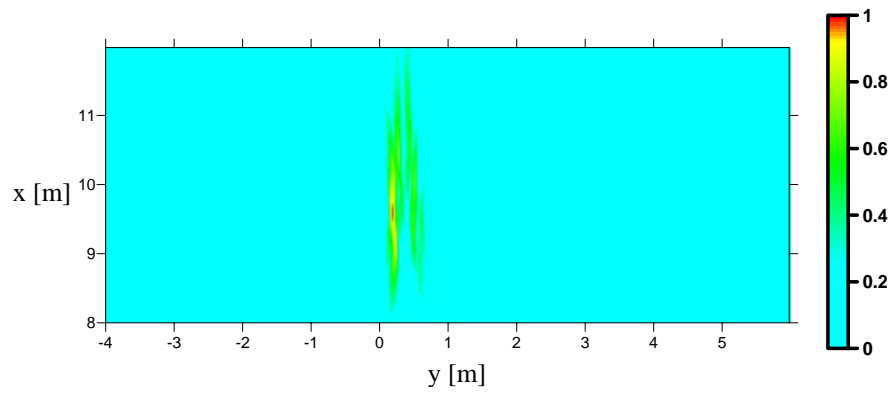


**Figure 33 (cont.): d)** Two-dimensional plane view of the resonance migrated proud shell using 26,900 Hz data.

**Figure 34:** Representative image of two 500 pound bombs (not the bomb used during the field experiment).
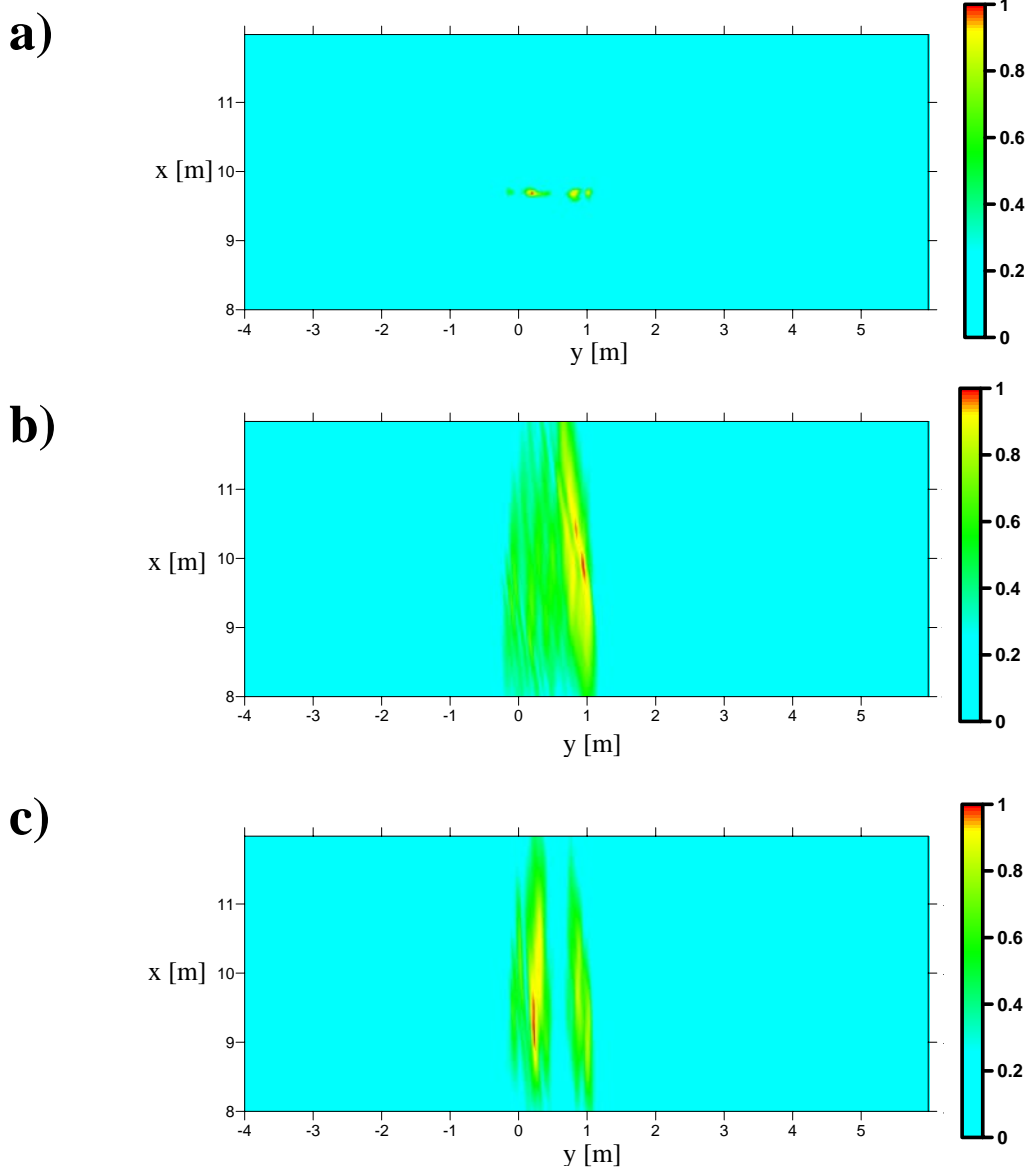
**Figure 35: a)** Two-dimensional plane view of the Kirchhoff migrated proud bomb oriented parallel to the rail. During data acquisition the tip of the bomb was oriented in negative y-direction. **b)** Two-dimensional plane view of the resonance migrated prou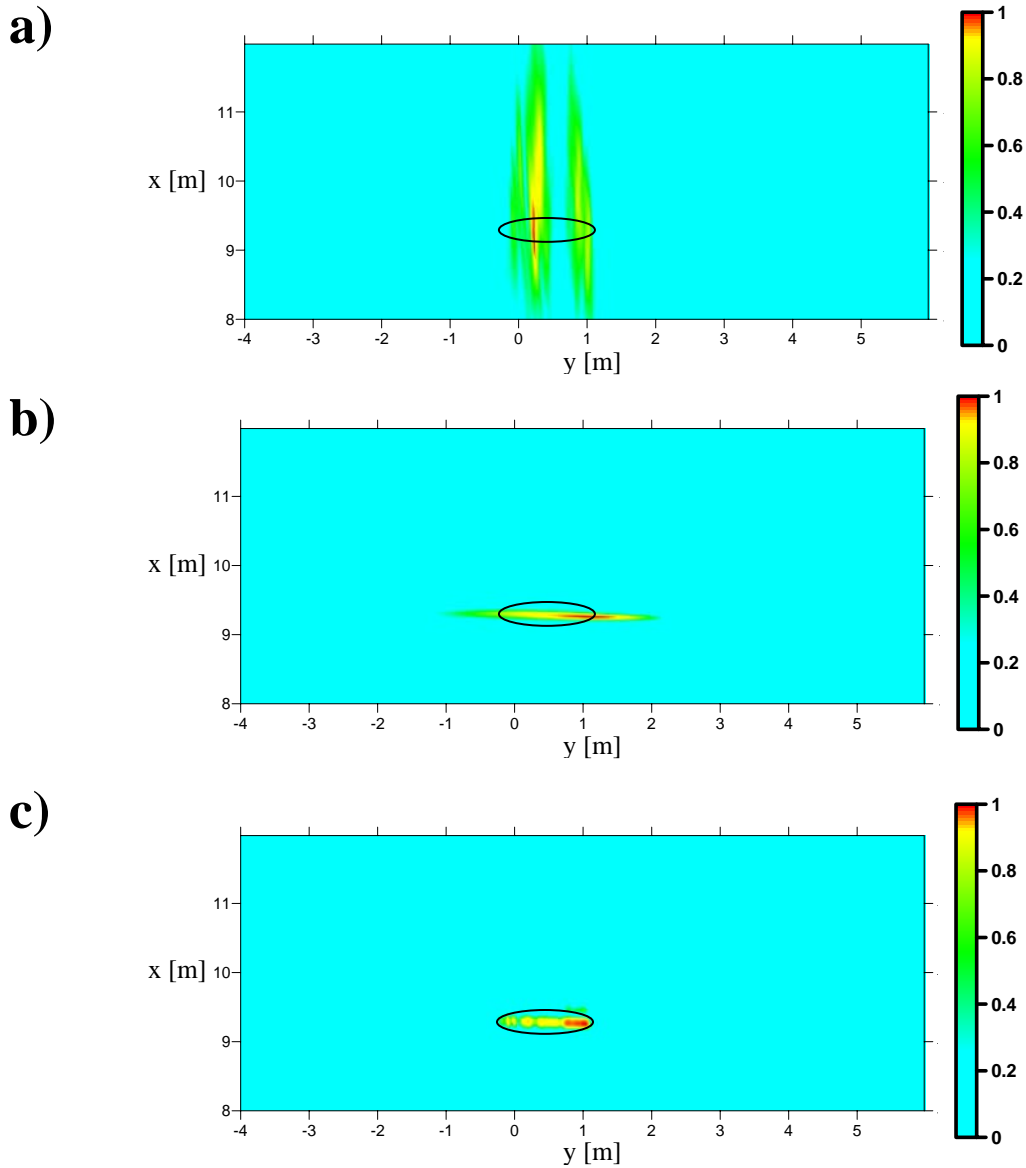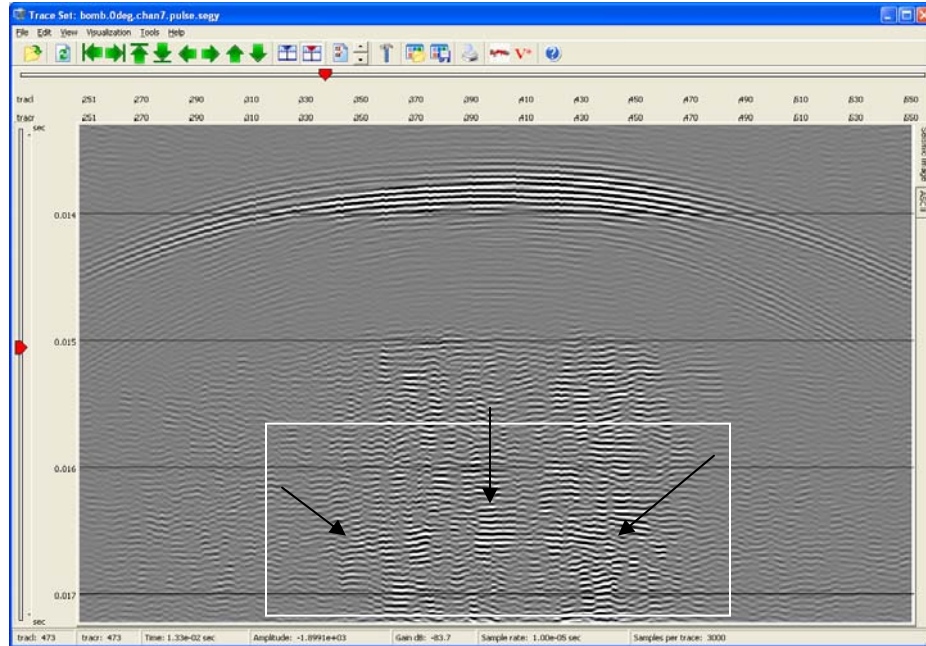d bomb oriented parallel to the rail using 20,120 Hz data. **c)** Two-dimensional plane view of the resonance migrated proud bomb oriented parallel to the rail using 25,960 Hz data.
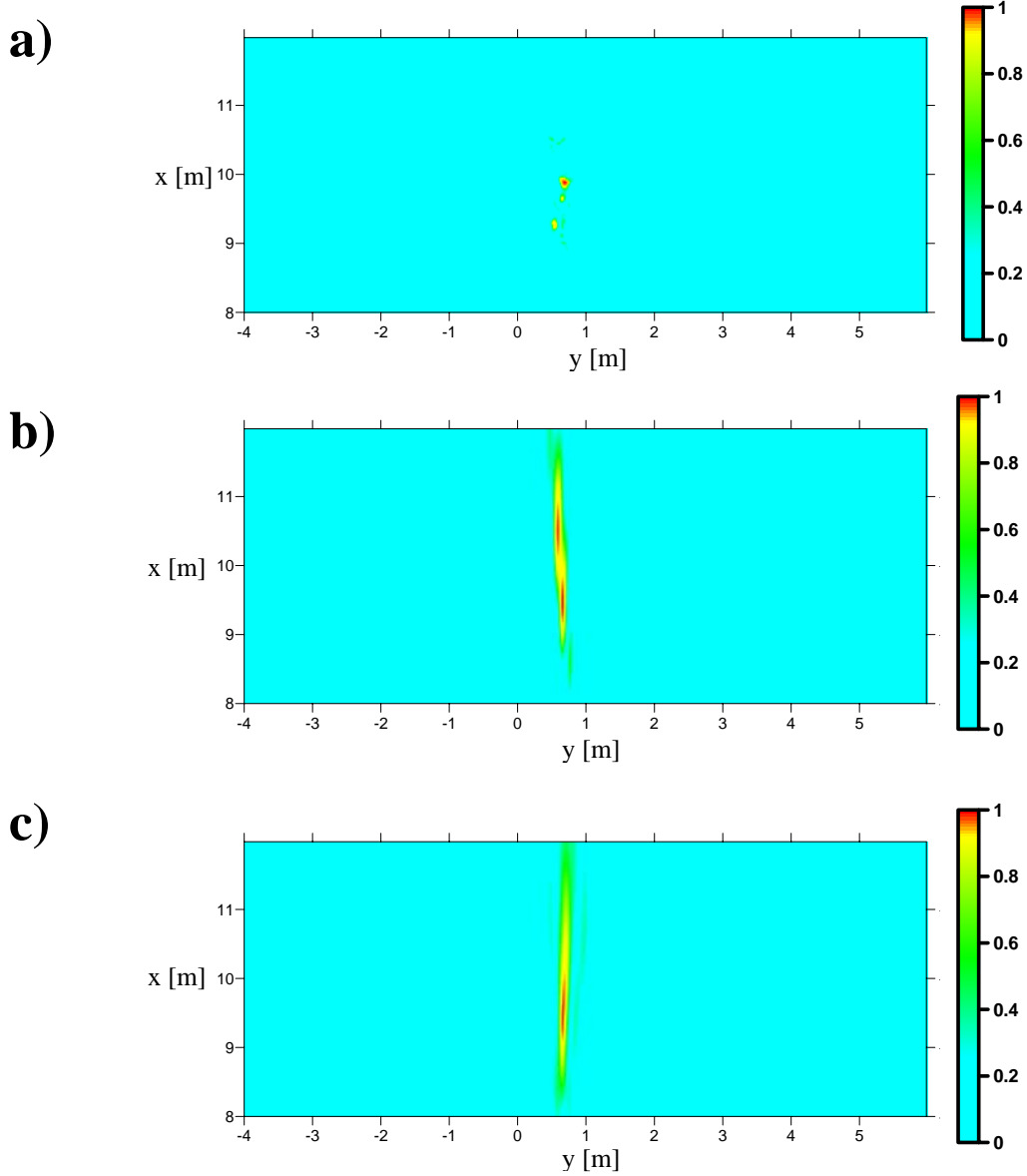
**Figure 36: a)** Two-dimensional plane view of the Kirchhoff migrated proud bomb oriented perpendicular to the rail. During data acquisition the tip of the bomb was oriented toward the rail. **b)** Two-dimensional plane view of the resonance migrated proud bomb oriented perpendicular to the rail using 18,700 Hz data. **c)** Two-dimensional plane view of the resonance migrated proud bomb oriented perpendicular to the rail using 19,340 Hz data.
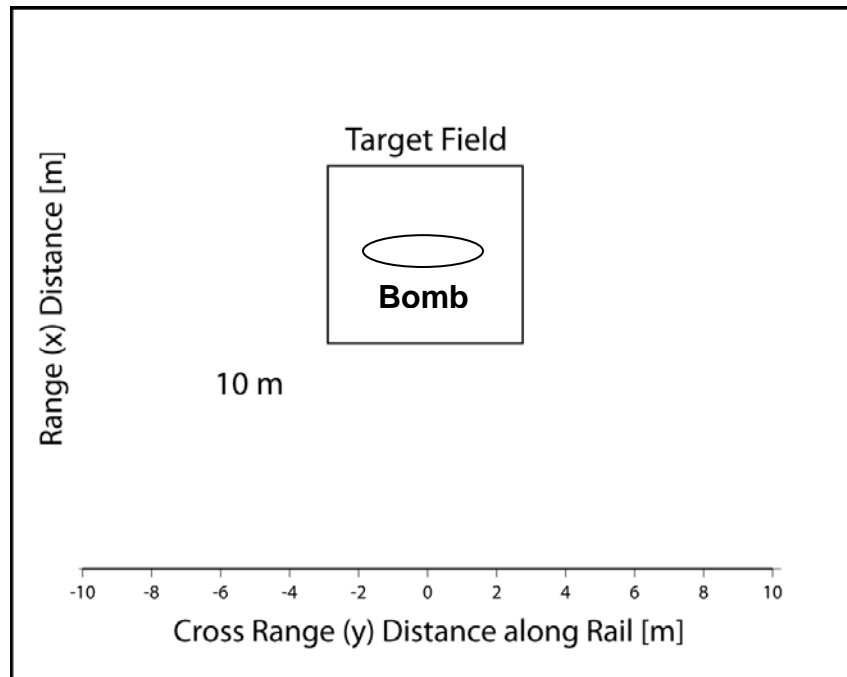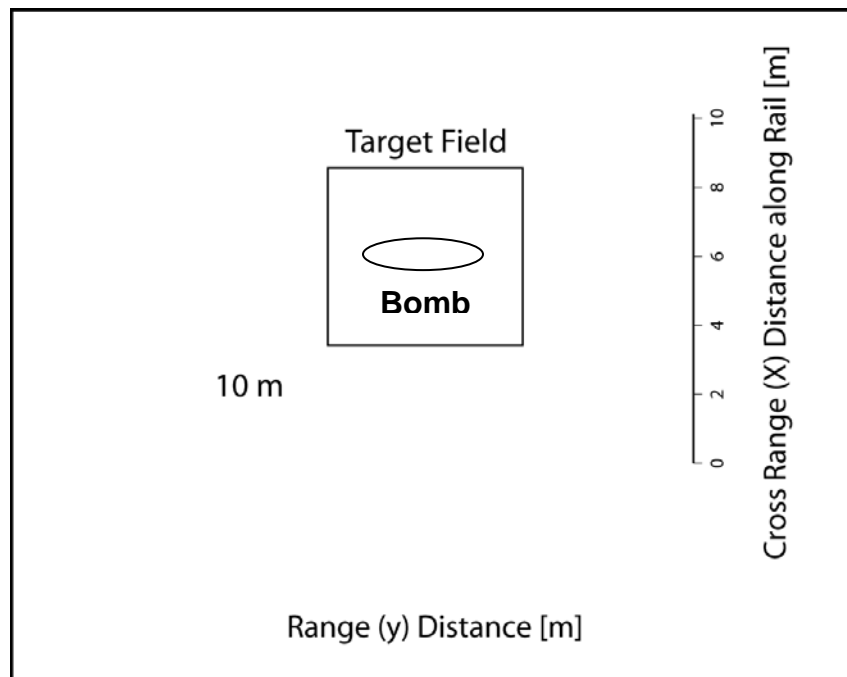
**Figure 37: a)** Geometry of the bomb oriented parallel to the rail. **b)** Hypothetical orientation of a rail oriented perpendicular to the geometry in a).

**Figure 38: a)** Same as Figure 35c.Two-dimensional plane view of the resonance migrated proud bomb oriented parallel to the rail using 25,960 Hz data. **b)** Similar to Figure 36c but rotated by 90°. Two-dimensional plane view of the resonance migrated proud bomb oriented parallel to the rail using 19,340 Hz data. **c)** Two-dimensional plane view with superimposed images in a) and b). The ellipses are added understand the orientation of the bomb in the three images and are not drawn to scale.
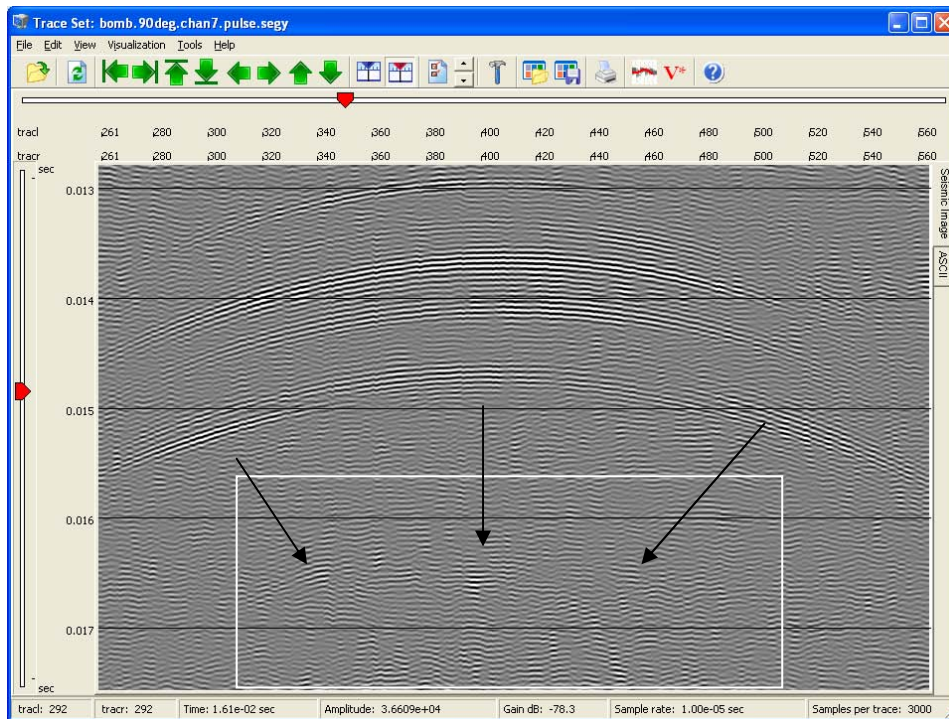
**Figure 39: a)** Time section of the waveforms recorded for the proud bomb oriented parallel to the rail. **b)** Time section of the waveforms recorded for the proud bomb oriented perpendicular to the rail. The arrows in both figures indicate the resonance scattered waves. The white rectangles indicate the part of the wavefield used to compute the spectra in Figure 40b). Amplitude gain control with a 0.005 s window length was applied to both wavefield sections.
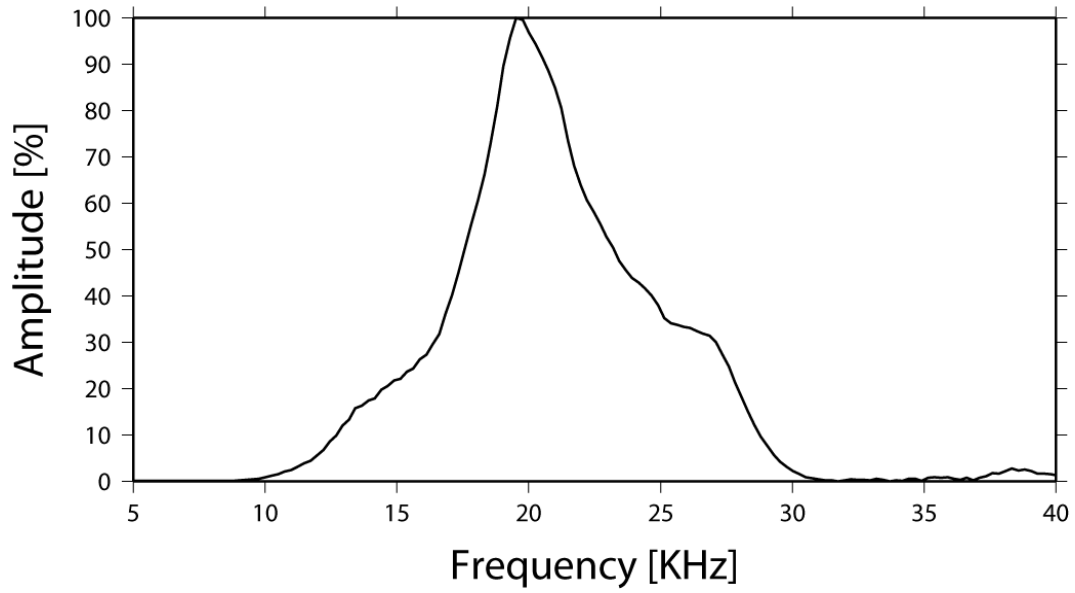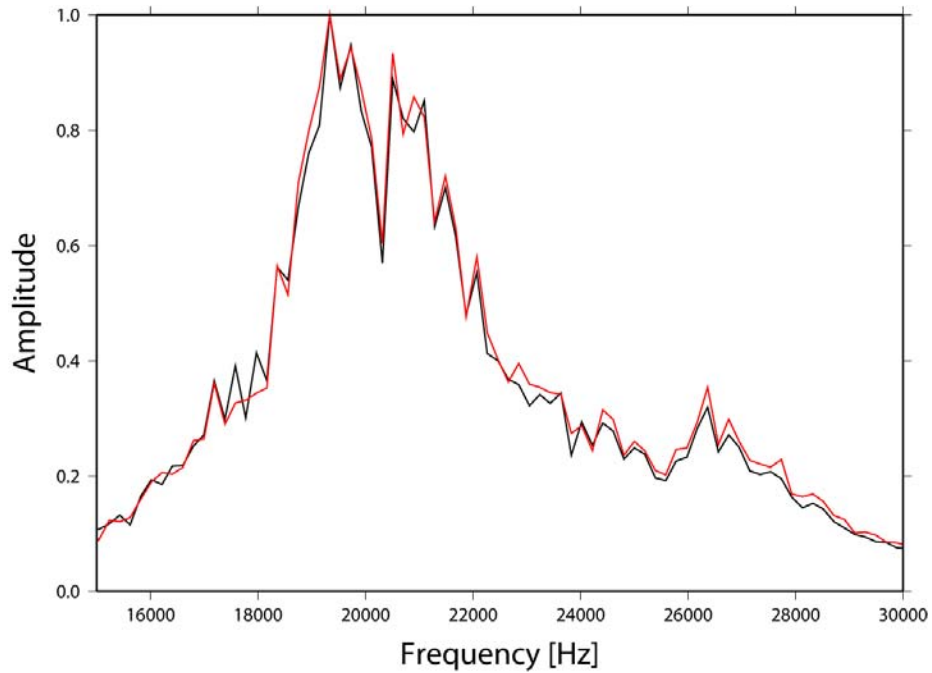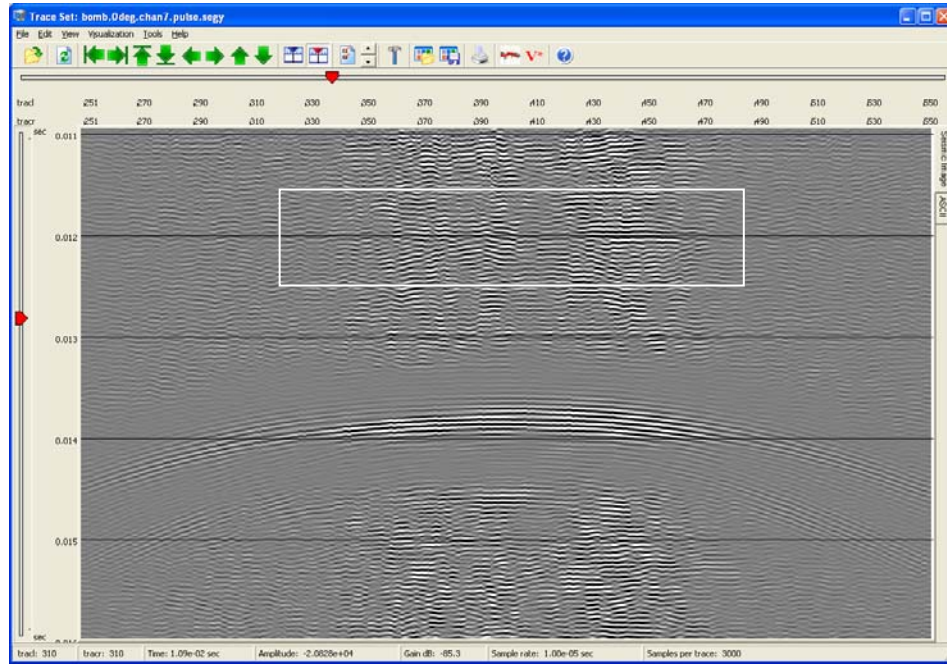
**Figure 40: a)** Spectrum of the source sweep (same as Figure 24b) **b)** Superposition of normalized resonance wave amplitude spectra for the proud bomb oriented parallel to the rail (black) and for the proud bomb oriented perpendicular to the rail (red). The resonance waves used to compute the spectra are highlighted by the white rectangles in Figure 39.
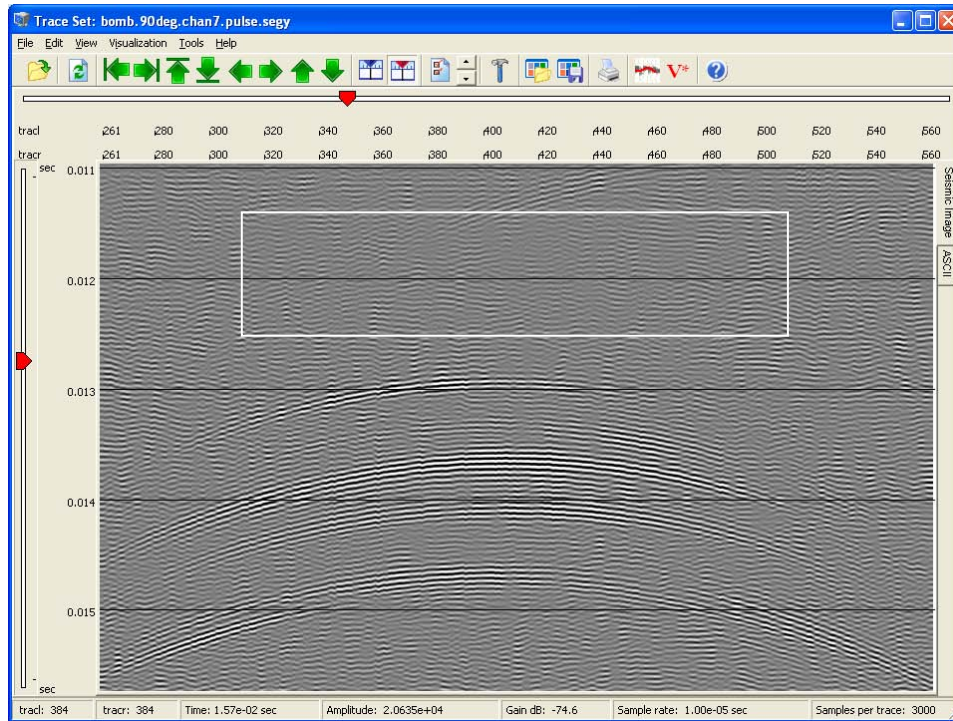
**Figure 41: a)** Time section of the waveforms recorded for the proud bomb oriented parallel to the rail (same as Figure 39a). **b)** Time section of the waveforms recorded for the proud bomb oriented perpendicular to the rail (same as Figure 39b). The white rectangles indicate the noise part of the wavefield used to compute the spectra in Figure 42b). Amplitude gain control with a 0.005 s window length was applied to both wavefield sections.
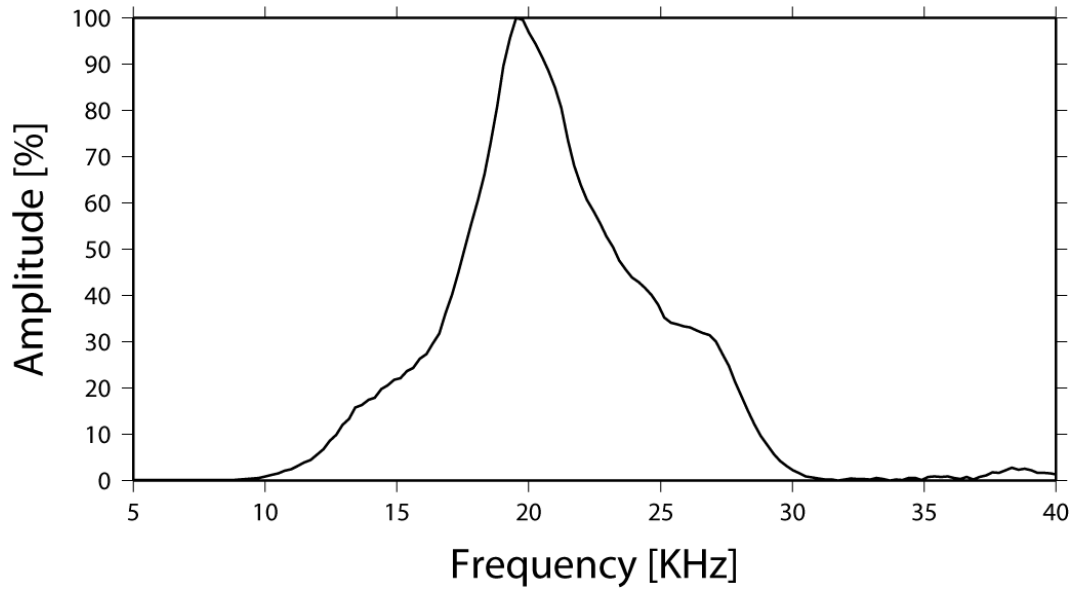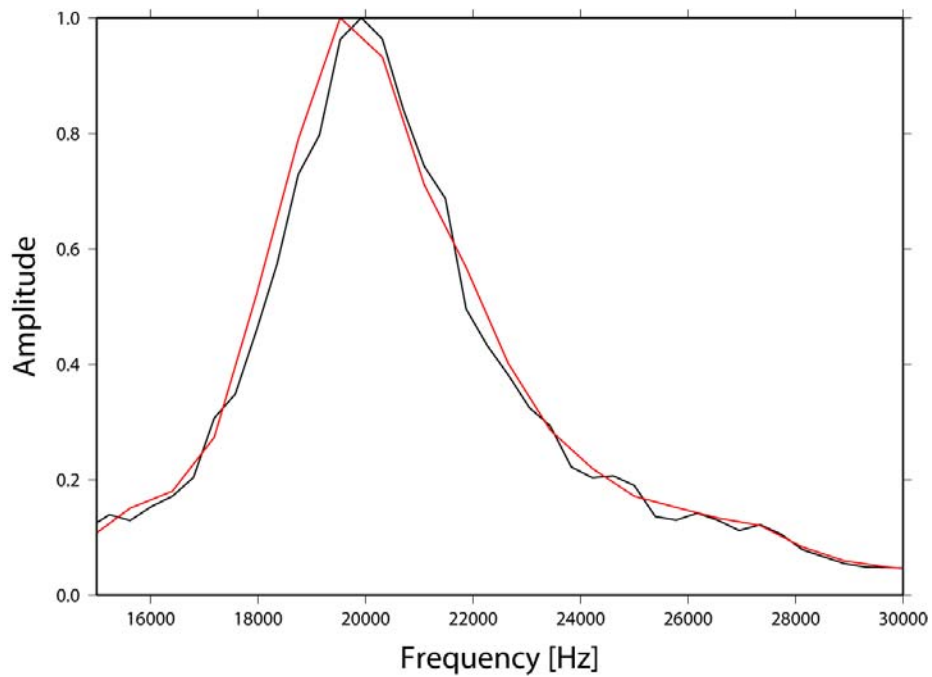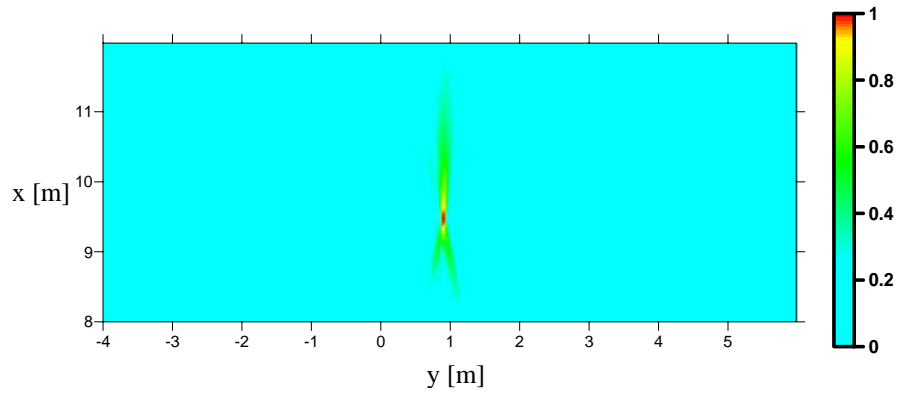
**Figure 42: a)** Spectrum of the source sweep (same as Figure 24b) **b)** Superposition of normalized noise spectra for the proud bomb oriented parallel to the rail (black) and for the proud bomb oriented perpendicular to the rail (red). The noise sections used to compute the spectra are highlighted by the white rectangles in Figure 41.
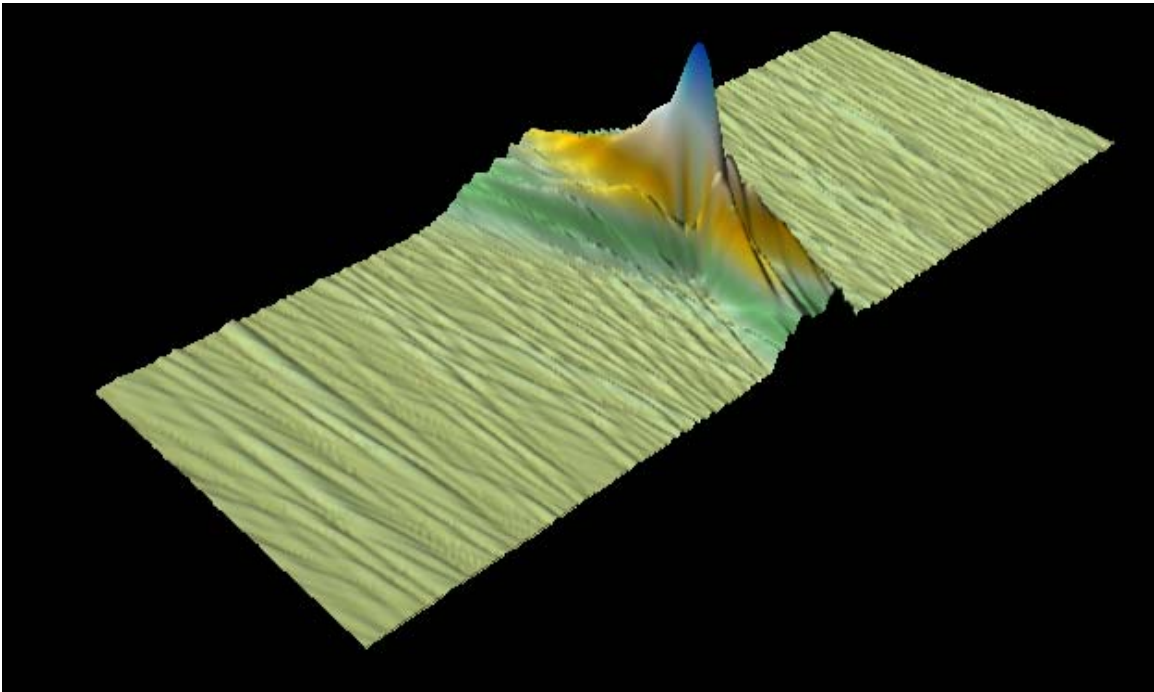
a)

b)

**Figure 43: a)** Two-dimensional plane view of the resonance migrated proud sphere. Migration was performed with a resonance frequency of 16,000 Hz and with the correct propagation velocity of P-waves in water (1,482 m/s). **b)** Three-dimensional surface plot of the image in a).
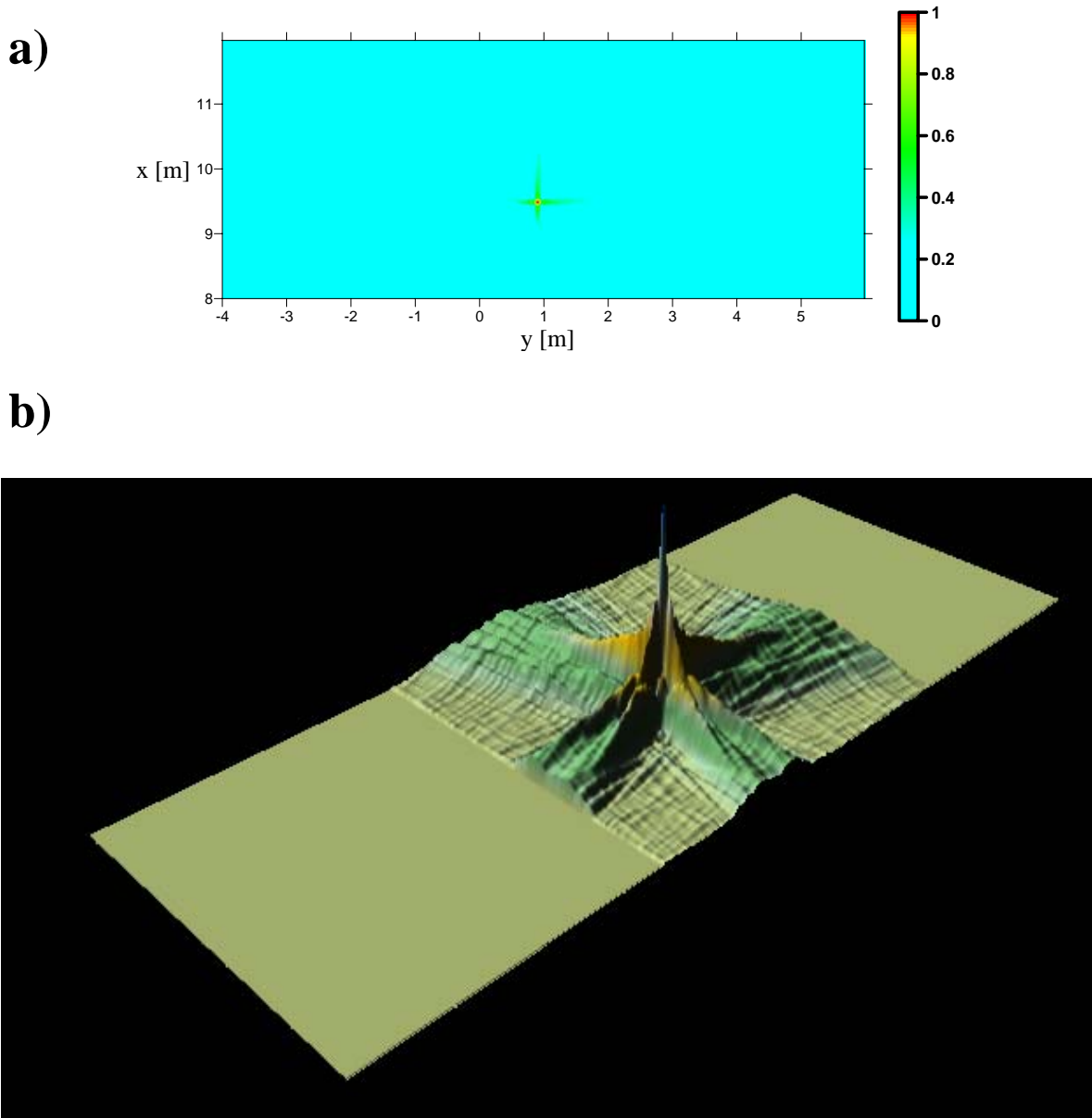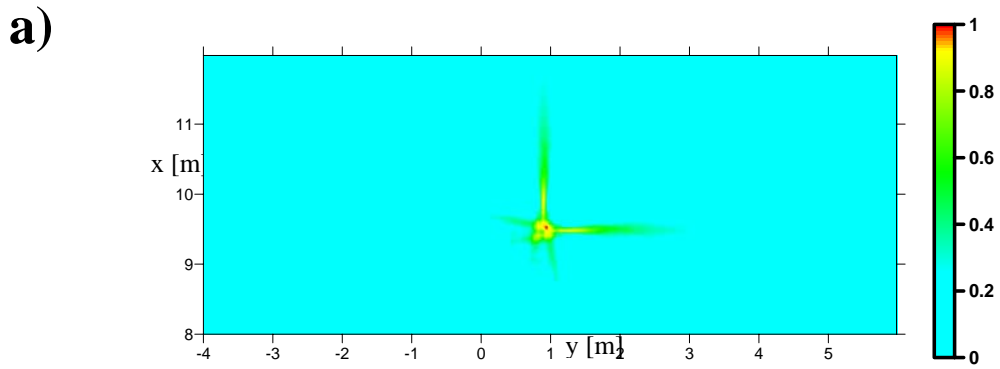
**Figure 44: a)** Two-dimensional plane view of the resonance migrated proud sphere. To produce the image it was assumed that two datasets from perpendicular profiles were available (along the pond rail in range (y) direction and along a second rail in the cross range (x) direction). Migration was done with a resonance frequency of 16,000 Hz and with the correct propagation velocity of P-waves in water (1,482 m/s). **b)** Three-dimensional surface plot of the image in a).
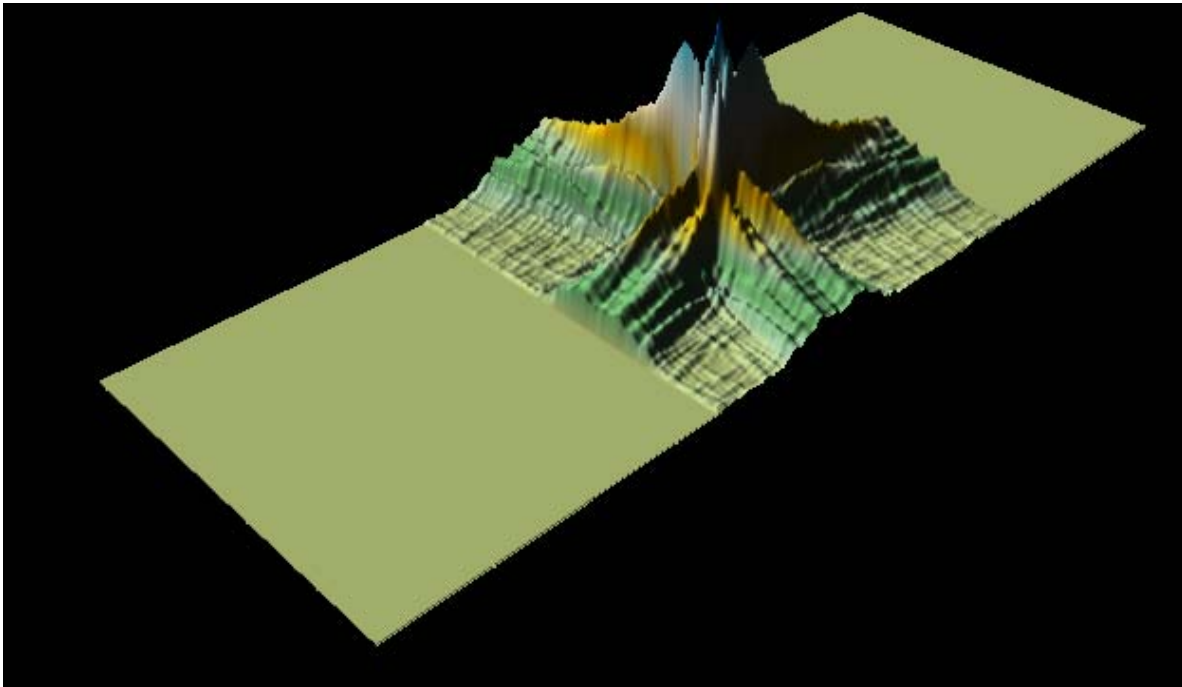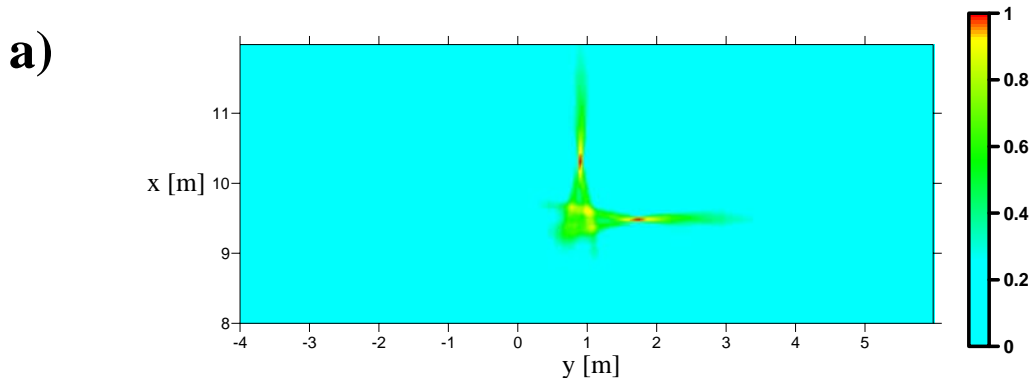
**Figure 45: a)** Two-dimensional plane view of the resonance migrated proud sphere. To produce the image it was assumed that two datasets from perpendicular profiles were available (along the pond rail in range (y) direction and along a second rail in the cross range (x) direction). Migration was done with a resonance frequency of 16,000 Hz and with an incorrect propagation velocity of P-waves in water (1,432 m/s). **b)** Three-dimensional surface plot of the image in a).
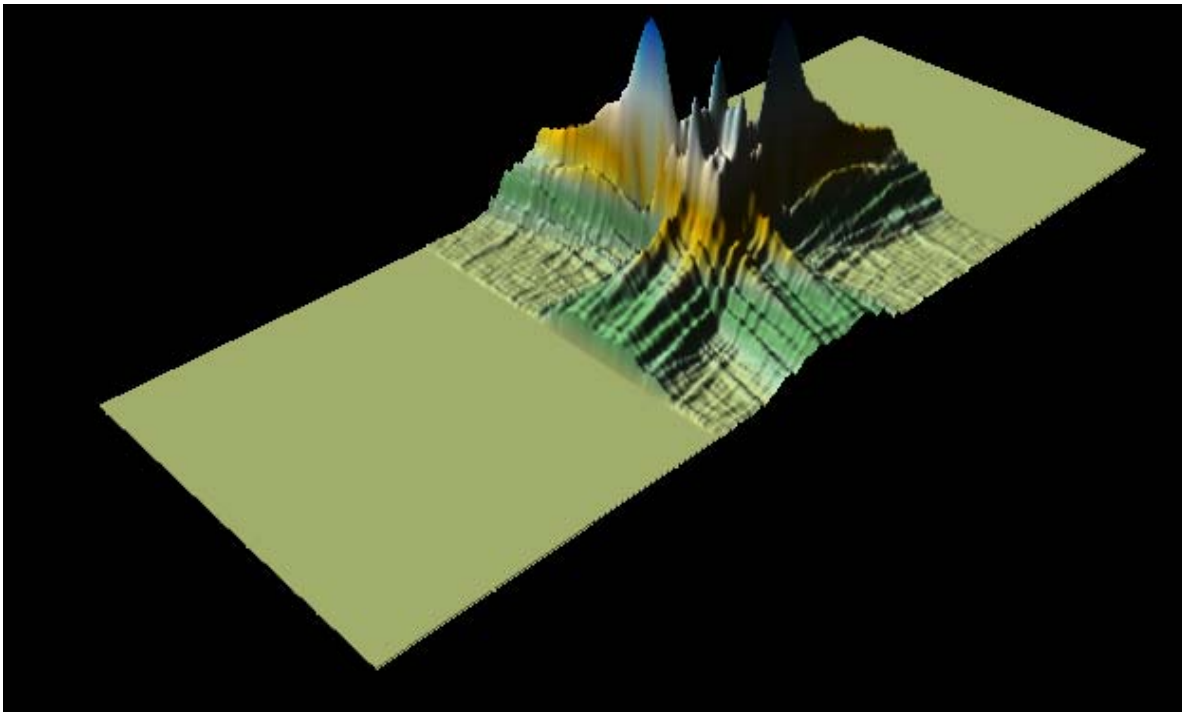
**Figure 46: a)** Two-dimensional plane view of the resonance migrated proud sphere. To produce the image it was assumed that two datasets from perpendicular profiles were available (along the pond rail in range (y) direction and along a second rail in the cross range (x) direction). Migration was done with a resonance frequency of 16,000 Hz and with an incorrect propagation velocity of P-waves in water (1,382 m/s). **b)** Three-dimensional surface plot of the image in a).